Detector readout electronics for EBEX : a balloon-borne cosmic microwave background polarimeter

François Aubin

Doctor of Philosophy

Department of Physics

McGill University

Montréal,Québec

2012/11/17

A thesis submitted to the Faculty of Graduate Studies and Research in partial fulfilment of the requirements for the degree of Doctor of Philosophy

DEDICATION

À mes parents Léane et Yves.

ACKNOWLEDGEMENTS

I first thank my supervisor prof. M. Dobbs for the numerous useful discussions we had. He was always available to discuss problems and those discussions helped me progress with my research. His support and trust contributed to facilitate the writing of this thesis. I also thank all the members of the EBEX collaboration. Designing, building and flying a state of the art balloon-borne telescope such as EBEX is a team project and requires complementary skills from many people. In particular, I thank the project investigator S. Hanany for many useful discussions; K. MacDermid, J. Hubmayr and K. Raach with whom I directly collaborated for the readout and detector testing and development and Chaoyun Bao for the atmospheric loading calculations she provided me and that are presented in Section 6.7.1. I also thank all the members of the Dobbs research group at McGill University with whom the DfMUX readout was developed. I especially thank G. Smecher who wrote all the DfMUX firmware, helped me debug the readout system and quickly provided firmware solutions for readout problems; A. Gilbert who helped me with the electronics hardware and McGill technician R. Gagnon who often performed on short notice SQUID glueing and wire bonding for our group.

I greatly thank my parents Léane and Yves for their support. They eased my life during the years my research was performed and always encouraged and supported me in reaching my goals. I also thank my girlfriend Chaoyun Bao for her support and her understanding of the long work hours and unpredictable schedules. I finally

thank all my friends who helped increase my research productivity by helping me change my mind once in a while.

ABSTRACT

EBEX (the E and B Experiment) is a balloon-borne telescope with 8' resolution primarily designed to detect the B-mode polarization of the cosmic microwave background radiation, which would represent strong evidence for the inflationary period of the universe. EBEX will also characterize the galactic dust and the gravitational lensing. During a 11 day long duration science flight over Antarctica scheduled for the Austral Summer of 2012-2013, EBEX will operate 872, 436 and 256 spider-web transition edge sensor (TES) bolometers at 150, 250 and 410 GHz, respectively, and observe a 350 square degree patch of sky.

The EBEX engineering flight in June 2009 over New Mexico and Arizona provided the first usage of both a large array of TES bolometers and a superconducting quantum interference device (SQUID) based multiplexed readout system in a space-like environment. The sensors were read out with a new SQUID-based digital frequency domain multiplexed (DfMUX) readout system that was designed to meet the low noise, low power consumption and robust autonomous operation requirements presented by a balloon experiment. The DfMUX readout system successfully tuned, monitored and operated the EBEX camera at float. This successful demonstration increases the technology readiness level of these bolometers and the associated readout system for future space missions.

In preparation for the science flight, the bolometer specifications to optimize the sensitivity of the EBEX camera have been calculated and verified to provide

EBEX with the required sensitivity to meet its science goals. A series of bolometer wafers were produced at University of California, Berkeley, and characterized at McGill University and University of Minnesota. From these wafers, 14 have been selected for integration for the EBEX long duration balloon flight. The multiplexing factor of the DfMUX readout system has also been demonstrated to be improved from 8 to 16. An algorithm allowing for the monitoring of the camera setup and the camera performance at float has been developed. The camera operator will use this algorithm to the camera during flight in order to optimize both the observing time of the telescope and the sensitivity of the camera. EBEX is ready to perform its long-duration science flight.

RÉSUMÉ

EBEX ("E and B Experiment") est un télescope maintenu en haute altitude par un ballon stratosphérique. Ce télescope conçu pour détecter la polarisation de type B du rayonnement cosmologique fossile possède une résolution de 8'. Une telle détection représenterait une évidence forte de la période inflationniste de l'univers. EBEX caractérisera également la poussière galactique ainsi que l'effet de lentille gravitationnelle. Pendant un vol de 11 jours prévu pendant l'été austral 2012-2013 au dessus de l'Antarctique, EBEX opérera 872, 436 et 256 bolomètres en transition supraconductrice dans les bandes de fréquence 150, 250 et 410 GHz, respectivement. EBEX observera une région du ciel de 350 degrés carrés.

Le vol d'essai de EBEX a eu lieu en juin 2009 au dessus du Nouveau-Mexique et de l'Arizona. Lors de ce vol d'essai, des bolomètres en transition supraconductrice ainsi qu'un système digital de lecture de données multiplexé en fréquence (DfMUX) avec amplificateurs supraconducteurs à interférence quantique (SQUID) ont été exploités avec succès dans un environnement spatial chacun pour la première fois. Le système DfMUX a été conçu pour permettre la lecture de bolomètres tout en respectant les exigences de produire peu de bruit électronique, de consommer peu d'énergie et de permettre une opération fiable des détecteurs. Ces exigences sont requises pour opérer un tel télescope en haute atmosphère. Lors de ce vol, le système DfMUX a mis au point et a vérifié avec succès le bon fonctionnement de la caméra de EBEX. Cette démonstration prépare le terrain pour l'utilisation des bolomètres en transition supraconductrice ainsi que le système DfMUX dans le cadre de futures missions

spatiales.

En préparation pour le vol scientifique de EBEX, les paramètres des bolomètres permettant d'optimiser la sensibilité de la caméra ont été calculés. La sensibilité calculée permettra à EBEX d'atteindre ses buts scientifiques. Parmi les dizaines de gaufres de détecteurs fabriquées à l'Université de la Californie, Berkeley, et caractérisées à l'Université McGill et à l'Université du Minnesota, 14 ont été sélectionnées pour l'intégration de l'instrument EBEX précédent le vol de longue durée. L'amélioration du facteur de multiplexage du système DfMUX de 8 à 16 a également été démontrée. Un algorithme permettant de surveiller la mise au point ainsi que la performance en vol de la caméra a été élaboré. L'opérateur de la caméra utilisera cet algorithme pendant le vol afin d'optimiser le temps d'observation du télescope ainsi que le sensibilité de la caméra. EBEX est prêt à entreprendre son vol scientifique.

TABLE OF CONTENTS

LIST OF TABLES

LIST OF FIGURES

CHAPTER 1
Introduction

The cosmic microwave background (CMB) was first measured by Penzias and Wilson in 1964 [1]. The precise measurements performed since have allowed for great improvements in the understanding of the content and the evolution of the universe. The polarization of the cosmic microwave background was first measured in 2002 by the Degree Angular Scale Interferometer (DASI) [2]. The polarization of the CMB represents a rich field of study since it will allow for the improvement of our understanding of the universe in many aspects : the inflationary period of the universe, gravitational lensing, large-scale structures, neutrinos, galactic dust, etc.

The E and B experiment (EBEX) is a balloon-borne millimeter wavelength telescope. The primary goal of EBEX is to detect the predicted imprint of the primordial gravity waves on the polarization of the CMB. This detection would support the existence of the primordial gravity waves. EBEX stands out from other balloon-borne telescopes by being sensitive to angular scales smaller than 1°. Only the Planck satellite mission, within instruments detecting photons from above the atmosphere, will be sensitive to millimeter wavelength photons at these angular scales [3]. Telescopes on balloon platforms are also cheaper to build than telescopes on satellite platforms and EBEX represents an innovative opportunity to develop the technology suitable for an even more sensitive satellite mission in the future. By detecting photons from above most of the terrestrial atmosphere, EBEX also gains an

important advantage over ground-based telescopes with similar goals. The smaller atmospheric signal and noise measured by balloon-borne telescope greatly improves the sensitivity of the receiver compared to ground-based telescopes.

Ballooning, however, has its challenges since risks are increased compared to ground-based telescopes. The telescope is designed to avoid single mode failures which would jeopardize the science goals of the mission. The telescope is also required to be commanded remotely with limited telemetry. The telescope and the hard drive on which the data are stored also risk being destroyed at landing. Balloon flight length is furthermore currently limited to a few weeks because of the constraints on the time the balloon can stay at float. EBEX, due to cryogenic constraints, will be limited to only 11 days. However, these risks and constraints are surmountable and the massive sensitivity gain will allow EBEX to compete with ground-based telescopes even with 11 days of observations.

This thesis presents the commissioning of the digital frequency readout multiplexing readout system and the TES bolometers, both used for the first time in a space-like environment during the June 2009 EBEX engineering flight. This thesis also presents the design and the preparation for the EBEX long-duration ballon flight scheduled for the Austral Summer of 2012-2013 in Antarctica. The science background motivating EBEX is first introduced in Chapter 2. The main goals EBEX pursues are presented in Chapter 3. The components of the EBEX telescope are also described in Chapter 3 : the pointing system, the software, the receiver and the focal planes. The theory of operation of TES bolometers with the methodology followed to produce, test and select science grade bolometer wafers is outlined in

Chapter 4. Arrays of kilopixel bolometers are required to be multiplexed and the digital frequency multiplexing readout system EBEX uses is detailed in Chapter 5. The commissioning of the improvement of the multiplexing factor from 8 to 16 is also demonstrated. Chapter 6 shows the results obtained during the EBEX engineering flight. The readout performance and power consumption are described. The receiver operation and stability as well as noise performance are presented. The optical loading incident on the bolometers is also measured. Finally, the bolometer specifications of the detectors to be used during the EBEX long-duration science flight are derived and the status of the fabricated bolometers is described in Chapter 7. The expected noise performance of those detectors for the science flight is predicted and the methodology to monitor and ensure the proper functioning of the detectors at float is outlined.

CHAPTER 2
Science Background

According to the "Big Bang" model, today's observable universe was originally concentrated in a singularity 13.7 billion years ago and suddenly started to expand. As the universe expanded, the hot adiabatic gas of elementary particles composing the universe cooled down and the complexity of its structures consequently increased. When the universe was 380 000 years old and its temperature, $\sim$3000 K, the association of free electrons and protons to form hydrogen atoms became energetically favorable and the universe became neutral. The photons, which interacts with the electrically charged particles through Thomson scattering, then became free to propagate through the neutral universe. The photons emitted at this "surface of last scattering" form the CMB. The CMB was measured to be a nearly perfect blackbody with temperature (2.725 ± 0.001) K by the Far Infrared Absolute Spectrophotometer (FIRAS) aboard the Cosmic Background Explorer (COBE) satellite [4]. This chapter describes the standard model of cosmology, the inflation paradigm and its imprint on the CMB and the potential sources of contamination.

2.1 The Λ-CDM Model

The standard model of cosmology is referred to as Λ-CDM because it describes the universe as dark energy (Λ) and cold dark matter (CDM) dominated. This model describes the universe as spatially flat with minimally 6 parameters : the physical baryon density, the physical dark matter density, the dark energy density, the scalar

spectral index, the curvature fluctuation amplitude and the re-ionization optical depth. Extensions to this model allow for the universe not to be flat, the density of dark energy to vary as the universe expands, a running of the spectral index, etc. The Wilkinson Microwave Anisotropy Probe (WMAP) is a satellite mission which measured with precision the intensity of the CMB with sub-degree resolution [5]. Figure 2–1 shows the whole sky map of the CMB temperature fluctuations measured by WMAP after seven years. The monopole component due to the average temperature of the CMB and the dipole component due to the relative movement of the WMAP satellite with respect to the CMB are subtracted. This figure is a linear combination of the five maps WMAP measured at 23, 33, 41, 61 and 94 GHz, with weights chosen to minimize the galactic foregrounds.

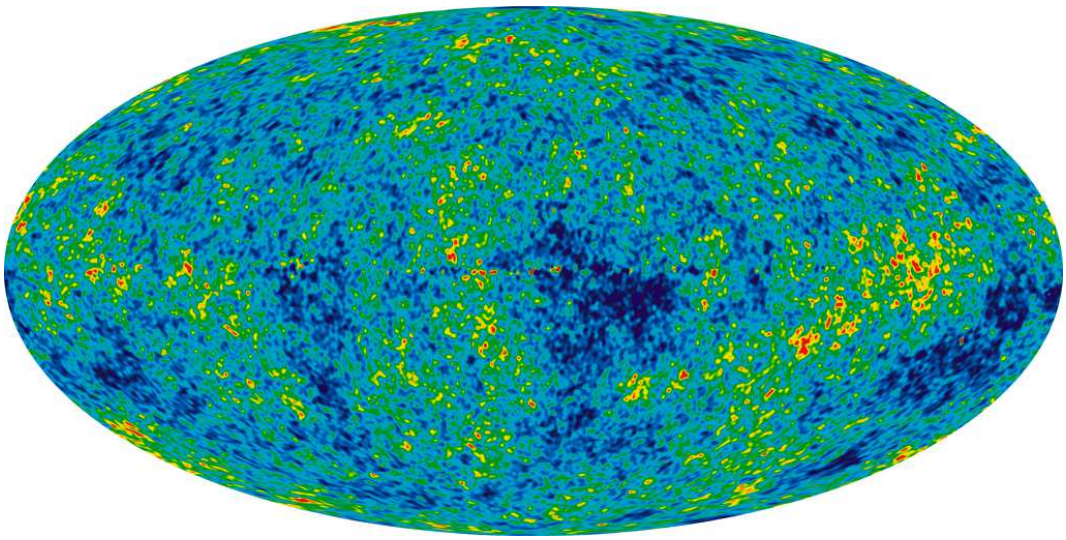

Figure 2–1: Measurement of the CMB temperature anisotropy performed by WMAP after 7 years. The scale is linear and ranges from -200 to 200 μK. [Figure courtesy of the WMAP Science Team]

The power spectrum of Figure 2–1, combined with the data measured with smaller angular resolution by the Arcminute Cosmology Bolometer Array Receiver (ACBAR) [6] and the Q and U Extragalactic Sub-mm Telescope (QUEST) at DASI (QUaD) [7], is computed and shown in Figure 2–2 with the best fit Λ-CDM model. From this spectrum, the universe is found to be currently dominated by dark energy and is composed of 73% dark energy, 23% cold dark matter and 5% baryonic matter. When the universe became neutral, it was cold dark matter dominated and was composed of 63% cold dark matter, 15% photons, 12% baryonic matter and 10% neutrinos [8]. The universe is therefore dominated by dark energy and cold dark matter.

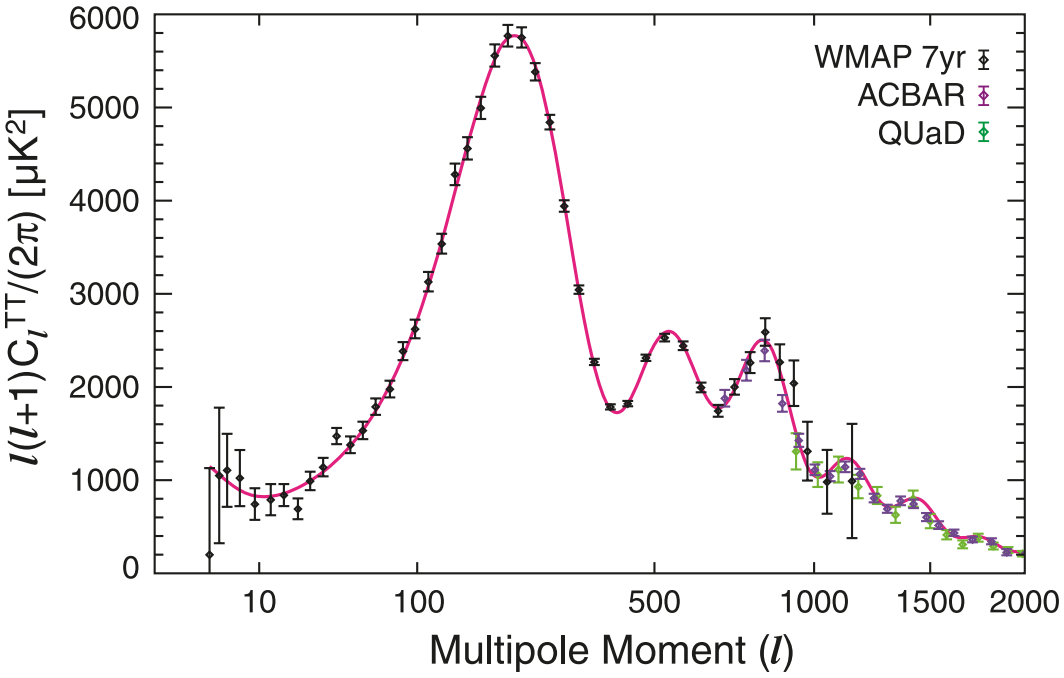

Figure 2–2: Measured power spectrum of the CMB by WMAP, ACBAR, and QUaD with the best fit Λ-CDM model [9].

The intensity of the CMB has therefore been precisely measured at all but the very smallest angular scales. However, the Λ-CDM model without an inflationary period[1] does not account for all the subtleties of the data acquired by WMAP and other similar experiments, such as ACBAR [6], QUaD [7], the South Pole Telescope (SPT) [10], the Cosmic Background Imager (CBI) [11], the Very Small Array (VSA) [12] and the Balloon Observations of Millimetric Extragalactic Radiation and Geophysics (BOOMERANG) experiment [13]. The CMB is almost perfectly thermalized across the full sky. However, over the time period between the Big Bang and the time the CMB photons were emitted, most parts of the CMB were not in causal contact. Also, for the universe to be close to flat at our age, it requires to be fine tuned so it was almost perfectly flat at early ages. Finally, as the universe temperature cooled and reached temperatures associated with the unification of the strong and the electroweak interactions (10^{14} GeV) and with the electromagnetic and the weak interactions (300 GeV), the presence of magnetic monopoles in the CMB is expected. The monopoles generated by symmetry breakdowns are not observed [14]. The most prominent theory to solve these inconsistencies which is compatible with all current observations is the inflationary model and is presented in the following section. Inflation is included in the standard cosmology model.

[1] Other models can account for those subtleties, but are not discussed in this thesis.

2.2 Inflation

In order to account for the imperfections of the Λ-CDM model, the inflationary model is postulated [15]. Inflation is the exponential expansion of the early universe. The universe is commonly thought to expand by at least 26 orders of magnitude within 10^{-34} seconds. Its source is the inflaton repulsive scalar field ϕ. Inflation allows for the horizon to encompass the observable universe and to explain the inconsistencies enumerated in the previous section.

The expansion rate of the universe is characterized by the Hubble parameter

$$H^2 = \frac{1}{3M_{pl}^2}\left(\frac{\dot{\phi}^2}{2} + V(\phi)\right), \tag{2.1}$$

where $V(\phi)$ is the inflationary potential, $M_{pl} = \sqrt{\frac{\hbar c}{8\pi G}}$ is the reduced Planck mass, $\hbar$ is the reduced Planck's constant, c is the speed of light and G is the gravitational constant. The "slow roll" inflation, a simple inflationary model, requires the kinetic term to be small with respect to the potential term in Equation 2.1 [16]. The "slow roll" inflation is described by the parameters

$$\epsilon = \frac{M_{pl}^2}{2}\left(\frac{V'(\phi)}{V(\phi)}\right)^2 \tag{2.2}$$

$$\eta = M_{pl}^2\left(\frac{V''(\phi)}{V(\phi)}\right), \tag{2.3}$$

where $V' \equiv \frac{dV(\phi)}{d\phi}$, and the "slow roll" condition is met when $\epsilon, |\eta| \ll 1$. Under these conditions, the inflaton is related to its potential by

$$3H\dot{\phi} + V'(\phi) \approx 0 \tag{2.4}$$

and the size of the universe is described by

$$R(t) = R(0)e^{Ht}. \tag{2.5}$$

The universe therefore exponentially expands during the inflationary period. When the "slow roll" condition is no longer satisfied, inflation stops and reheating occurs. The universe temperature then returns to its pre-inflation temperature due to inflaton decays.

Density fluctuations of the universe are scalar perturbations. The scalar spectrum can be written as the power law

$$P_S(k) = P_S(k_0)\left(\frac{k}{k_0}\right)^{n_s(k_0)-1+\alpha_s(k_0)\frac{ln(k)}{ln(k_0)}}, \tag{2.6}$$

where k is the wave number, k_0 is the arbitrary pivot scale, n_s is the scalar spectral index and α_s is the running scalar spectral index [17, 18]. A scalar spectral index

of 1 corresponds to a scale invariant spectrum. Inflation also predicts the existence of primordial gravity waves which are tensor perturbations and the tensor spectrum can be written as the power law

$$P_T(k) = P_T(k_0)\left(\frac{k}{k_0}\right)^{n_T}, \tag{2.7}$$

where n_T is the tensorial spectral index [19]. A spectral index of 0 corresponds to a scale invariant spectrum. The scalar and tensorial spectrums are calculated to be

$$P_{S\ SR}(k) = \frac{2\pi}{3M_{pl}^6}\frac{V^3(\phi)}{V'^2(\phi)} \tag{2.8}$$

$$P_{T\ SR}(k) = \frac{2}{3M_{pl}^4}V(\phi). \tag{2.9}$$

for the "slow roll" inflationary model [19].

In order to quantify the magnitude of gravity waves, the tensor to scalar ratio is defined as

$$r = \frac{P_T}{P_S} \tag{2.10}$$

and is evaluated to be

$$r_{SR} = \frac{M_{pl}^2}{\pi}\left(\frac{V'(\phi)}{V(\phi)}\right)^2 \tag{2.11}$$

for the "slow roll" inflation.

The detection of the primordial gravity waves would represent strong evidence for inflation. Their imprint on the polarization of the CMB is discussed in the next section.

2.3 Polarization of the CMB

Gravity waves produced during the period of inflation imprint a signature on the polarization of the CMB. This section describes the Stokes formalism for polarization and the sources of polarization of the CMB.

2.3.1 Stokes Formalism

The Stokes formalism allows for the quantification of the degree of polarization of photons. The polarization of the electromagnetic wave travelling in the $\hat{z}$ direction

$$\vec{E}(z,t) = E_{0x}e^{i(\omega t - kz + \phi_x)}\hat{x} + E_{0y}e^{i(\omega t - kz + \phi_y)}\hat{y}, \tag{2.12}$$

where ω is the wave angular frequency and k is the wave number, is characterized by the Stokes parameters I, Q, U and V. The parameter I represents the total intensity of the wave. The parameter Q quantifies the difference of polarization between the axes $\hat{x}$ and $\hat{y}$. The parameter U quantifies the difference of polarization between

the axes $\hat{x} + \hat{y}$ and $\hat{x} - \hat{y}$. The parameter V quantifies the difference of polarization between the right-hand and the left-hand circularly polarization. The equations to calculate these parameters are

$$\begin{cases} I = E_{0x}^2 + E_{0y}^2 \\ Q = E_{0x}^2 - E_{0y}^2 \\ U = 2E_{0x}E_{0y}cos(\phi_y - \phi_x) \\ V = 2E_{0x}E_{0y}sin(\phi_y - \phi_x). \end{cases} \tag{2.13}$$

The Stokes parameters I, Q, U and V are equivalent to the electromagnetic wave parameters E_{0x}, E_{0y}, ϕ_x and ϕ_y, but allow for a more efficient quantification of the degree of polarization of electromagnetic waves. No sources of V polarization on the CMB are known.

2.3.2 Sources of Polarization

The polarization of the CMB originates from Thomson scattering within quadrupole structures composed of two cold and two warm temperature inhomogeneities. A collision between unpolarized photons and an electron through Thomson scattering produces scattered photons with a net polarization along the axis perpendicular to both the incoming and the scattered photons, as shown in Figure 2–3. Photons colliding with electrons within a quadrupole temperature structure produce scattered photons with a net polarization tracing the cold axis of the quadrupole since the photons incoming from the cooler regions are less energetic than the photons incoming from the warmer regions.

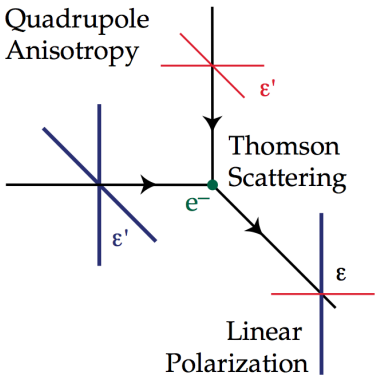

Figure 2–3: Net polarization of the CMB generated by Thomson scattering. The scattering of unpolarized photons off an electron produces photons polarized in the direction perpendicular to both the direction of the incoming and the scattered photons. The photons incoming from cold temperature inhomogeneities have their polarization shown in red and the photons incoming from the warm temperature inhomogeneities have their polarization shown in blue. The net polarization of the scattered photons traces the cold axis of the quadrupole structure of the temperature anisotropy [20].

At the surface of last scattering, matter over-densities corresponds to cold regions of the CMB since the photons climb out of a deeper gravitational potential than photons emitted from under-densities, corresponding to hot regions of the CMB. The plasma is accelerated from under-densities towards over-densities due to gravitational attraction and is decelerated as it reaches over-densities due to radiative pressure. When the plasma is accelerated, the photons are red-shifted along the direction of their displacement with respect to the plasma, in the electron frame, and a quadrupole with a cold axis parallel to the plasma movement is created. The scattered photons from the CMB therefore have a net polarization parallel to the plasma displacement and the polarization pattern shown in Figure 2–4 a) is observed around hot regions of the CMB. When the plasma is decelerated, the photons are blue-shifted

along the direction of their displacement in the electron frame and a quadrupole with a warm axis parallel to the plasma movement is created. The scattered photons from the CMB therefore have a net polarization perpendicular to the plasma displacement and the polarization pattern shown in Figure 2–4 b) is observed around cold regions of the CMB. Both of those patters are curl-free (Q≠0, U=0) and are called "E-modes" analogously to electric fields. The density fluctuations generating E-mode polarization are scalar perturbations.

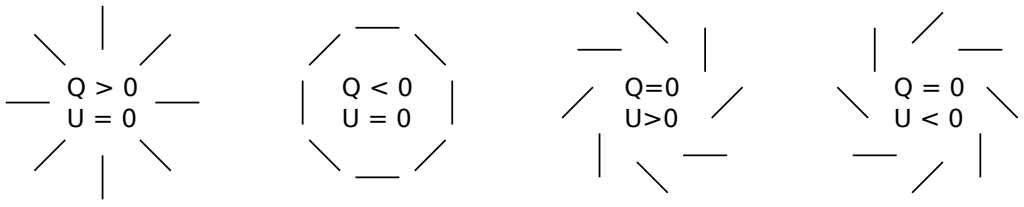

(a) (b) (c) (d)

Figure 2–4: Figure a) and b) show pure E-mode polarization with positive and negative Q, respectively. Figure c) and d) show pure B-mode polarization with positive and negative U, respectively.

The E-mode CMB polarization have been measured by many experiments, such as the DASI [2], CBI [21], the BOOMERanG experiment [22], the Cosmic Anisotropy Polarization Mapper (CAPMAP) [23], the Anisotropy Experiment Imaging Array with polarization sensitivity (MAXIPOL) [24], the Background Imaging of Cosmic Extragalactic Polarization (BICEP) experiment [25], QUaD [7] and WMAP [26]. Figure 2–5 shows the measurement of the power spectrum of the E-modes with the best fit Λ-CDM model.

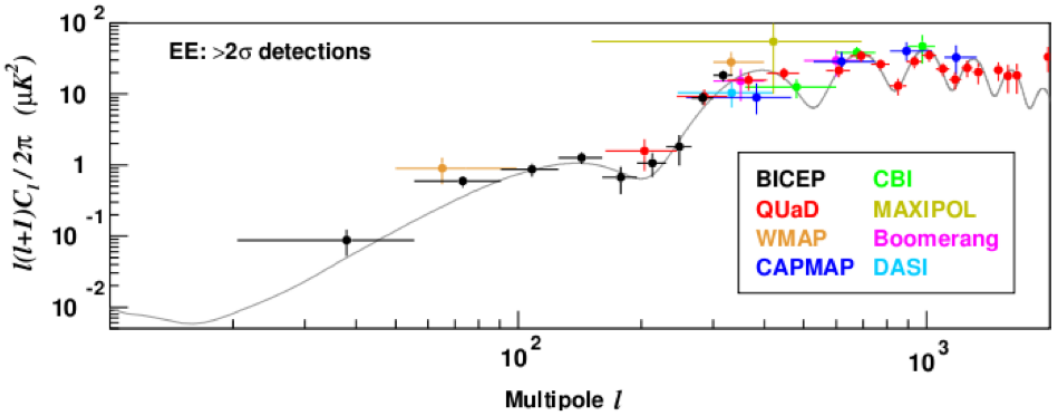

Figure 2–5: Measured power spectrum of the E-mode polarization of the CMB with the best fit Λ-CDM model [25].

The gravity waves, or tensor perturbations, present at the surface of last scattering distort space-time and produce both a divergence-free polarization called "B-modes" (Q=0, U≠0), analog to magnetic fields, and E-modes. The distortion of space-time red and blue-shifts the photons and creates polarization through Thomson scattering as shown in Figure 2–3. The magnitude of the tensor perturbations is minimally one order of magnitude smaller than the magnitude of the scalar perturbations and distinguishing the tensorial E-modes from the scalar E-modes is therefore very challenging. The polarization patterns observable from gravity waves are best observed using their B-mode signature and follow the ones presented in Figure 2–4 c) and d).

The vertexes of the plasma, or vector perturbations, also generate polarization on the CMB. The quadrupole structures generated by the vector perturbations are composed of two dipoles of opposite direction caused by Doppler effects. The vector perturbations generate both E and B-modes. Even though they can be significant

in some models, they are expected to be negligible in most and are not discussed in this thesis.

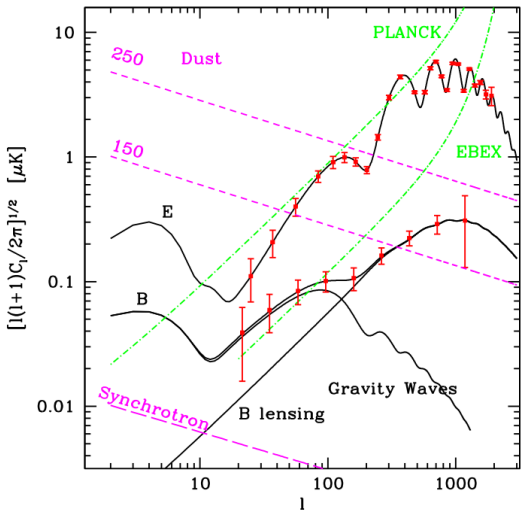

Figure 2–6: Power spectrum of the E and B-mode polarization as a function of the multipole moment ℓ expected to be measured by EBEX assuming the tensor to scalar ratio r is 0.05. The black lines show the theoretical model and the red points and error bars show the expected EBEX sensitivity during a 11 day flight. Pessimistic dust spectrum predictions within the 150 and 250 GHz EBEX bands and the synchrotron foregrounds within the 150 GHz EBEX band are also shown. The green lines finally show the power spectrum of the beam-size pixel noise for EBEX and the PLANCK satellite mission. [Figure courtesy of Carlo Baccigalupi, International School for Advanced Studies, SISSA]

The polarization is measured point by point on the sky and the vector field formed by all of these pixels is split into the E and B-mode basis. The power spectrum of those two vector fields is then computed. Figure 2–6 shows the power spectrum of E and B-modes EBEX is expected to measure if the tensor to scalar ratio r is 0.05 : the approximate sensitivity EBEX is expected to achieve. The detection of B-mode CMB polarization would represent strong evidence for inflation. However,

since the B-mode polarization is expected to be small, the foregrounds have to be understood properly to extract the B-mode signal. The next section describes these foregrounds.

2.4 Foregrounds

The foreground contamination is required to be meticulously characterized and subtracted from the measured signal because of the small magnitude of the B-mode signal of the CMB. Galactic dust and synchrotron radiation produce polarized light which can potentially contaminate the B-mode signal EBEX attempts to measure. Also, gravitational lensing converts E-modes into B-modes on small anglar scales.

Galactic dust is composed of asymmetric millimeter dust particles absorbing and re-emitting polarized photons. Within the 100 to 500 GHz range, the power spectrum of this signal increases with frequency. Figure 2–6 shows the magnitude of the pessimistic polarized emission expected from galactic dust on the fraction of the sky region and within the frequency bands EBEX will observe. Dust will dominate the signal in the highest frequency bands of EBEX and will allow for its characterization and subsequent subtraction from lower frequency band data [27].

Synchrotron radiation is due to the acceleration of electrons by magnetic fields and is polarized. The expected contamination within the 150 GHz EBEX frequency band is shown in Figure 2–6 and is expected to be negligible for EBEX due to the low contamination of the sky region chosen to be observed [27].

The effects of the gravitational lenses deflecting the CMB photons before they are detected converts E-modes into B-modes and vice-versa. Given the dominant magnitude of the E-modes with respect to the B-modes, the transformation from

E-modes to B-modes is important and can contaminate the B-mode signal, but the transformation from B-modes to E-modes is negligible. The power spectrum of the E to B-mode leaking signal due to gravitational lensing is shown as "B lensing" in Figure 2–6. Lensing effects are important at scales of ℓ >100 [28].

Therefore, the galactic dust and the E to B-mode leaking signal will be significant for EBEX and will be required to be adressed when extracting the B-mode signal from the data.

2.5 Summary

In order to detect primordial gravity waves, the polarization of the CMB will be measured. The vector field will be decomposed in the basis of E and B-mode polarization and their power spectrum will be computed. The galactic dust will be characterized at high frequency and subtracted from the lower frequencies. The gravitational lensing B-mode spectrum will be measured for the angular scales $\ell >$ 100 and the primordial gravity waves would be measured for angular scales $\ell < 100$ if r>0.04. Chapter 3 describes the EBEX telescope optimized to measure the signature of the primordial gravity waves through the B-mode CMB polarization.

The intensity of the CMB and its E-mode polarization have been well characterized by contemporary experiments. A theory such as inflation has to be included into the Λ-CDM model to both describe accurately the observations of the CMB and to explain the causality, flatness and monopole problematics related to the CMB observations. The detection of B-mode polarization of the CMB would increase the degree of confidence in the existence of the inflationary period of the universe.

CHAPTER 3
The EBEX Experiment

EBEX is a balloon-borne telescope scheduled to be launched by NASA Columbia Scientific Balloon Facility (CSBF) in December 2012 for a flight that will circumnavigate Antarctica. This long duration balloon (LDB) science flight is expected to last 11 days, limited by cryogenics. This chapter describes the science goals EBEX pursues, the methodology EBEX will follow and the components of the EBEX gondola, pointing system and receiver.

3.1 EBEX Science Goals

The primary science goal for EBEX is to detect the gravitational waves produced during the inflationary period of the universe through the signature they imprint on the polarization of the CMB. EBEX will detect B-modes if $r \widetilde{>} 0.04$. Gravity waves are the only primordial source of B-modes on large angular scales and their detection would represent a strong experimental evidence of the inflationary period. In the event of a non-detection, EBEX will improve the current upper limit of $r < 0.17$ to $r < 0.04$ with a 2σ confidence level [29]. Such an upper limit would constrain the inflation potential to $V^{\frac{1}{4}}(\phi) < 1.65 \times 10^{16}$ GeV. An upper limit of 0.04 on r would rule out classical inflationary models, i.e. the simplest models.

EBEX will also measure the lensing effects on the CMB polarization through small scale B-modes. A signal-to-noise ratio of 7 on the detection of B-modes from lensing is expected to be achieved. Such a measurement would constrain the sum of

the neutrino masses $\sum m_\nu$, the dark energy equation of state w and the dark energy evolution equation w_a with a 1σ precision 0.12 eV, 0.2 and 0.4, respectively.[1]

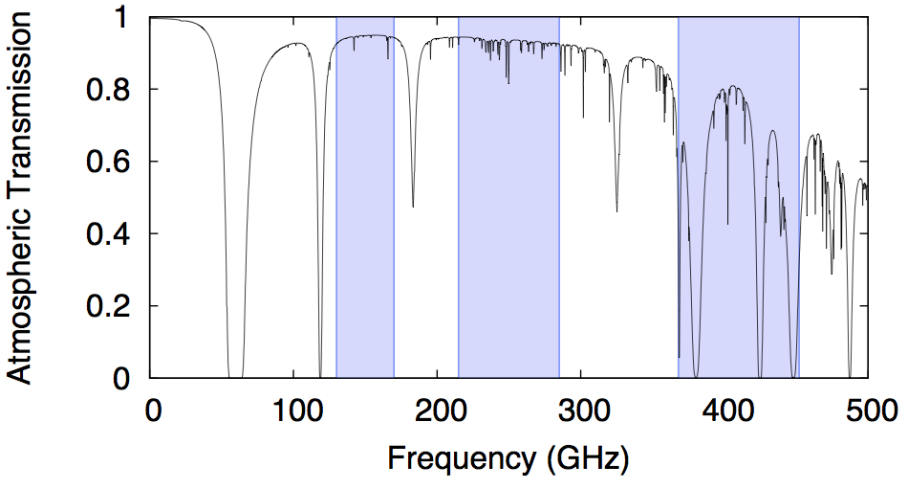

Figure 3–1: Atmospheric transmission to millimeter wave photons at the South Pole, one of the driest and most favorable observing sites on Earth for millimeter-wave photons. The observing EBEX bands are shown as shaded areas. The choice of a balloon-borne platform for EBEX greatly facilitates the observation at 410 GHz as compared to ground-based observations [30, 31].

Finally, EBEX will characterize the polarization of the galactic dust. EBEX will benefit from observing from above the atmosphere to study a dust-dominated signal at high frequencies. Figure 3–1 shows the EBEX frequency bands and the transmission through the terrestrial atmosphere at the South pole, one of the driest sites on Earth, and also, one of the best for millimeter wave observation. The low transmission at high frequencies motivates the choice of a balloon-borne platform for

[1] These precisions were derived by the EBEX collaboration and included in a proposal submitted to NASA.

EBEX. EBEX will determine the spectral index of dust and the amplitude of the dust polarization to 1.5% and 2%, respectively, with a 68% confidence level. EBEX is the first telescope optimized to measure the polarization of dust. Ground-based telescopes suffer from atmospheric absorption of photons and increased photon noise due to the terrestrial atmosphere emissions and fluctuations. The Planck satellite mission will also provide information about dust polarization on a timescale similar to EBEX. However, Planck is only sensitive to polarization up to 350 GHz and is optimized to observe larger angular scales than EBEX. The noise per pixel is therefore higher for Planck within the frequency bands EBEX will observe. EBEX is optimized to study dust in a smaller region of the sky known to be less contaminated by foregrounds.

3.2 Methodology

In order for EBEX to attain its science goals described in the previous section, its design and observing strategy have been optimized. This section describes the observing strategy EBEX will follow during its LDB flight as well as the methodology for the post-flight data analysis.

3.2.1 Observing Strategy

EBEX will measure the polarization and intensity of the CMB over the 350 square degree area in the Southern celestial sky shown in Figure 3–2 a). This region has been chosen for its low foreground emission properties between 130 and 450 GHz. Its size is chosen to optimize sensitivity to the large scale gravity wave induced B-modes given the current knowledge of dust.

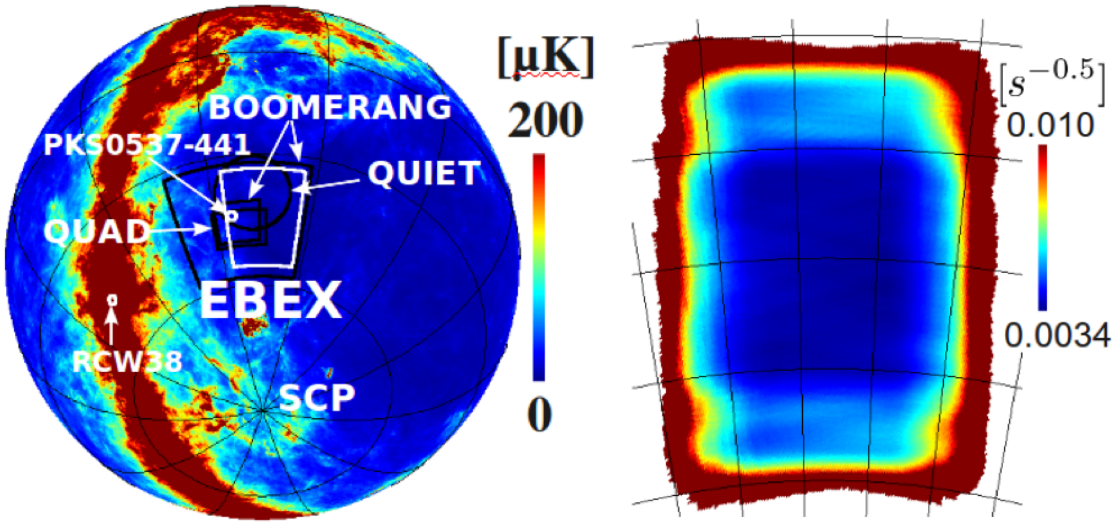

(a) (b)

Figure 3–2: Figure a) shows the area of the sky EBEX will observe in comparison to the past CMB experiments BOOMERanG, QUAD and QUIET. The galactic polarized HII region RCW 38 and the pulsar PKS 0537-441, which EBEX will calibrate from, are also shown. Figure b) shows the inverse square root of time spent observing the EBEX sky area (the sensitivity is obtained by a multiplicative factor). The sampling is almost uniform besides edge effects caused by the size of the focal planes. [Figure courtesy of Sam Leach, International School for Advanced Studies, SISSA]

EBEX will scan this area in azimuth at constant elevation over a 15° throw, back and forth, for a period of 83 s at a speed of $0.4°/s$. This azimuth scan will be repeated at 50 different elevations stepped by half a beam size. This procedure will be repeated 6 times over different sub-areas, every time covering $\sim$ 50 % of the previous sub-area. The entire 350 square degree area will be completely covered every half day. Those half day scans also include calibration scans over known polarized sources observed by BOOMERANG, the Balloon-borne Large-Aperture Submillimeter Telescope (BLAST), WMAP and Planck : the galactic HII region RCW 38 and the pulsar PKS 0537-441. The location of both sources relative to the

EBEX scanning area are shown in Figure 3–2 a). The entire EBEX area will be scanned twice a day repeating the 12 hour scan, but reversing the elevation stepping order. Figure 3–2 b) shows a simulated EBEX scan density map. The scan strategy maximizes the uniformity of the sampling. The edge effects are due to the finite size of the focal planes. Every non-edge point in the EBEX sky area will be visited by every pixel multiple times on the EBEX timescales : half-wave plate rotation (0.5 s), azimuth throw (41 s), sub-area scan (1 hour) and full area coverage (12 hours). The comparison of the multiple maps (2 maps/day) obtained will allow for the study and verification of systematic effects.

3.2.2 EBEX Science Analysis

As shown in Figure 2–6, EBEX is sensitive to angular scales of $20 \lesssim \ell \lesssim 1000$. EBEX is therefore not sensitive to the gravity wave peak generated during reionization at $\ell \sim 5$. The detection of this peak requires probing thousands of square degrees on the sky. Detection during a 11 day flight would require the EBEX telescope beam to be bigger. EBEX is optimized to detect the gravity wave peak generated at the surface of last scattering at $\ell \sim 100$ where its signal is maximised with respect to the gravitational lensing signal.

The response to optical signals from individual TES bolometers will be obtained by comparing the recorded signal to a known polarized source. EBEX will calibrate from RCW 38 and PKS 0537-441 since no planet will be observable by the telescope during the LDB flight. The responsivity and the beam of every detector will be obtained to better than 5% from scanning RCW 38 twice a day. The extended emission of this 4' source will be deconvolved using high resolution BLAST maps.

The responsivity will also be obtained to better than 5% at 150 and 250 GHz from comparison between RCW 38 calibrations and the WMAP temperature maps. As a cross-check for the beams, the fainter point source PSK 0537-441 will also be scanned and the beams will be verified by stacking the data from all detectors. Therefore, no information will be gained for individual detectors from PSK 0537-441.

The polarization of the CMB will be measured at every position in the scanned area. At every frequency, this vector field of polarization will be decomposed into the E and B-mode basis. The power spectrum of each component will then be computed. The galactic dust will dominate the measured B-mode signal at 410 GHz, will be comparable to the CMB B-mode signal at 250 GHz and will be dominated by the CMB B-mode signal at 150 GHz. The galactic dust will dominate the measured E-mode signal at 410 GHz and the CMB will dominate the E-mode signal at 250 and 150 GHz. The galactic dust will be characterized at high frequency, extrapolated to 150 GHz and subtracted from the 150 GHz measured signal. The dust, a grey body with an approximate temperature of 25 K, is expected to be small, but not negligible at 150 GHz.

The B-mode primordial gravity wave signal would be measured, if r is sufficiently high, at $\ell \lesssim 200$ in the power spectrum. The magnitude of this signal is directly related to the energy scale of inflation. The B-mode spectrum for $\ell \gtrsim 200$ is dominated by the gravitational lensing signal. The magnitude of the small scale component of the spectrum can be used to characterize gravitational lensing, measure the sum of the neutrino masses and probe the equation of state of dark energy.

3.3 Description of the EBEX Telescope

EBEX focuses incident photons into a cryostat with an off-axis Gregorian Mizuguchi-Dragone telescope designed with a parabolic 1.5 m diameter primary mirror and an ellipsoid 0.98 by 1.10 m secondary mirror. EBEX is designed to achieve 8' beams in order to be sensitive to CMB modes within $20 \lesssim \ell \lesssim 1000$. The largest angular scale is constrained by the size of the sky area EBEX will scan and the smallest scale is defined by the resolution of the telescope. Since EBEX is a balloon-borne telescope, it is designed to minimize the number of single point failure modes. Redundancy allows for the minimization of the risk of not recording and recovering science grade data after the flight.

The EBEX gondola, shown in Figure 3–3 a), physically supports the cryostat, the 300 K optics, the electronic crates, the pointing sensors, the power sources and the communication transmitters and receivers. It is composed of two main structures : the inner and outer frames. At float, the inner frame is tilted with respect to the outer frame to point between 30 and 60° in elevation. This range is chosen to minimize incident photons emitted by the ground and the balloon to enter the cryostat. Baffles are also installed on the outer frame to prevent photons from reflecting on the gondola structures into the cryostat. Figure 3–3 b) shows the baffles mounted to the gondola for the EBEX engineering flight. The payload is powered with Li-ion batteries that are recharged at float with solar panels. Batteries provide 28 V to the different subsystems which are converted to various voltages through DC to DC converters. The following sections describe the different subsystems present on the gondola.

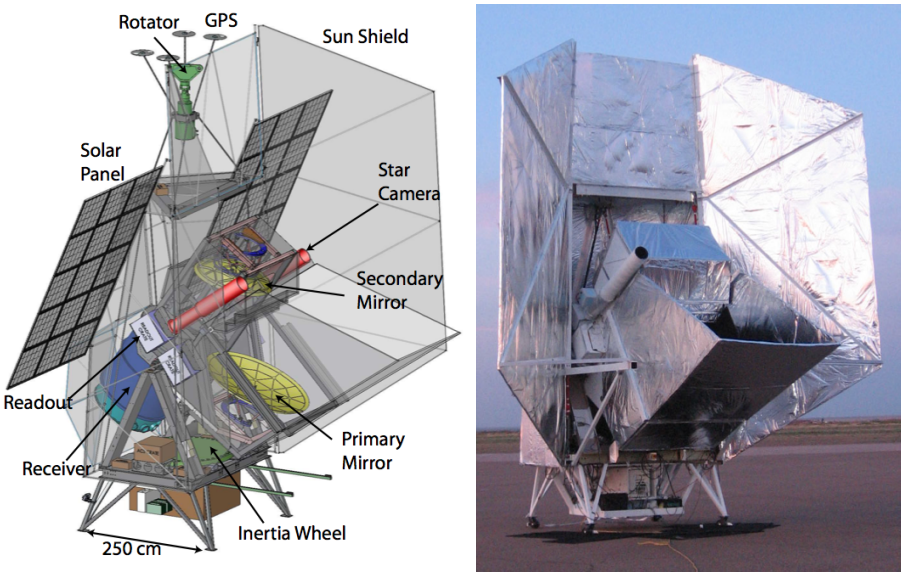

(a) (b)

Figure 3–3: The gondola is composed of the inner and outer frame. The inner frame supports the mirrors and the cryostat and tilts with respect to the outer frame. Baffles and solar panels are mounted to the outer frame. Figure a) shows a model of the EBEX gondola. Figure b) shows a picture of EBEX before its engineering flight. EBEX was not equipped with solar panels for this partially nocturnal flight and power was provided by batteries.

3.3.1 The Flight Control Software and Hardware

All EBEX subsystem controls are centralized and commanded by the flight control program (FCP), evolved from the software BLAST originally flew [32, 33]. Two fully redundant flight computers execute their own copy of the FCP, though only one computer is in charge of EBEX at a time. The FCP executes commands either uploaded from the ground or from a stored schedule on the flight computer. Those schedule files contain the flight plan : a preset list of commands to be executed under set conditions. The flight computers are part of a ring configured network with industrial Ethernet switches to allow redundancy by providing multiple network paths

between any two nodes in case of failure of any network point. Two redundant copies of the EBEX data are written to hard drives located in two separate pressure vessels.

Only a fraction of the data written to disk can be downlinked during the flight because of bandwidth limitations. A maximal subset of the bolometer timestreams as well as the readout housekeeping values, the realtime pointing solutions and the result files of the camera setup will be downlinked in priority. The remaining data, such as the payload position and altitude and the cryostat component temperatures, will be downlinked once the priority downlink is completed. A CSBF hardware package provides for the reception and transmission of commands that are transfered to the flight computers through serial communication. Communication with the payload is most effectively achieved through line of sight (LOS) direct communication. LOS is typically available during the first 12 to 24 hours of an Antarctica flight, depending on the wind speed. When LOS is not available, communication is achieved through the tracking and data relay satellite system (TDRSS) and Iridium satellite communication. The TDRSS downlinking is available for a fraction of each day depending on the satellite positioning : 6 hours per day at a latitude of 90° and 20 hours per day at a latitude of 85°. Iridium downlinking is always available when TDRSS is not. The addition of a TDRSS high gain antenna hardware package provides improved downlinking rate over standard TDRSS. EBEX will use the pulse-code modulation high gain antenna encoding, rather than the lower performing standard encoding. Table 3–1 shows the different downlinking speed performance.

The flight computers are synchronized in time with the different EBEX subsystems by two redundant timing servers clocked by high precision oven-controlled

Table 3–1: Downlinking speeds for the different available downlinking methods during the EBEX NA and LDB flights.

Downlink method	Maximal speed $\frac{kB}{s}$
Iridium	2
TDRSS	6
TDRSS high gain standard	75
TDRSS high gain pulse-code modulation	92
LOS	1000

625 kHz oscillators with 0.2 ppb precision. The oscillators will therefore drift by a maximum of 190 μs over the entire 11 day flight. The servers distribute Manchester encoded timestamp signals at a 6 Hz rate [34]. The subsystems re-synchronize their timestamp counter according to the time-servers signals and, between two such signals, achieve a precision to better than 5 μs with respect to the timeservers. This precision is required to align bolometer and pointing data accurately enough so EBEX achieves its science goals.

3.3.2 The Attitude Control System

The EBEX attitude control system (ACS) points the telescope and is composed of seven different types of sensors mounted to the EBEX gondola. These sensors provide redundant information to determine the azimuth, elevation and roll of the gondola or, equivalently, the right ascension (RA) and declination (DEC) of the sky-pointing. The pointing of the telescope need only be moderately accurate to 0.5° in real time, to achieve rough pointing. It is also required to be robust against faulty pointing, for instance caused by cosmic rays, to avoid destructive consequences such

as pointing at the Sun. The accuracy of the pointing reconstruction for the post-flight analysis is required to be 9" for EBEX to achieve its science goals.

The azimuth control is achieved by a rotator providing the mechanical link between the balloon and the gondola and is fine-tuned by a reaction wheel located on the outer frame. The elevation of the telescope is set by a linear actuator controlling the relative angle between the inner and the outer frame. The elevation drive is a single point failure mode for EBEX. To avoid excessive forces from being applied to the actuator at launch, a protective mechanism rigidly attaches the elevation actuator to the outer frame, but attaches it through a spring mechanism to the inner frame. The relative angle between the frames is fixed by a lock pin. After launch, the elevation actuator will be extended until it rigidly connects to the inner frame through a lockin mechanism and the lock pin will be disengaged, allowing the elevation to be controlled. This implementation was not present for the North American (NA) flight and was motivated by the bending of the elevation actuator at launch, as discussed in Section 6.1. It has been implemented for the LDB flight.

The seven ACS sensor types are listed in Table 3–2 with their precision for the measurements they enable. Every pointing coordinate can be redundantly determined by the implementation of multiple sensors to ensure robust pointing solutions in case of any sensor malfunction and unreliability or in case cosmic rays cause temporary biases. Two charge-coupled device (CCD) star cameras are optimized to detect stars from high altitude and are the most precise EBEX pointing sensors. Consequently, two identical star cameras are flown for redundancy. They allow absolute determination of azimuth and elevation, with precision of 5", and of roll, with

Table 3–2: The EBEX ACS sensors and their respective precision in azimuth, elevation, roll.

Sensor	Accuracy		
	Azimuth	Elevation	Roll
Star camera	5” *	5” *	3’ *
Gyroscope	11’ †	11’ †	11’ †
Magnetometer	12’ † 0.5° (NA) - 4° (LDB) *	—	—
Clinometer	—	1’ *	1’ *
Rotary encoder	—	20’ †	—
Sun sensor	14’ *	—	—
DGPS	20’ *	20’ *	40’ *

* Absolute precision.
† Relative precision.

precision of 3’, by comparing the star boresight pointing directly with the known location of stars on the sky. They are mounted on the inner frame. Two units each composed of three fiberoptic gyroscopes are mounted to the inner frame and individually measure relative rotation. Each unit allows for the determination of azimuth, elevation and roll with 11’ precision. A three-axis fluxgate magnetometer measures the relative azimuth to 12’ by determining the local magnetic field changes. When the measurements are compared to the magnetic model of the Earth, produced by the National Oceanic and Atmospheric Administration [35], an absolute precision is achieved. The precision depends on the inclination of the magnetic field vector and is 0.5° at the NA flight latitudes and 4° at the South Pole. Two clinometers measure the absolute elevation and roll of, respectively, the inner and outer frames by measuring the orientation of frames with respect to gravity, both to 1’. An absolute optical rotary encoder monitors the relative elevation angle between the inner and the outer

frame to 20'. Finally, four global positioning systems (GPS) rigidly attached to the rotator of the EBEX pivot each provide position, altitude and time. The formation of this four point antenna creates a differential GPS (DGPS) and allows the absolute determination of azimuth, elevation and roll to, respectively, 20', 20' and 40'. The DGPS has not yet been proven to work reliably on CSBF balloon flights.

A Sun sensor composed of a two-dimensional position sensitive diode identifies the azimuthal position of the Sun with a 14' accuracy. This sensor is also used to safeguard against pointing at the Sun. The absorption of such high optical power by the receiver could cause damage to the cold optical elements. EBEX will point within 45° of the anti-Sun direction at all times.

The star cameras record pictures of stars at the end of every azimuth half scan. Given the star cameras only furnish discrete solutions in time, other sensors are required to interpolate the pointing solutions. Pointing solutions are computed by the EBEX flight computer at 100 Hz, the fastest ACS sampling rate, using all non-vetoed sensors. The sensor's information are weighted by the inverse of the variance of their respective signal. The realtime solution computations are limited by processing time. The offline pointing reconstruction is performed under the same principle, but based on more complex and accurate algorithms and with user feedback to optimize the pointing results. The weight of the star camera solutions evolved by the gyroscope readings are set to be dominant to achieve more precise solutions [36].

3.3.3 The Receiver

The EBEX cryostat is mounted to the inner frame of the gondola as shown in Figure 3–3 a). The cryostat is composed of five isolated temperature layers in addition to its sub-kelvin cold stages. The inside layer is cooled to 4 K with liquid helium evaporation, the middle layer is cooled to 77 K with liquid nitrogen evaporation and the outside layer is at ambiant temperature ($\sim 300\ K$). In between those three layers, two vapor cooled shields (VCS) are cooled by helium and nitrogen vapor from inner layers to optimize the efficiency of the cryogenics [37]. The liquid helium and nitrogen tanks respectively hold 130 and 150 L. The cryogenics are helium limited and the helium boil-off rate is measured to be 0.35 L/h.

The CAD image of the EBEX cryostat is shown in Figure 3–4 a). An anti-reflection coated vacuum window seals the cryostat. Thermal filters installed at the 300, 77 and 4 K stages low-pass the incident power to minimize the thermal load on the lower temperature stages of the cryostat [39]. Inside the cryostat, the image of the primary mirror is re-imaged on a cold 22 cm aperture stop by an ultra high molecular weight polyethylene field lens. A rotative anachronous half-wave plate (HWP) is located by the aperture stop. The aperture stop image is then re-imaged on the focal planes by a pair of pupil lenses, a 43 cm polarizing grid and an additional camera lens. A picture of the optic box, the receiver components with a temperature below 4 K, is shown in Figure 3–4 b). The path of the photons through the cold optic elements is shown in Figure 3–5.

The lenses are fabricated and anti-reflection (AR) coated with techniques developed at Cardiff University. The HWP is AR coated by techniques developed at

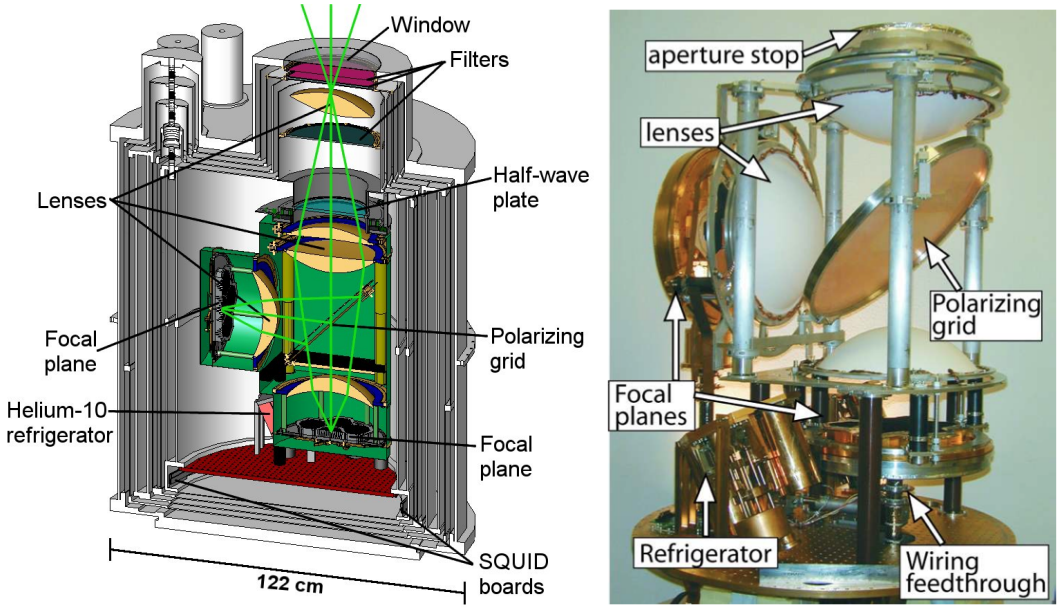

(a) (b)

Figure 3–4: Figure a) shows a CAD image of the EBEX cryostat. Thermal filters distributed at the 300 K, 77 K and 4 K cryostat stages low-pass filter photons. At 4 K, an anachronous HWP, located by an aperture stop, modulates the polarization of the signal. A polarization grid 45° inclined with respect to the incident photons reflects half the photons onto the V focal plane and transmit the other half onto the H focal plane. Ultra high molecular weight polyethylene lenses re-image the primary mirror onto the focal planes. Figure b) shows a picture of the EBEX optic box : the 4 K and below part of the camera [38].

Cardiff University and the University of Minnesota. The polarization grid is tilted 45° with respect to the incident photon path so half the photons, with a polarization aligned with the grid, are unaffected and reach the horizontal focal plane (H) and the other half, with a polarization perpendicular to the grid axis, are reflected onto the vertical focal plane (V). This allows both Q and U to be simultaneously measured on each pixel of the sky.

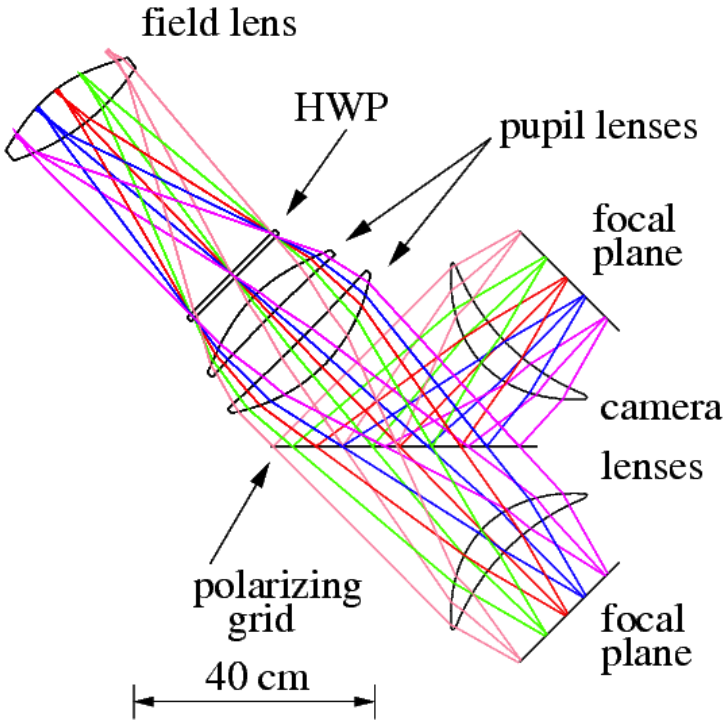

Figure 3–5: Optical path of photons in the EBEX cryostat. The primary mirror is re-imaged on the HWP by the field lens. A polarization grid separates the incident radiation in two orthogonal components onto two focal planes. Pupil and camera lenses focus the HWP image onto the focal planes [38].

The HWP is composed of five glued birefringent sapphire plates maintained at 4 K. It levitates on superconducting bearings to minimize friction while rotating and, therefore, dissipated power in the cryostat [40]. Each of the plates has its relative optical axis rotated with respect to the first plate by 0, 25, 85, 25 and 0°, respectively, to produce a polarization modulation efficiency superior to 98 % over the frequency range EBEX will observe. The relative orientation of the HWP is determined by an optical encoder that uses an LED emitting through a series of slots in the HWP mount [41]. The rotation of the HWP, at a frequency f_0, allows for the reduction

of systematic effects by modulating the signal to the sidebands of $4f_0$ where the 1/f noise is negligible. The angular symmetry of the HWP and the sensitivity of EBEX exclusively to the magnitude of polarization both modulate the signal by a factor of 2 with respect to the HWP rotation frequency f_0. The EBEX HWP is rotated at f_0=2 Hz.

The cold optics installed in the cryostat and the focal planes are thermally isolated by long vespel legs attached to the 4 K main plate. The optics are cooled to 1 K by a two stage $^4He/^4He$ absorption refrigerator to reduce optical loading on the detectors as the focal plane is cooled to 270 mK by a three stage $^4He/^3He/^3He$ absorption refrigerator. Both refrigerators are heat-sunk to the 4 K main plate. The refrigerators are controlled and the temperatures in the cryostat are read using housekeeping electronic boards designed at the Weizmann Institute of Science [42]. A refrigerator cycle keeps the focal planes cold for 3 days and consumes 10 L of helium. EBEX will have sufficient helium to operate its detectors for 11 days at float.

3.3.4 The Focal Planes

An EBEX focal plane is composed of four 150 GHz, two 250 GHz and one 410 GHz bolometer wafers arranged as shown in Figure 3–6 a). Low-pass metal-mesh filters and high-pass waveguides select the band-pass for each EBEX frequency band. In between, smooth-walled conical feed horns couple detectors to the sky. The bandwidth of the three frequency bands measured before the EBEX engineering flight are shown in Table 3–3 [43]. The size of the horns are frequency dependent, so the beams are not, to facilitate the post-flight analysis. Figure 3–6 b) shows the

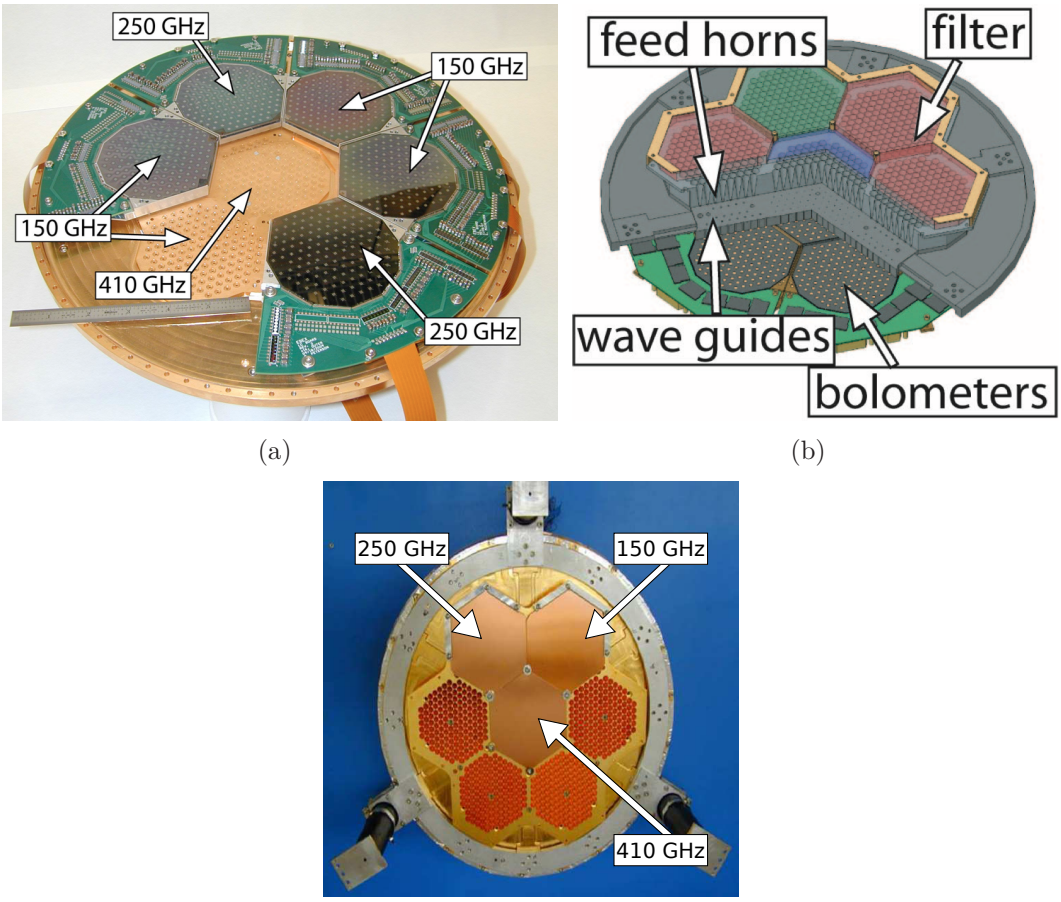

(a) (b)

(c)

Figure 3–6: Figure a) shows the bolometer wafer layout of a focal plane. Five wafers are shown with their LC-boards. Figure b) shows a cross-section of an EBEX focal plane CAD model. Low-pass metal-mesh filters define the high frequency edge of the band-pass. Smooth-walled conical feed horns couple the photons from the sky to the high-pass waveguides. Only the selected photons reach the bolometer wafers. Figure c) shows an EBEX focal plane configured for the EBEX engineering flight. The filters and conical feeds are visible.

cross-section of an EBEX focal plane CAD model. Figure 3–6 c) shows an EBEX focal plane configured for the EBEX engineering flight with only three wafers; only the filters and the horns are visible. EBEX will operate 872, 436 and 256 detectors

at 150, 250 and 410 GHz, respectively, for the LDB flight with a Strehl ratio superior to 0.9 across the entire focal plane and is therefore diffraction limited.

Table 3–3: Measured EBEX frequency bands.

Frequency Band Name GHz	ν_{low} GHz	ν_{high} GHz	$\bar{\nu}$ GHz	$\Delta\nu$ GHz
150	133	173	153	40
250	218	288	253	70
410	366	450	408	84

Individual bolometer wafers have 140 spiderweb bolometric transition edge sensors (TES). An EBEX pixel is shown in Figure 3–7 a). Wafers are produced by thin film deposition and optical lithography on silicon wafers. Every pixel is composed of a spiderweb absorber, eight low stress nitride legs, a bandwidth limiting gold thermal ballast and a transition edge sensor made of an aluminum and titanium bilayer. Figure 3–7 b) shows a TES located on its thermal ballast. To lower the bolometer thermal conductance with respect to ground-based experiment bolometers, such as APEX-SZ and SPT, the gold thermal bridge between the thermal bath and the TES is removed and the nitride legs are lengthened [44]. Chapter 4 describes in detail the operational principle of the bolometers.

The bolometer wafers are mounted with an LC board on an invar plate to increase the wafer robustness and to avoid differential thermal contractions. The electrical connections between the bolometers and the LC board traces are achieved with aluminum wire-bonds. The sub-kelvin multiplexing hardware is located on the LC boards. Low inductance microstrip cables are handmade from niobium-titanium flat wires sandwiched in Kapton tape. They were designed and developed at University

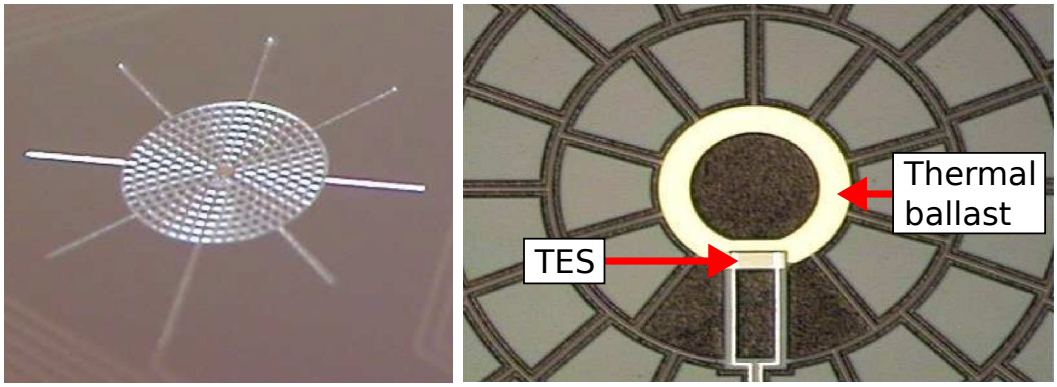

(a) (b)

Figure 3–7: Figure a) shows a picture of an EBEX spiderweb TES. Eight low stress nitride legs support the absorptive spiderweb with, in its center, an aluminum and titanium bilayer TES. Figure b) shows a zoom on the center Figure a). The TES is located on the gold thermal ballast at the center of the spiderweb absorber. The thermal ballast shown in Figure b) has been designed prior to the NA flight.

of Minnesota and fabricated both at University of Minnesota and McGill University [43]. They connect the superconducting quantum interference device (SQUID) boards, shown in Figure 3–8, to the LC boards. The microstrip cables are routed through a radio frequency tight tower which has low thermal conductance between the focal planes and the 4 K main plate. The SQUIDs, fabricated at the National Institute of Standards and Technology (NIST), are located at the 4 K stage [45]. The SQUIDs are protected by a Cryoperm[2] magnetic shield. The SQUID boards are

[2] www.cryopermshielding.com

wired to the 300 K electronics with Tekdata[3] cables fed through the different temperature stages of the cryostat. SQUIDs and multiplexing are thoroughly described in Chapter 5.

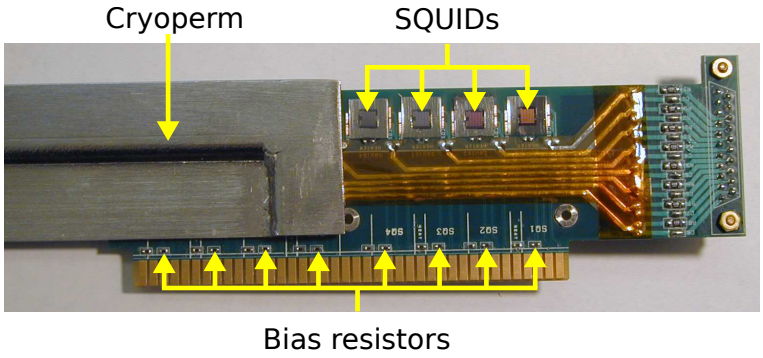

Figure 3–8: An EBEX SQUID board. Eight SQUIDs fabricated at NIST are protected by a Cryoperm magnetic shield. The 30 $m\Omega$ bias resistors are also mounted on this electronic board.

The SQUID biases are provided by SQUID controller and digital frequency multiplexing (DfMUX) electronic boards. The SQUID controller boards are located in a radio frequency interference (RFI) shielded can and the DfMUX boards are located in the bolometer readout crates (BRO) as shown in Figure 3–9. Given the high sensitivity of the EBEX detectors and SQUIDs to radio frequencies, the readout electronics are placed inside a Faraday enclosure. The BROs are connected to the RFI can through cables shielded in aluminum tubes. At the input of the RFI can, 1000 and 180 pF π-filters respectively filter the SQUID controller communication lines

[3] www.tekdata-interconnect.com

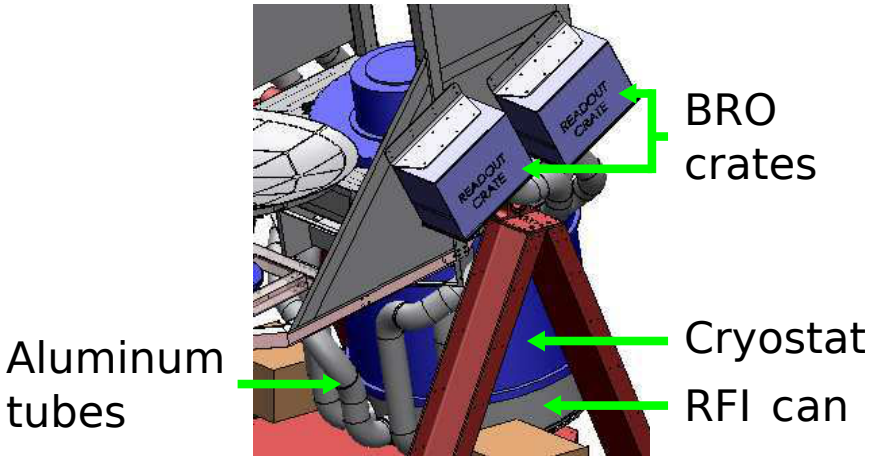

Figure 3–9: Model of the EBEX cryostat mounted on the gondola. The readout electronics are located in the bolometer readout crates and the RF can. Two readout crates are mounted per gondola side. Those enclosures are protected against radio-frequencies and are electrically connected with shielded cables fed through aluminum tubes.

and the bolometer biasing lines. The readout system and electronics are described in Chapter 5.

3.4 Summary

EBEX is designed with a mixture of technologies well proven to work at float and technologies specifically developed for EBEX and operated at float for the first time. For instance, the ACS system is inherited from BLAST and has flown in similar configurations many times, whereas the digital frequency domain multiplexing system, the EBEX spiderweb TES bolometers and rotating half-wave plate are being used in a space-like environment for the first time. The EBEX telescope is therefore a state of the art telescope designed and built to measure the B-mode polarization of the CMB while developing the technology and expertise for a potential future satellite mission.

CHAPTER 4
Bolometer Theory and Characterization

Bolometers absorb incident photons, converting them to thermal energy, and the measurement of their temperature-dependent resistance allows one to infer the power they absorbed. Transition edge sensor bolometers are superconductors, electrically biased within their superconducting transition, and thermally coupled to an absorber. They are ultra-sensitive because of their narrow superconducting transition and are commonly used in telescope focal planes to measure millimetre to far-infrared light. This chapter describes the concept, performance and operation of TES bolometers as well as the bolometer wafer characterization procedure.

4.1 Bolometer Thermal Conductance

The simplest bolometer model is shown in Figure 4–1. A bolometer with temperature T absorbs power with heat capacity C and has a weak thermal link with thermal conductance G to a thermal bath with temperature T_0. The dynamic thermal conductance is defined to be $G \equiv \frac{dP}{dT}$ and the average thermal conductance is defined to be $\bar{G} \equiv \frac{\Delta P}{\Delta T}$, where ΔT is the difference between the bolometer and the bath temperatures. In steady state, the bath temperature-dependent power flow through the system is described by

$$\bar{G}(T_0)\Delta T = \sum_i P_i, \tag{4.1}$$

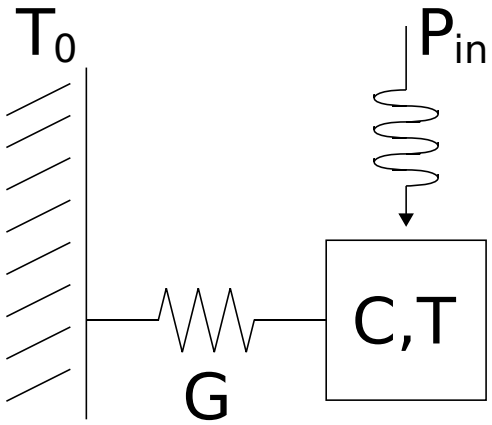

Figure 4–1: The simplest bolometer model. A bolometer with a temperature T and heat capacity C absorbs the input power P_{in}. The absorbed power is conducted to a thermal bath of temperature T_0 though a weak thermal conductance G.

where $\sum_i P_i$ is the sum of all the sources of incident power. For CMB applications, Equation 4.1 is commonly written as

$$\bar{G}(T_0)(T - T_0) \;=\; P_e + P_{rad}, \tag{4.2}$$

where P_e is the biasing electrical power and P_{rad} is the incident power absorbed by the bolometer. The contributions to the absorbed power are the CMB, the atmosphere, the components inside the cryostat, etc. From the definition of the thermal conductance, the temperature of a bolometer after the absorption of a power δP is given by

$$T \ = T_0 + \frac{\delta P}{\bar{G}} \left(1 \ - \ e^{-t/\tau_0}\right), \tag{4.3}$$

where $\tau_0 \ \equiv \ \frac{C}{\bar{G}}$ is the optical time constant of the bolometer.

The power transferred at a position x along the weak thermal link of the bolometer is governed by the Fourier heat conduction law

$$P(x) = A(x)\kappa(T)\frac{dT}{dx}, \tag{4.4}$$

where A(x) is the cross-section area of the link of length L, $\kappa(T)$ is the thermal conductivity of the link and $\frac{dT}{dx}$ is the thermal gradient across the link. The total power transferred across the link, in the steady state, is therefore

$$P = \frac{\int_{T_0}^{T} \kappa(T')dT'}{\int_0^L A^{-1}(x)dx}. \tag{4.5}$$

Assuming a cross-section area independent of x and the power law $\kappa(T) = \kappa_0 T^n$ for the thermal conductivity, where n $\in \Re$, Equation 4.5 becomes

$$P = \frac{A\kappa_0}{L}\frac{1}{(n+1)}(T^{n+1} - T_0^{n+1}). \tag{4.6}$$

From the definition of the dynamic thermal conductance and Equations 4.1 and 4.6, the dynamic and average thermal conductance are

$$G = \frac{A\kappa_0}{L} T^n; \tag{4.7}$$

$$\bar{G} = \frac{A\kappa_0}{L} \frac{1}{(n+1)} \frac{(T^{n+1} - T_0^{n+1})}{(T - T_0)}. \tag{4.8}$$

The division of the previous two equations yields the relation between the two different thermal conductances

$$\frac{G}{\bar{G}} = (n+1) \left[\frac{1 - (\frac{T_0}{T})}{1 - \left(\frac{T_0}{T}\right)^{n+1}} \right]. \tag{4.9}$$

This relation is important since the dynamic thermal conductance is relevant for the bolometer noise predictions, but is more challenging to measure than the average thermal conductance, as discussed in Section 4.6.

4.2 Electro-Thermal Feedback

Transition edge sensor bolometers are maintained in their superconducting transition with a biasing electrical current or voltage. A bolometer current bias of $P_e = RI^2$, where R is the bolometer resistance, would result in the positive electro-thermal feedback

$$\left(\frac{dP_e}{dT}\right)_+ = \frac{d}{dT}\left(RI^2\right) = I^2\frac{dR}{dT} > 0 \tag{4.10}$$

since $\frac{dR}{dT}$ is positive for a superconductor into its superconducting transition. A bolometer voltage bias of $P_e = \frac{V^2}{R}$ provides negative electro-thermal feedback

$$\left(\frac{dP_e}{dT}\right)_- = \frac{d}{dT}\left(\frac{V^2}{R}\right) = -\left(\frac{V}{R}\right)^2\frac{dR}{dT} < 0. \tag{4.11}$$

The absorbed power by a bolometer operated with current bias generates an increase in the bolometer temperature and thus, resistance. The feedback causes the bolometer to become normal and a TES bolometer operated with positive feedback is therefore a threshold detector. Conversely, the increase in the bolometer resistance due to the absorbed power by a bolometer operated with voltage bias decreases P_e and negative feedback maintains the bolometer into its superconducting transition. The sharp superconducting transitions ($\frac{dR}{dT} \gg 1$) creates strong negative electro-thermal feedback. Negative feedback is used to continuously monitor power fluctuations of a thermal source with TES bolometers and is well suited to CMB observations [46]. Other types of bolometers, such as neutron transmutation doped bolometers (NTD), have $\frac{dR}{dT} < 0$ and can therefore be stably used with negative feedback when current biased.

4.3 Responsivity

The responsivity $S_I \equiv \frac{dI}{dP}$ allows for the determination of the absorbed power from the measured current going through the bolometers. For the special case of a small incident power variation δP with angular frequency ω, the time dependent power flow portion of Equation 4.1 is

$$\begin{aligned} \sum_j \delta P_j e^{i\omega t} &= \frac{d(Pe^{i\omega t})}{dT}\delta T + \frac{d(Pe^{i\omega t})}{dt}\delta t \\ (\delta P_e + \delta P)e^{i\omega t} &= G\delta T e^{i\omega t} + i\omega C \delta T e^{i\omega t}. \end{aligned} \tag{4.12}$$

Defining the logarithmic slope of the superconducting transition $\alpha \equiv \frac{d(log(R))}{d(log(T))}$, positive for TES bolometers, and substituting $\delta P_e = \frac{dP_e}{dT}\delta T = -\frac{P_e \alpha}{T}\delta T$, Equation 4.12 becomes

$$\begin{aligned} \frac{\delta P}{\delta T} &= G + i\omega C + \frac{P_e \alpha}{T} \\ &= G(1 + i\omega\tau_0)[1 + \mathcal{L}(\omega)]. \end{aligned} \tag{4.13}$$

The loop gain $\mathcal{L}(\omega)$ is defined to be the negative ratio between the electrical and the incident power absorbed by the bolometers

$$\begin{aligned}\mathcal{L}(\omega) &= -\frac{\delta P_e}{(G+i\omega C)\delta T} \\ &= \frac{\mathcal{L}_0}{1+i\omega\tau_0}. \end{aligned} \tag{4.14}$$

The loop gain of ideal bolometers follows a single pole function with a DC loop gain of $\mathcal{L}_0 \equiv \frac{P_e \alpha}{GT}$. After defining the electro-thermal time constant

$$\tau_{ETF}(\mathcal{L}_0) \equiv \frac{\tau_0}{1+\mathcal{L}_0}, \tag{4.15}$$

the responsivity is finally evaluated by

$$\begin{aligned} S_I \equiv \frac{dI}{dP} = \frac{dI}{dT}\frac{\delta T}{\delta P} &= \frac{dI}{dR}\frac{dR}{dT}\frac{1}{\frac{\delta P}{\delta T}}. \\ &= -\left(\frac{\sqrt{2}}{V_{RMS}}\right)\left(\frac{\mathcal{L}_0}{1+\mathcal{L}_0}\right)\left(\frac{1}{1+i\omega\tau_{ETF}(\mathcal{L}_0)}\right), \end{aligned} \tag{4.16}$$

where V_{RMS} is the root mean square value of the sinusoidal bolometer voltage bias. The responsivity is a complicated function, but conveniently simplifies to $S_I \simeq -\frac{\sqrt{2}}{V_{RMS}}$ at low frequency when the loop gain is high [47].

4.4 Dynamic Range

The maximum power that can be absorbed by a bolometer while remaining in its superconducting transition, called the saturation power P_{sat}, is constrained by the power conducted to the thermal bath through the weak thermal link and the temperature difference between the bolometer and its bath. From Equation 4.2, the saturation power is the electrical biasing power required when no incident power is absorbed by the bolometer. In other terms, the saturation power is the maximum power the bolometer can absorb and still be operated in its superconducting transition. This power is given from Equation 4.4 by

$$P_{sat} = \frac{A}{L}\int_{T_0}^{T_c} \kappa(T')dT', \tag{4.17}$$

where T_c is the critical temperature of the bolometer. To maximize the usage of the bolometer dynamic range by photons instead of electrical biases and minimize the non-bolometric noise contributions to the bolometer performance, the ideal bolometer would have a saturation power equal to the absorbed optical load. However, the saturation of the bolometers must be avoided since it prevents photons from being detected and this ideal bolometer would have no dynamic range. The saturation power specifications have to allow for optical loading variations. This is achieved by increasing the saturation power, which comes at the expanse of additional noise due to the increased electrical biases required. Transition edge sensors have therefore to be optimized for the expected observing conditions of EBEX and the optimization of

the thermal conductance for the EBEX LDB flight bolometers is discussed in Chapter 7. Typically, ground-based telescopes operate bolometers with saturation power of tens of picowatts [48, 49]. Balloon-borne telescope bolometers have a saturation power of a few picowatts due to the smaller atmospheric power measured at high altitude.

4.5 Noise Performance

The detector noise performance directly impacts the receiver sensitivity. Demonstrating that the noise performance of the bolometers is understood and nominal is therefore of primary interest. This section describes the prediction and measurement of the noise performance of the system.

4.5.1 Noise Measurement Methodology

To extract the measured noise value for a SQUID or bolometer channel, a gradient is first subtracted from the timestream. The gradient models signals with minutes timescale not intrinsically related to the detectors, such as variations of the bolometer wafer temperature. A Hanning window is then applied to the timestream to minimize fast Fourier transform edge effects. The power spectral density (PSD) of the timestream is finally computed and the result is referred to as current through the SQUID coil.

During the NA flight, the detectors measured optical power at the half-wave plate rotation frequency and its harmonics. As a first step for all NA flight data analysis, a eight harmonic HWP template model with 33 parameters is fitted and subtracted from the data. The model is given by

$$HWP_{temp} = \sum_{n=1}^{8} A_n sin(n\omega t) + B_n t sin(n\omega t) + C_n cos(n\omega t) + D_n t cos(n\omega t), \quad (4.18)$$

where the parameters A_n, B_n, C_n and D_n are time dependent coefficients and the parameter ω is the angular HWP rotation frequency. This model is inspired by the Maxipol analysis [24]. The HWP rotation frequency is fitted to be 2 Hz. To avoid any potential confusion between HWP template residuals and white noise, the white noise level is quoted as the average of the power spectrum between 2.2 and 2.7 Hz, a frequency region that falls between harmonics and within the bolometer band ($\sim$15 Hz). The same frequency region is also selected for measurements without HWP template to avoid systematic effects. The measured to predicted noise ratio is finally quoted to account for the detector non-uniformity. The noise prediction is customized for every detector. The noise prediction is referred to as the current noise through the SQUID coil.

4.5.2 Noise Expectations

The readout electronic components and the bolometer Johnson, phonon and photon noise contribute to the noise performance of the detectors. In this thesis, the data are shown as demodulated current through the SQUID coil (i_n), equivalent to current noise through the bolometer, instead of the noise equivalent power (NEP) due to the absence of on-sky calibration for EBEX. The responsivity is used to convert power noise contributions at the bolometers to current noise at the SQUID coil.

The digital section of the readout system synthesizes the carrier and nuller biases and demodulates the recorded signal. Digitization and truncation noise are produced. Passive components and ICs from the analog electronics on the carrier, nuller and demodulator chains also generate noise. All the noise contributions from the 300 K components added in quadrature are subdominant in the camera noise performance. Appendix B shows in detail the contribution of all digital and electronic components.

The components dominating the cold readout electronic noise performance are the SQUID current-to-voltage converter and the bias resistor. The SQUIDs have a temperature of $\sim 5K$ and contribute 3.5 $\frac{\mathrm{pA}}{\sqrt{Hz}}$ to the noise performance of the camera. The noise contribution of the SQUIDs is empirically determined. The SQUID dominates the 4 K readout noise. The SQUIDs are required to be maintained substantially below their critical temperature of $\sim 8\ K$. The bias resistors R_{bias}, nominally 30 mΩ, produce voltage Johnson noise $\sqrt{4kT_{\mathrm{SQUID}}R_{bias}}$, where T_{SQUID} is the SQUID temperature. The bias resistors and the SQUIDs are located at the 4 K stage of the receiver to minimize their noise contributions while minimizing the number of wires reaching the detector stage to two.

The bolometers biased above their superconducting transition produce current Johnson noise $\sqrt{\frac{4kT_{bolo}}{R_{bolo}}}$, where T_{bolo} and R_{bolo} are the bolometer temperature and resistance, due to the intrinsic variations in their current. When biased in their superconducting transition, their Johnson noise is suppressed by $\frac{1}{1+\mathcal{L}_0}$ due to the negative electro-thermal feedback [50]. This reduction is small compared to the other sources of noise and can be neglected. The bolometers biased in their superconducting transition also produce the noise equivalent power phonon noise $\sqrt{\gamma 4kT_{bolo}^2 G}$ due to the

energy exchange between the TES phonons, where γ is a unit-less factor accounting for the temperature gradient across the thermal link. The term $\gamma^{1/2}T_{bolo}$ represents the effective temperature of the bolometer in the phonon noise [51]. It is the weighted mean temperature by the thermal conductivity of the thermal link. Assuming the mean free-path of the phonons present in the TES is short compared to the length of the thermal link L, this factor is

$$\begin{aligned} \gamma &= \frac{\int_{T_0}^{T} \left(\frac{T'\kappa(T')}{T\kappa(T)}\right)^2 dT'}{\int_{T_0}^{T} \frac{T'\kappa(T')}{T\kappa(T)} dT'} \\ &= \frac{n+1}{2n+3}\left(\frac{1-[\frac{T_0}{T}]^{2n+3}}{1-[\frac{T_0}{T}]^{n+1}}\right). \end{aligned} \tag{4.19}$$

The value of γ is typically 0.5 for EBEX bolometers.

Photon noise is also present when the bolometers are biased in their superconducting transition and its two spectral density terms are

$$\begin{aligned} NEP^2_{\gamma\ Pois} &= \int 2h\nu P_\nu d\nu \\ NEP^2_{\gamma\ corr} &= \xi \int \frac{c^2 P_\nu^2}{A\Omega\nu^2} d\nu, \end{aligned} \tag{4.20}$$

where P_ν is the spectral density of the photons, ν is the photon frequency, $A\Omega$ is the telescope throughput, h is Planck's contant, c is the speed of light and ξ is the photon correlation factor [52]. The first term corresponds to the variability in the photon

absorbed by the bolometers, following Poisson statistics, and the second term, to the photon correlation noise [53]. The parameter ξ is introduced to correct for the level of correlation. It is 0 for uncorrelated photons and is assumed to be 1 for polarized cameras. Since the bolometers integrate the incident power spectral density and $A\Omega \approx \lambda^2$ for a single-mode conical feed, Equation 4.20 can be approximated by

$$\begin{aligned} NEP_{\gamma\ Pois} &\simeq \sqrt{2h\nu P_{rad}} \\ NEP_{\gamma\ corr} &\simeq \sqrt{\xi \frac{P_{rad}^2}{\Delta\nu}}. \end{aligned} \tag{4.21}$$

Demodulation treats the measured signal, the phonon and the photon noise differently from the readout and the bolometer Johnson noise. Incident photon signals and phonon and photon noise all modulate the bolometer resistance and are indistinguishable. Phonon and photon noise are therefore subject to the same transfer function as incident photon signals. We assume a demodulated signal $y(t) = s(t)cos(\omega_c t)D(t)$, where s(t) is a photon incident signal, ω_c is the voltage bias angular frequency and D(t) is the demodulator function. By configuring a sinusoidal demodulator in phase with the voltage bias, the demodulated signal becomes

$$\begin{aligned} y(t) &= s(t)cos^2(\omega_c t) \\ &= \frac{s(t)}{2}[1 - cos(2\omega_c t)]. \end{aligned} \tag{4.22}$$

The $cos(2\omega_c t)$ term is digitally filtered out by the DfMUX system and the demodulated signal becomes

$$y(t) = \frac{s(t)}{2}. \tag{4.23}$$

For broadband sources of noise, such as the SQUID, and for broadband sources of noise bandwidth limited by the RLC bolometer filter (narrowband sources of noise), such as the bolometer Johnson noise, the white noise level can be decomposed into a series of sine-waves and the transfer function given by Equation 4.23 also applies individually to these components. However, the sidebands at frequencies above and below the voltage bias frequency add incoherently after demodulation and the white noise level is therefore increased by $\sqrt{2}$. For simplicity, the transfer function for incident signal is uniformly applied to the measured data and a demodulation enhancement factor is applied to the expected noise contributions of the readout components and the bolometer Johnson noise.

Table 4–1 shows the equations of the different sources of current noise referred to the SQUID coil. The demodulation enhancement factors of $\sqrt{2}$ are included. The phonon and photon noise are only present within the demodulated bandwidth of the bolometers ($\sim 15Hz$). The other broadband and narrowband sources of noise are limited by the FIR filter bandwidth of the DfMUX : 76 Hz at the FIR6 filter output for EBEX [54].

Table 4–1: Bolometer current noise contributions referred at the SQUID coil, as calculated in Appendix B.

Noise source	Equation $\frac{A}{\sqrt{Hz}}$
300 K readout	n/a*
4 K readout	$\sqrt{2} \times \left(3.5 \times 10^{-12} \oplus \frac{\sqrt{4kT_{SQUID}R_{30m\Omega}}}{R}\right)$
Bolometer Johnson	$\sqrt{2} \times \sqrt{\frac{4kT}{R}}$
Bolometer phonon	$S_I\sqrt{4kT^2G}$
Bolometer photon Poisson	$S_I\sqrt{2P_{rad}h\nu}$
Bolometer photon correlation	$S_I\sqrt{\xi\frac{P_{rad}^2}{\Delta\nu}}$

* Detailed calculations are shown in Appendix B.

An optimized experiment has a photon noise dominated receiver to optimize its sensitivity to incident signals since photon noise is the only source of noise intrinsic to photon detection. The readout system has to be designed to be a subdominant source of noise. The thermal conductance, the critical temperature and the normal resistance of the bolometers can be tuned in the fabrication process. According to Equation 4.2, the bolometer voltage bias is $V_b = \sqrt{R(\bar{G}(T - T_0) - P_{rad})}$ and from Equation 4.16, the responsivity can be written as

$$S_I \simeq \frac{\sqrt{2}}{V_b} = \sqrt{\frac{2}{R(\bar{G}(T - T_0) - P_{rad})}}, \tag{4.24}$$

assuming $\mathcal{L}_0 \gg 1$. The bolometer response therefore depends on the bolometer parameters, which are also constrained by the bolometer bath temperature and the incident power. Section 7.1 describes in detail the optimisation of these parameters.

4.6 Detector Characterization

The bolometers are required to be characterized before their noise performance can be predicted. The normal resistance (R_n), the critical temperature (T_c), the dynamic thermal conductance (G), the power law index of the weak thermal link conductance (n) and the electro-thermal feedback time constant (τ_{ETF}) of the bolometers must be determined. When detecting photons, the power absorbed (P_{rad}) is also required to be measured. This section describes the methodology followed to measure the EBEX bolometer characteristics and the power they absorb.

4.6.1 Pre-Characterization

The biasing frequency of each bolometer is set by an LC filter located on a circuit board wire bonded to the bolometer wafers. The inductors are fabricated at NIST and all have the same value across an eight inductor chip (13, 16 or 22 μH for the NA flight and 24 μH for the LDB flight). The different frequencies on a multiplexed module are defined by the capacitor values and the circuit diagram of a multiplexed module is shown in Figure 4–2 a). Due to the temperature dependence of the capacitor values, the bias frequencies have to be measured at sub-kelvin temperature. A network analysis is performed by stepping the frequency of a known voltage bias produced by the DfMUX and measuring the output current while the bolometers are maintained normal ($T_0 \sim 800$ mK). This methodology allows for the determination

of the normal resistance and the bias frequency (f_0) of the bolometers. The continuity of the bolometer wiring is also simultaneously verified. Raising the bolometer temperature above the bolometer superconducting transition improves the SQUID stability and accelerates the data acquisition since the resonant peaks are wider and easier to locate. Figure 4–3 a) shows such a network analysis for the multiplexed module #1 of the EBEX bolometer wafer 410-12, configured with a multiplexing factor of N=16.

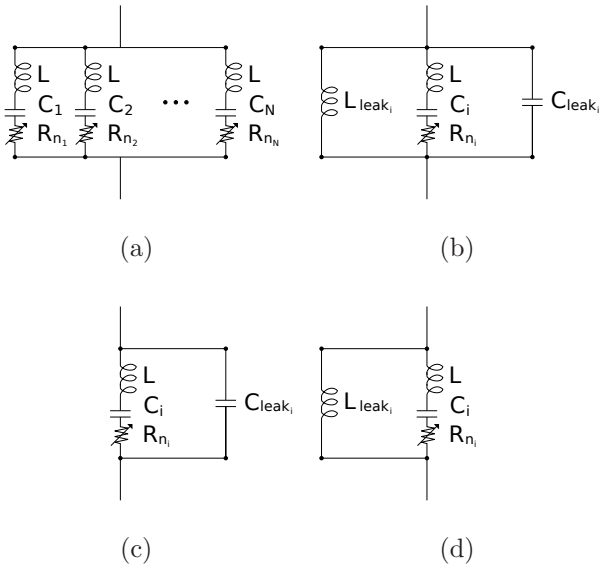

Figure 4–2: Figure a) shows the multiplexing circuit diagram : N bolometers are voltage biased in parallel and the bolometer frequencies are set by bandpass RLC filters. Figure b) shows the diagram assumed to determine the biasing frequency of the bolometer : the lower frequency bolometer branches are modeled by a leaking inductive branch and the higher frequency bolometer branches are modeled by a leaking capacitive branch. Figure c) and d) show, respectively, the models assumed to determine the lowest and the highest bias frequencies.

The impedance Z_{CLR_i} of the i^{th} bolometer in series with its LC filter on a multiplex module is given by

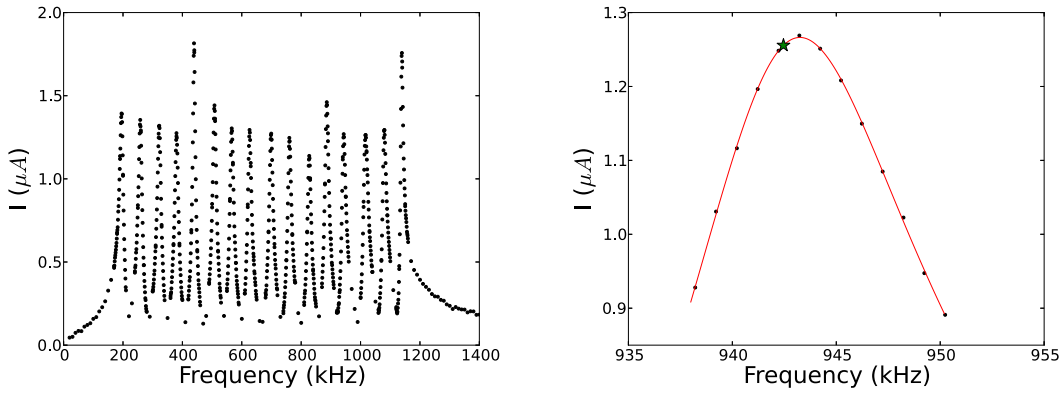

(a) (b)

Figure 4–3: Figure a) shows the network analysis for the multiplexed module #1 of the EBEX bolometer wafer 410-12 maintained at $\sim$ 800 mK. Figure b) shows a zoom of the 13^{th} peak of Figure a) with the modelling (solid line) of the RLC bandpass filter. The biasing frequency is shown with a green star.

$$Z_{CLR_i} = R_{n_i} + j2\pi f L \left[1 - \left(\frac{f_{0_i}}{f}\right)^2\right], \tag{4.25}$$

where f is the frequency of the voltage bias provided for the network analysis, L is the inductor value of the LC filter and $f_{0_i} = \frac{1}{\sqrt{LC_i}}$ is the resonant frequency of the i^{th} bolometer branch with a capacitor C_i. Every peak is modelled with a capacitive (C_{leak_i}) and inductive (L_{leak_i}) leakage branch in parallel with the Z_{CLR_i} impedance to represent the higher and lower frequency leakage, respectively. The lowest frequency peak in a network analysis is constrained to $L_{leak_i} \to \infty$ since no lower frequency leakage is possible and the highest frequency peak, to $C_{leak_i} = 0$ since no higher

frequency leakage is possible. This model is shown in Figure 4–2 b), c) and d). The current measured in the network analysis for the i^{th} bolometer is

$$I_i = V_b \left| \frac{1}{j2\pi f L_{leak_i}} + \frac{1}{Z_{CLR_i}} + j2\pi f C_{leak_i} \right|. \tag{4.26}$$

Figure 4–3 b) shows this model for bolometer 410-12-02-08, the 13^{th} peak of Figure 4–3 a). This model allows for the biasing of the bolometers with a bias frequencies f_{0_i}, maximizing the current through the individual bolometers, instead of biasing the bolometers with the frequencies at which the current through the multiplexed module has local maxima. Selecting the frequency at which the current through the multiplexed module is maximal would instead maximize the leakage current through the neighbouring bolometers, which would have the undesirable effect of increasing crosstalk. This bolometer is found to require a bias at $f_{0_{13}} = 942\ 459$ Hz and to have a normal resistance of $R_{n_{13}} = 1.85\ \Omega$.

4.6.2 First Characterization Method

Two different measurement techniques can be used to determine the critical temperature and the thermal conductance of bolometers. The simplest method is the direct measurement of these values. The critical temperature of the detectors can be obtained by measuring the bolometer resistance as a function of its temperature. A bias voltage of ∼70 nV is provided by the DfMUX boards and the output current is measured as the temperature of the bolometer wafer is slowly varied. Figure 4–4 shows such a measurement performed for bolometer 250-03-12-01.

Its critical temperature is measured to be 432 mK with a transition width of 6 mK. The error is dominated by the ruthenium dioxide temperature sensor uncertainty. During the measurement, the bolometer temperature change rate was ∼3 mK per minute. The wafer bath temperature was first set lower than the critical temperature of the bolometers and varied so the bolometers became normal twice. This procedure ensured the absence of hysteresis in the resistance curve. Hysteresis is observed when the voltage bias is too high, heating the bolometers and preventing them from equilibrating with the bath, or when the bolometer bath temperature is changed too quickly, not allowing the temperature sensor present on the invar mount of the wafer to thermalize with the bolometers. Hystereses increase the uncertainty on the measurement of the critical temperature when observed.

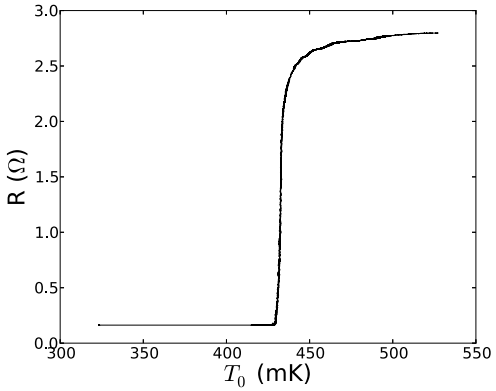

(a)

Figure 4–4: The measured resistance of bolometer 250-03-12-01 as a function of the bath temperature in the EBEX cryostat while the detectors were made dark by closing the cryostat window and covering over the feed-horns and waveguides.

The thermal conductance, averaged across the temperature gradient, can be estimated using $\bar{G} = \frac{P_{sat}(T_0)}{T_c - T_0}$. The saturation power is obtained by measuring the

current through the bolometer as a function of the applied voltage bias when the bolometer is dark and no photons are absorbed. The current through bolometer 410-06-08-12 as it is dropped into its superconducting transition to a resistance of 75% of its normal resistance is shown in the top panel of Figure 4–5. This bolometer wafer was operated in a testing cryostat without an optical window and was contained in a photon-tight box to ensure no photon were absorbed. The middle panel of Figure 4–5 shows the electrical bias power as a function of the applied voltage bias for the same bolometer. The lower panel of Figure 4–5 shows the bolometer resistance and the fraction of the bolometer resistance to its normal resistance as it is dropped into its superconducting transition.

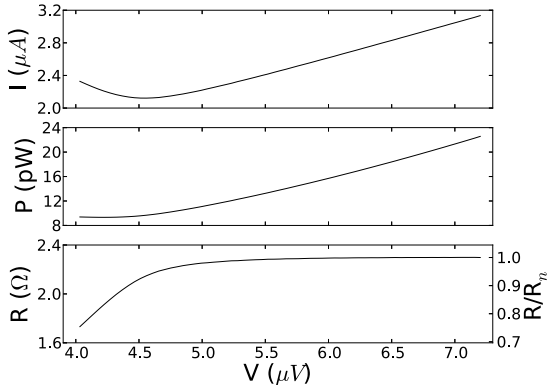

(a)

Figure 4–5: The current (top panel), the power (middle panel) and the resistance (lower panel) of bolometer 410-06-08-12 measured as the electrical voltage bias is decreased and the bolometer is dropped into its superconducting transition to a resistance of 75% of its normal resistance. The bolometer wafer is located in a light-tight box in a testing cryostat. The lower panel also shows the fraction of the bolometer resistance to its normal resistance as it is dropped into its superconducting transition.

The dynamic thermal conductance can afterwards be derived from Equation 4.9. However, obtaining the power law index of the thermal conductivity requires more complex measurements such as the one described in Section 4.6.3. We estimate the value of the power law index of the thermal conductivity to be 2 for EBEX. From Equation 4.19, the value of γ can also be calculated using the same estimation for the power law index of the thermal conductivity. Figure 4–6 shows the relative uncertainty on the dynamic thermal conductance and γ as a function of the critical temperature of the bolometer, assuming an uncertainty on the power law index of the thermal conductivity of $\sigma_n = 1$ and a bath temperature of 270 mK. The error introduced on the estimation of γ is small, but the error introduced on the thermal conductance is important. However, this methodology meets the requirements for a rudimentary noise estimation. The advantage of this method is its straightforwardness and its simplicity. Besides the critical temperature, all parameters are obtained for free while operating the detectors.

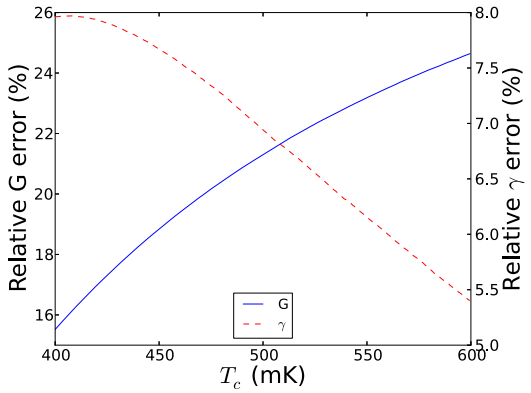

Figure 4–6: Relative error on the dynamic thermal conductance (solid line) and on γ (dashed line) assuming an uncertainty on the power law index of the thermal conductivity of $\sigma_n = 1$ and a bath temperature of 270 mK.

4.6.3 Second Characterization Method

The saturation power of the bolometers depends on the bath temperature according to Equation 4.6. The critical temperature of the bolometer and the power law index of the thermal conductivity can be obtained from fitting the measured saturation power of the bolometers in an environment closed to light as a function of the bath temperature. Figure 4–7 shows such a measurement performed on detector 250-G20-03-09 in the EBEX cryostat while the detectors were made dark by closing the optical window and taping over the waveguides and the conical feeds [30].

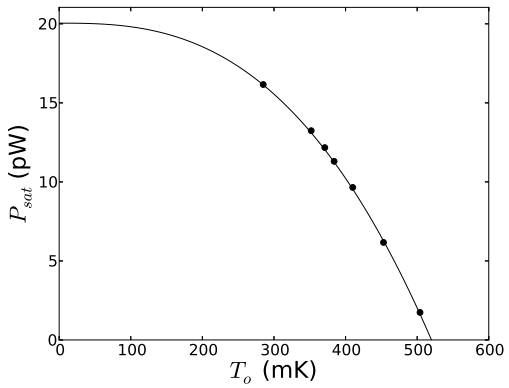

Figure 4–7: Saturation power as a function of the bath temperature for bolometer 250-G20-03-09 measured in the EBEX cryostat. The measured values (circles) and the model (line) are shown. The detectors were made "dark" by taping over the feed-horns and the waveguides.

The determination of the power law index of the thermal conductivity allows the dynamic conductance to be determined from Equation 4.7 and γ, from equation 4.19. This characterization method produces more precise dynamic conductance and γ parameters than with the characterization method presented in Section 4.6.2. However,

since the critical temperature of the detectors and their biasing parameters are a priori unknown when the bolometer wafer is first characterized, this method requires that the method presented in Section 4.6.2 is first performed so this measurement can be efficiently executed. Due to time constraints, this methodology is therefore not systematically performed on all characterized wafers.

4.6.4 Absorbed Power Determination

From Equation 4.1, the power absorbed by the bolometers is

$$P_{rad} = P_{sat_\gamma}(T_0) - P_{sat}(T_0). \tag{4.27}$$

The power absorbed by the bolometers is calculated by subtracting the saturation power of the bolometer measured dark P_{sat} from the bolometer saturation power when it absorbs light P_{sat_γ}. However, the previous statement is only true when both saturation powers are measured at the same bath temperature. The model shown in Figure 4–7 represents an important result since it allows for the electrical bias power to be determined if the saturation power is measured at a different bath temperature.

4.6.5 Electro-Thermal Feedback Time Constant

The electro-thermal time constant represents a measurement of the bolometer response to thermal fluctuations. Figure 4–8 shows a more accurate model of a TES bolometer than the model presented in Section 4.1. A spiderweb absorber is in contact with a bath temperature through weakly conducting legs with thermal conductance G. A TES is in thermal contact with a gold thermal ballast with thermal

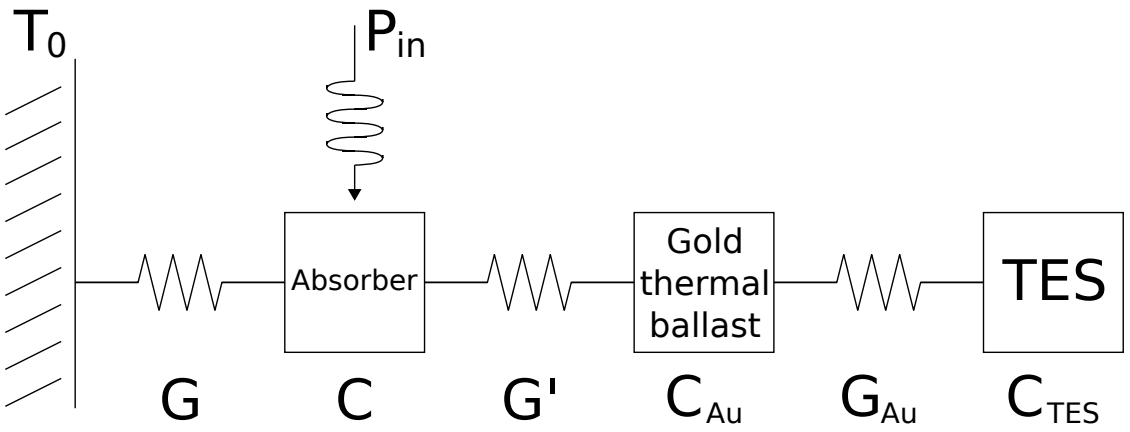

Figure 4–8: The TES bolometer model. The incident power is absorbed by an absorber of heat capacity C in thermal contact with a thermal bath of temperature T_0 though a weak thermal conductance G. The absorber is in thermal contact with a gold thermal ballast of heat capacity C_{Au} through a link of thermal conductance G'. The temperature of the bolometer is measured by a TES with a heat capacity C_{TES} in thermal contact with the thermal ballast through a thermal conductance G_{Au}.

conductance G_{Au}. This thermal ballast is in thermal contact with the absorber with thermal conductance G'. By design, the thermal conductance between the TES and the bath is small so a negligible amount of heat is conducted through the leads, the TES is strongly coupled to the thermal ballast ($G_{Au} \gg G$) and the thermal ballast is strongly coupled to the spiderweb absorber ($G' \gg G$). The TES, the gold thermal ballast and the absorber have a heat capacity C_{TES}, C_{Au} and C, respectively. The thermal time constant associated with the absorber is $\tau_0 = \frac{C}{G}$. The role of the gold thermal ballast is to slow the response of the TES so it responds slower to optical signal than to electrical bias and $C_{TES} \ll C_{Au}$. A strong thermal contact is achieved between the TES and the gold ballast and the time-constant from the TES is therefore $\tau_{0\ TES} \approx \frac{C_{Au}}{G}$. If the TES responds more quickly to optical signal than

the absorber, the bolometer can oscillate and become unstable. The electro-thermal time constant of the bolometer is given by Equation 4.15.

To measure the electro-thermal feedback time constant of a bolometer biased with a carrier signal $V_b cos(\omega_c t)$, an additional test signal $V_h cos([\omega_c + \delta\omega]t)$, where $V_h \ll V_b$ and $\delta\omega$ is the angular frequency difference between the voltage bias and the test signal, is injected on the carrier wire [55]. The power biasing the bolometer is therefore

$$\begin{aligned} P_e &= \frac{V_{Total}^2}{R_{bolo}} \\ &= \frac{1}{R_{bolo}} \left\langle \left(V_b cos(\omega_c t) + V_h cos([\omega_c + \delta\omega]t) \right)^2 \right\rangle_{\tau_{ETF}} \\ &= \frac{1}{R_{bolo}} \left\langle V_b^2 cos^2(\omega_c t) + 2V_b V_h cos(\omega_c t) cos([\omega_c + \delta\omega]t) + V_h^2 cos^2([\omega_c + \delta\omega]t) \right\rangle_{\tau_{ETF}} \\ &\simeq \frac{1}{R_{bolo}} \left[\frac{V_b^2}{2} + V_b V_h cos(\delta\omega t) + \frac{V_h^2}{2} \right], \end{aligned} \tag{4.28}$$

after averaging over the time constant of the bolometer. The application of the additional carrier signal modulates the response of the bolometer at a frequency $\delta\omega$. The bolometer response is therefore amplitude modulated according to the voltage bias $[V_b + V_h cos(\delta\omega)]cos(\omega_c t)$. The mixing of the bolometer response with a demodulator $cos(\omega_d t)$ yields to a measured current going through the bolometer of

$$
\begin{aligned}
I &= \frac{1}{R_{bolo}}\Big[[V_b + V_h cos(\delta\omega t)]cos(\omega_c t)\Big]cos(\omega_d t) \\
&= \frac{V_b}{2R_{bolo}}\Big[cos([\omega_c - \omega_d]t) + cos([\omega_c + \omega_d]t)\Big] \\
&\quad + \frac{V_h}{4R_{bolo}}\Big[cos([\omega_c - \omega_d - \delta\omega]t) + cos([\omega_c + \omega_d - \delta\omega]t) \\
&\quad + cos([\omega_c - \omega_d + \delta\omega]t) + cos([\omega_c + \omega_d + \delta\omega]t)\Big]. \qquad (4.29)
\end{aligned}
$$

The demodulated current generated by the voltage bias $V_b cos(\omega_c t)$ is split in two components with frequencies $\omega_c \pm \omega_d$ and amplitude $\frac{V_b}{2R_{bolo}}$. Each of these two currents has two smaller current components present in their sidebands generated by the additional amplitude modulating voltage bias $V_h cos(\delta\omega t)cos(\omega_c t)$. Those four sideband currents have frequencies $\omega_c - \omega_d \pm \delta\omega$ and $\omega_c + \omega_d \pm \delta\omega$ and amplitude $\frac{V_h}{4R_{bolo}} \ll \frac{V_b}{2R_{bolo}}$.

The bias frequency is set between 200 and 1 200 kHz. The demodulator frequency is usually set to the carrier frequency, but specifically for this test, it is set to $\omega_d = \omega_c - \delta\omega - \Omega$. Since $\delta\omega$ is a value smaller than a kiloHertz and Ω is arbitrarily set to 24 Hz, the $\omega_c + \omega_d$ carrier signal and its sidebands are digitally filtered by the DfMUX system and the measured current becomes

$$
I = \frac{V_b}{2R}cos([\delta\omega + \Omega]t) + \frac{V_h}{4R}\Big[cos(\Omega t) + cos([2\delta\omega - \Omega]t)\Big]. \qquad (4.30)
$$

The thermal response of the bolometer is measured at a frequency Ω as the response at a frequency $2\delta\omega - \Omega$ also contains its ohmic response. Figure 4–9 a) shows the PSD of such a measurement performed for bolometer 410-06-08-09 dropped to 75% of its normal resistance into its superconducting transition with an additional carrier with $\delta\omega = 9$ Hz.

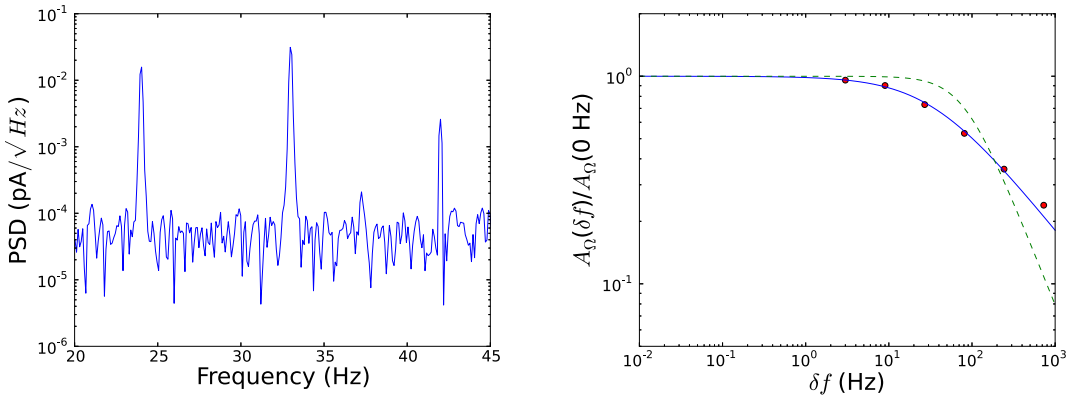

(a) (b)

Figure 4–9: Figure a) shows the PSD of the bolometer 410-06-08-09 biased at 75% of its normal resistance with a voltage bias and a test signal separated by $\delta f = 9$ Hz in the frequency domain. The 24 Hz peak shows the thermal response of the bolometer and the 42 Hz peak also shows the ohmic response of the bolometer. The 33 Hz peak shows the applied voltage bias. Figure b) shows the thermal response of the same bolometer as a function of $\delta\omega$ (points) with a single pole model (dashed line). Since the bolometer response does not follow a single pole, a generic fit is also shown (solid line). The electro-thermal time constant is found to be 4.7 ms when biased at 75% of its normal resistance.

The value of $\delta\omega$ is varied from 3 to 243 Hz. The amplitude of the response measured at the demodulated frequency Ω follows a single pole response as a function of $\delta\omega$ if $\tau_{0\ TES} \ll \tau_0$:

$$A_\Omega(\delta f) = \frac{A_0(\mathcal{L}_0)}{\sqrt{1 + \left(\frac{\delta f}{f_{ETF}(\mathcal{L}_0)}\right)^2}}, \tag{4.31}$$

where $A_0(\mathcal{L}_0)$ is the DC amplitude of the electro-thermal response and $f_{ETF}(\mathcal{L}_0) = \frac{1}{2\pi\tau_{ETF}(\mathcal{L}_0)}$. Figure 4–9 b) shows such a model for bolometer 410-06-08-09 dropped to 75% of its normal resistance into its superconducting transition and its electro-thermal time-constant is found to be 4.7 ms. The EBEX bolometers do not typically follow a single pole. By measuring the electro-thermal time constant of a bolometer at various positions in its superconducting transition, i.e. different loop gains, the DC time constant $\tau_{0\ ETF}$ can be evaluated from Equation 4.15.

4.7 Characterization Results

After the bolometers are characterized, the bolometer wafers are ranked according to their expected performance for the EBEX LDB flight. The bolometer electro-thermal time-constant typically meets the requirement of ∼10 ms. An ideal wafer would have uniform bolometer characteristics meeting the specifications derived in Section 7.1. In practice, the parameters have a distribution. For example, the bolometers on wafer 150-43 have a saturation power of 9.0 pW with an RMS deviation of 2.3 pW, measured in a light tight box while the bath temperature was 250 mK. The distribution is shown in Figure 4–10 a). The distribution is narrow and 95% of the bolometers measured are above the specified saturation power of 4.8 pW, minimizing the number of bolometer potentially saturating at float. Their critical temperature is 478 mK with an RMS deviation of 24 mK and the distribution

is shown in Figure 4–10 b). The bolometer wafer 150-43 is therefore considered a potential flight wafer.

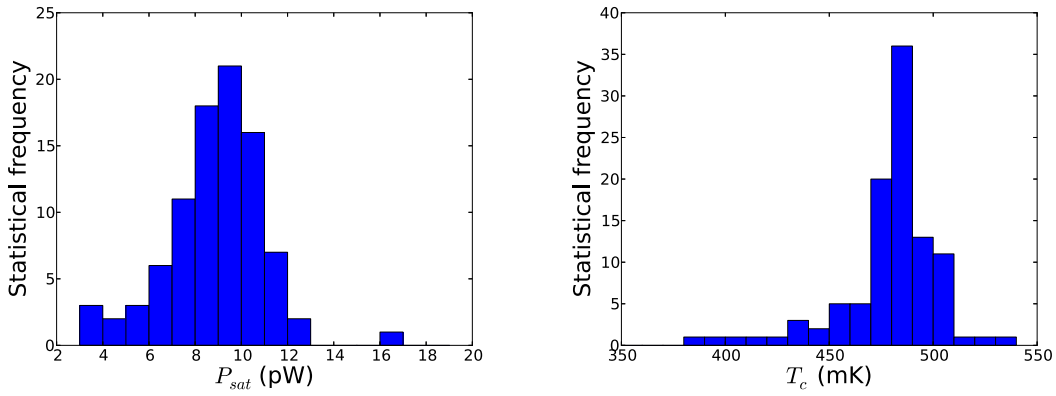

(a) (b)

Figure 4–10: Figure a) shows the distribution of saturation power measured while the bath temperature was 250 mK on bolometer wafer 150-43 located in a light tight box. Figure b) shows the distribution of critical temperature measured on the same bolometer wafer 150-43. This wafer is a candidate to be flown for the EBEX LDB science flight.

The bolometer wafer 150-41 has a saturation power of 17.5 pW with an RMS deviation of 3.4 pW, measured in a light tight box while the bath temperature was 250 mK, not accounting for the outlying saturation powers above 30 pW. The distribution is shown in Figure 4–11 a). The saturation power of the bolometers on this bolometer wafer range from 1.8 to 6.4 times the specified saturation power. The bolometer wafer 150-G19 has a bimodal critical temperature distribution, as shown in Figure 4–11 b). Moreover, 79% of the bolometers have a critical temperature above 1 K, which is much higher than the specified 420 mK. Both of these bolometer wafers are not demeaned to be science grade and will not be used for the EBEX LDB flight.

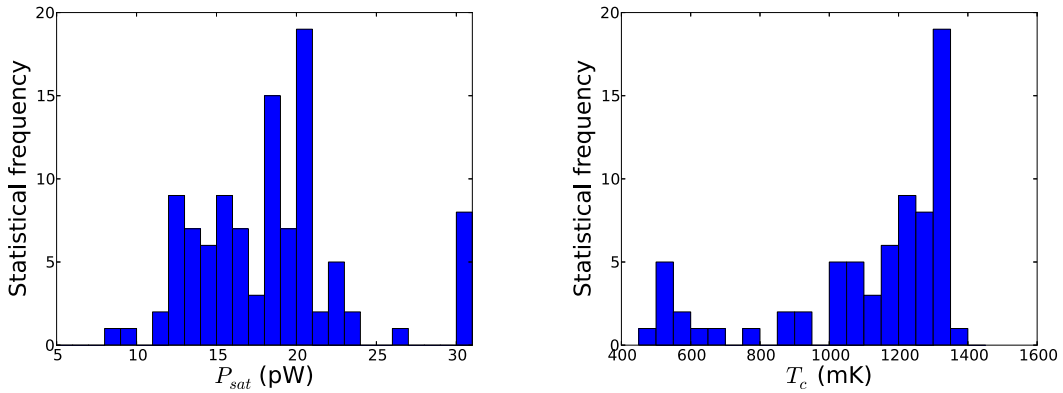

(a) (b)

Figure 4–11: Figure a) shows the distribution of saturation power measured while the bath temperature was 250 mK on bolometer wafer 150-41 located in a light tight box. All bolometers in the last bin have a saturation power distributed between 30 pW and 177 pW. The average saturation power is 3.5 times the specified value, not considering the outlying values above 30 pW. Figure b) shows the distribution of critical temperature measured on bolometer wafer 150-G19 in a light tight box, which is bimodal and has 79% of its values above 1 K. Both of these wafers will not be used during the EBEX LDB flight.

From the tens of bolometer wafers fabricated, the 14 bolometer wafers optimizing the camera sensitivity, shown in Table 4–2, have been selected. This selection is based on the relative sensitivity of the bolometer wafers which is quantified by the mapping speed. For a single bolometer, the mapping speed is defined to be

$$M_S^{bolo} = \frac{NEQ,U}{\sqrt{\Omega_s}}, \tag{4.32}$$

where NEQ,U is the noise equivalent temperature for the Q and U polarization and Ω_s, the solid angle of the bolometer beam. The NEQ,U represents the required

Table 4–2: List of bolometers wafers selected to populate the two EBEX focal planes during the LDB flight. The NEQ,U for the average bolometer on each wafer and the mapping speed of each bolometer wafer are also shown.

Bolometer wafer	Bolometer NEQ,U $\mu K\sqrt{s}$	M_s^{wafer} $\mu K\sqrt{\frac{s}{deg^2}}$
150-03	177	221
150-09	249	222
150-15	183	161
150-20	173	152
150-24*	256	234
150-39	238	221
150-41	284	235
150-43	210	186
250-10	766	734
250-23	705	619
250-24	700	608
250-29	710	690
410-16*	1.08×10^4	9.56×10^3
410-18*	1.04×10^4	9.11×10^3

* A neutral density filter with 50% optical efficiency is assumed to avoid bolometer saturation.

temperature of a polarized source that fills the beam with uniform surface brightness to produce an incident signal on the bolometers such that the signal-to-noise ratio is one. In this thesis, the NEQ,U is referred to the CMB since EBEX will be detecting its millimeter-wave photons. The conversion from NEP, described in Section 4.5.2, to NEQ,U is

$$NEQ,U = \frac{NEP}{\sqrt{2}\eta}\frac{dT}{dP}\Big|_{T_{CMB}}\frac{1}{A\Omega_s BW}, \tag{4.33}$$

where η is the end-to-end efficiency of the telescope and receiver, $\frac{dP}{dT}\Big|_{T_{CMB}}$ is the conversion gradient from power to temperature, $A\Omega_s$ is the telescope throughput and BW is the observing bandwidth. Typical end-to-end efficiencies of 21, 14 and 8.4% for the 150, 250 and 410 GHz EBEX observing frequency bands are assumed.[1] The conversion factor is derived from the blackbody spectral density of the CMB with temperature T_{CMB} and is

$$\frac{dP}{dT}\Big|_{T_{CMB}} = \left\langle \frac{c^2 k T_{CMB}^2}{2h^2\nu^4}\frac{(e^{\frac{h\nu}{kT_{CMB}}}-1)^2}{e^{\frac{h\nu}{kT_{CMB}}}} \right\rangle_{band}. \tag{4.34}$$

[1] The telescope and receiver transmission coefficients are calculated in Section 7.1.1. Bolometer absorption efficiencies of 60, 50 and 40% are assumed for the 150, 250 and 410 GHz bolometers, respectively.

The telescope throughput is approximated to be $A\Omega_s \approx \lambda^2$, consistent with the single-moded conical feed optical system employed for EBEX. The NEQ,U units are $K\sqrt{\frac{s}{deg^2}}$ and the factor of $\sqrt{2}$ in Equation 4.33 is due to the Nyquist frequency of a 1 Hz band being $\frac{1}{2}$ Hz when converting from $\frac{1}{\sqrt{Hz}}$ to $\sqrt{s}$. In the presence of a neutral density filter, the $\frac{dP}{dT}$ is increased by the inverse of the photon loss.

The n_b bolometers sensitive to light on a bolometer wafer contribute to its mapping speed M_S^{wafer}. Assuming the bolometer wafers are perfectly uniform, the mapping speed of a bolometer wafer is approximated to be

$$M_S^{wafer} = \left(\sum_{i=1}^{n_b} \frac{1}{\left(M_S^{bolo_i}\right)^2} \right)^{\frac{-1}{2}} \approx \frac{M_S^{bolo}}{\sqrt{n_b}}. \tag{4.35}$$

Table 4–2 presents the mapping speed of the 14 bolometer wafers currently identified as the best candidates for the LDB science flight. Since new wafers are still being fabricated, some of these wafers may be replaced with new ones.

Three bolometer wafers have saturation powers below specifications, which requires the use of a neutral density filter to attenuate the incident loading by 50% to avoid bolometer saturation. The filters will cause the signal-to-noise from those bolometers to decrease since half of the photons will be reflected, yet none of the detector noise will be attenuated. Nevertheless, due to high bolometer yield, these wafers represent the most sensitive bolometer wafers presently available for EBEX. In parallel to the Summer 2012 EBEX integration, the fabrication of 410 GHz bolometer wafers with higher saturation power to replace 410-16 and 410-18 for the LDB

flight has been emphasized. The University of California, Berkeley team is also fabricating detector wafers in the 150 and 250 bands, and several wafers are presently being characterized. The 14 bolometer wafers presented in Table 4–2 meet the EBEX requirements for sensitivity.

The combined mapping speed of all the bolometers observing the same frequency band is

$$M_S^{band} = \left(\sum_{j=1}^{n_{wafer}^{band}} \sum_{i=1}^{n_{b_j}^{band}} \frac{1}{\left(M_S^{bolo_{ji}^{band}} \right)^2} \right)^{\frac{-1}{2}}, \tag{4.36}$$

where n_{wafer}^{band} is the number of bolometer wafers observing within the given frequency band, $n_{b_j}^{band}$ is the number of bolometers on the j^{th} wafer observing within the given frequency band and $M_S^{bolo_{ji}^{band}}$ is the mapping speed of the i^{th} bolometer of the j^{th} wafer observing within the given frequency band. The mapping speed within the 150, 250 and 410 GHz EBEX observing bands are calculated to be 69.3, 328 and 6.60 $\times 10^3$ $\mu K \sqrt{\frac{s}{deg^2}}$, respectively. The noise per pixel is calculated by multiplying the mapping speed of the whole EBEX camera, obtained by combining the mapping speed of the three EBEX observing bands, by $\sqrt{\frac{A_{pixel}}{\Delta t_{obs}}}$, where A_{pixel} is the size of a pixel beam and Δt_{obs} is the total observing time. These bolometer wafers allow EBEX to reach a depth of 1.5 μK_{RMS} across 350 square degrees with 11 days of observations, assuming the CMB will be observed 80% of the time.

4.8 Summary

A series of bolometer wafers were produced and characterized and enough LDB flight grade wafers, such as bolometer wafer 150-43, have been produced to populate the 14 positions in the EBEX focal plane. However, the total number of detectors can still be increased. The uniformity and average value of the different bolometer parameters can still be improved to maximize the EBEX sensitivity. Bolometer wafers will therefore continue to be produced and characterized until the final integration of EBEX in Antarctica.

CHAPTER 5
The EBEX Readout Electronics

The polarization of the CMB was first detected by DASI [2] and its E-mode spectrum, by CBI [21]. The BOOMERanG experiment was the first to measure the polarization of the CMB with bolometers [56]. Other experiments, such as CAPMAP [23], MAXIPOL [57], the BICEP experiment [25], QUaD [58] and WMAP [26] have since improved the precision of the measurement of the E-mode polarization of the CMB. To measure the B-mode polarization generated by the primordial gravitational waves, the sensitivity of telescope cameras is required to be improved and is achieved by increasing the number of detectors present in their focal planes. The number of wires connecting the room-temperature electronics to the sub-kelvin detectors limits the number of TES detectors by increasing the heat load on the sub-kelvin stage. To operate kilopixel focal planes of TES bolometers while respecting the camera cryogenic heat load budget, the readout is required to be multiplexed. This chapter describes the theory of operation of superconducting quantum interference devices, the different multiplexing techniques currently developed and the EBEX readout system.

5.1 SQUIDs

Transition-edge sensor bolometers are low noise devices and typically have a resistance of 0.1-1 Ω. Therefore, the current through the bolometers must be first amplified with a low noise and low input impedance amplifier. Superconducting

quantum interference devices meet those constraints and are used to convert the magnetic flux generated by the current through the SQUID coil into an output voltage. The SQUIDs used for multiplexing TES bolometers are described in this section.

A Josephson junction is created by interrupting a superconducting material by a thin layer of normal material. If the thickness of the link is small compared to the coherence length of the Cooper pairs present in the superconductor, the Cooper pairs tunnel through the link. A voltage difference is then produced across the link. A SQUID is composed of two identical parallel Josephson junctions forming a closed loop and their operation relies on the quantization of the magnetic flux in the loop. Its voltage response to magnetic flux is derived in Appendix A. A SQUID is characterized by its coil inductance L_i, its inductance L_{SQ_i}, its flux to voltage conversion factor $\frac{dV_i}{d\Phi}$ and its mutual inductance $M_i = \alpha\sqrt{L_i L_{SQi}}$, where α is a geometric coupling factor. The output voltage of the SQUID is

$$V_i = I M_i \frac{dV_i}{d\Phi}. \tag{5.1}$$

To increase the signal-to-noise ratio, N_{SQ} single-SQUIDs are connected in series as shown in Figure 5–1. The total voltage difference across a SQUID-array is

$$V = \sum_{j=1}^{N_{SQ}} V_i = N_{SQ} V_i. \tag{5.2}$$

However, the noise contributions of the individual SQUIDs $i_{n\ SQ_i}$ add in quadrature and the total noise of the N_{SQ}-element SQUID array is

$$i_{n\ SQ} = \sqrt{\sum_{j=1}^{N_{SQ}} i_{n\ SQ_i}^2} = \sqrt{N_{SQ}} i_{n\ SQ_i}. \tag{5.3}$$

The signal-to-noise of a N_{SQ}-element SQUID-array therefore increases as $\sqrt{N_{SQ}}$.

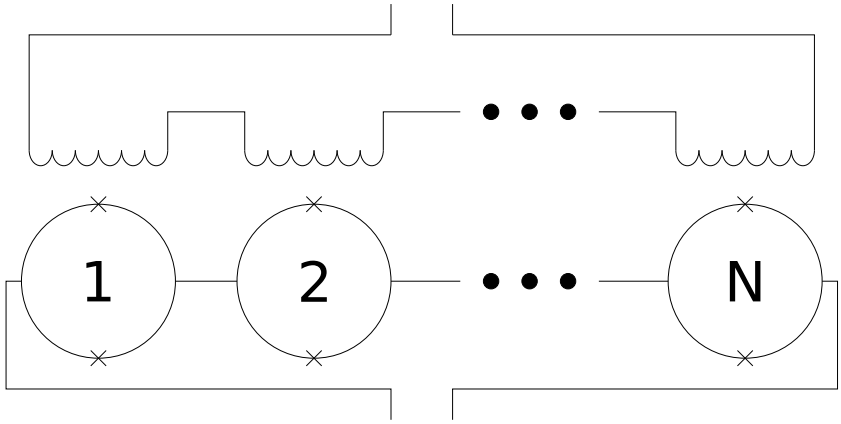

Figure 5–1: A N_{SQ}-element SQUID array referred to henceforth in this thesis as a "SQUID" formed by connecting N_{SQ} single-SQUID elements in series.

Difficulties in the SQUID operation can arise from the magnetic environment. A space dependent trapped magnetic flux in the superconducting single-SQUIDs generates a misalignment of their $V - \Phi$ curves and, consequently, a poor SQUID-array voltage response. The SQUIDs are therefore heated above their critical temperature and cooled before they are tuned to ensure no magnetic flux is trapped. EBEX uses

100-element SQUID-arrays. For the rest of this thesis, a SQUID-array is referred to as a "SQUID" unless specified.

5.2 Multiplexing

Readout multiplexing is achieved through the encoding of the signals from N detectors with N orthogonal functions and their decoding by room-temperature electronics, reducing the number of wires and the heat load on the sub-kelvin stage by a factor of N. Different encoding functions define the multiplexing techniques. This section describes the time-division, code-division and frequency domain multiplexing techniques currently developed to increase the pixel count of TES bolometer focal planes.

5.2.1 Time-Division Multiplexing

The time-division multiplexing (TDM) was first proposed and developed at NIST and is a mature multiplexing technology used by experiments such as SCUBA-2 [60], ACT [61], SPIDER [62], BICEP-2 and the Keck Array [63]. Figure 5–2 shows the schematic of a TDM $N \times M$ bolometer array composed of the assembly of M multiplexed module columns, each with N bolometers. The TES on a multiplexed module are sequentially sampled in time, so the data of any bolometer is recorded $\frac{1}{N}^{th}$ of the time. Every bolometer is individually coupled to a first stage single-SQUID trans-amplifier located on the sub-kelvin stage and used as a switch. The M bolometers on a single row are read out simultaneously. The rows are selected by biasing the first stage single-SQUIDs with low-duty boxcar current biases with a row-dependent phase, non-zero for $\frac{1}{N}^{th}$ of the time. The boxcar single-SQUID biases of the N rows are orthogonal. The outputs of all the first stage single-SQUIDs

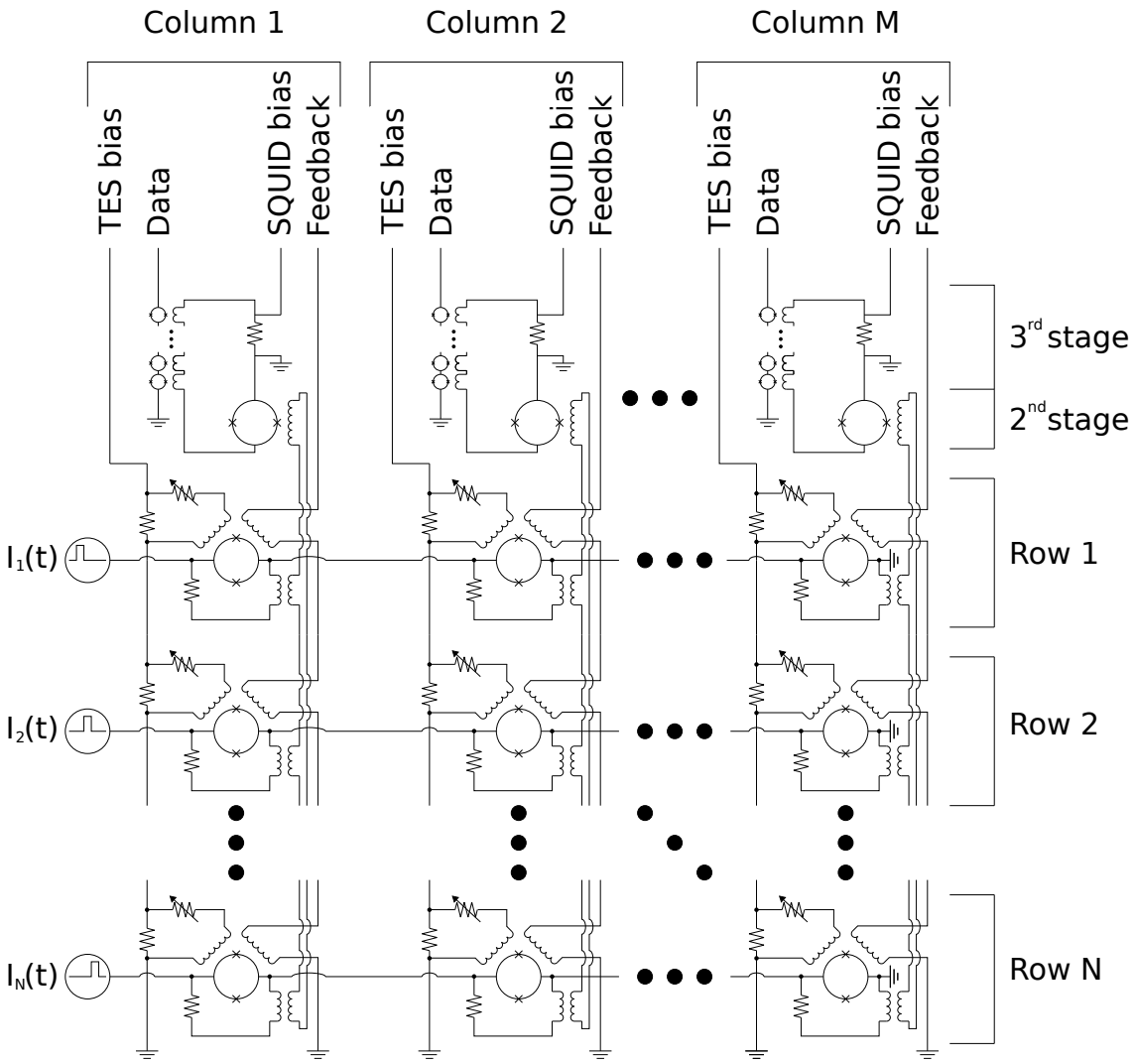

Figure 5–2: Schematic of a $N \times M$ TDM bolometer array. The TES are operated within a RL bandwidth limiting filter and are read by a single-SQUID biased with boxcar current functions. The rows are read simultaneously by a second stage single-SQUID and a third stage SQUID-array. The TDM multiplexed module is a column [59].

on a multiplexed module are coupled to a unique second stage single-SQUID and the signal is finally amplified a third time by a SQUID-array before reaching room

temperature electronics. TDM allows for the sharing of the wires providing the row selecting biases, the TES biases, the second stage single-SQUID biases, the first stage single-SQUID feedback and the TES signals. The total number of wires scales as 6×N×M for a non multiplexed system[1] and as 4M+N for a $N \times M$ TDM bolometer array.

In theory, the multiplexing factor of TDM is limited by the total bandwidth, the individual TES bandwidth, and the SQUID noise aliasing penalty. The total bandwidth is constrained to a few megahertz by the settling time of the row-selecting circuitry. To limit the individual bandwidth of the TES to a few kilohertz, the $\sim 10\ m\Omega$ TES are operated within a low-pass RL filter, where the filtering inductor is the SQUID input coil which typically has an inductance of hundreds of nanohenries. In the absence of this filter, the TDM would suffer from SQUID noise aliasing penalty since the TES are sampled only $\frac{1}{N}^{th}$ of the time. The noise above the Nyquist frequency of the bolometer sampling frequency would be aliased back into the baseband. The noise performance of the readout would therefore degrade as $\sqrt{N}$. A strong RL filter prevents this aliasing. However, bolometers operated within a RL filter with a cutoff frequency which is too low can become unstable, forcing the cutoff frequency to be increased above half of the bolometer sampling frequency. In this configuration, TDM suffers from SQUID noise aliasing penalty smaller than $\sqrt{N}$ and the value depends on the filtering parameters. A multiplexing factor of

[1] A non-multiplexed system of SQUID-coupled bolometer has three pairs of wires : one for bolometer bias, one for SQUID output and one for SQUID feedback.

40 is currently achieved with TDM and up to 32 multiplexed modules are read out simultaneously [60].

Since the TES and SQUID biases are shared within, respectively, a column and a row, TDM requires the SQUIDs and the bolometers to have uniform characteristics. The NIST fabrication process currently routinely achieves high yield arrays with uniform parameters. The sub-kelvin power dissipation is small ($\sim$ 10 nano-watts per multiplexed module), but non-zero. The sub-kelvin dissipation currently does not limit the multiplexing factor [59, 64].

5.2.2 Code-Division Multiplexing

The code-division multiplexing (CDM) is evolved from TDM and is also being developed at NIST. Due to its current on-going development, no cameras are currently operated with CDM. Walsh functions replace the TDM boxcar functions to encode the first-stage biasing currents and the TES signals are continuously sampled [65]. The TES are read out with either nominal or inverted polarity as a function of time and the multiplexing factor N is constrained to be a power of 2. The Walsh matrix for the simple case N=4 is

$$W = \begin{pmatrix} 1 & 1 & 1 & 1 \\ 1 & 1 & -1 & -1 \\ 1 & -1 & -1 & 1 \\ 1 & -1 & 1 & -1 \end{pmatrix} = 4W^{-1}, \tag{5.4}$$

where each row represents one of the N Walsh states and the different columns represent the M different multiplexing modules. The nominal polarity of the signal is read out for "+1" in the matrix and the inverted polarity, for "-1". The summed signals are decoded with the inverted Walsh matrix.

Figure 5–3 shows the schematic of a $N \times M$ CDM bolometer array with current steering.[2] Every bolometer is operated within a bandwidth limiting RL filter. A single-pole double-throw (SPDT) switch selects the polarity of the bolometer signal. The switch is composed of two parallel branches each with a single-SQUID and a coil in series. The two single-SQUIDs are operated with a $\frac{\Phi_0}{2}$ flux bias difference and the two coils have opposite polarity. One of the single-SQUIDs is operated with a $(n + \frac{1}{2})\Phi_0$ flux bias, where n is an integer. Its critical current is therefore small, as shown in Equation A.2, and the single-SQUID is driven normal by the bolometer signal. The TES signal is read through the other SPDT switch branch. The polarity of the signal is selected by applying a time dependent $\frac{\Phi_0}{2}$ flux bias simultaneously to both of the SQUIDs in the SPDT switch. The signals from the TES in a multiplexed module are summed and read out by a digitally fed back SQUID-array. As for TDM, the single-SQUIDs of the M TES bolometers on a single row share their biases.

The major advantage of CDM over TDM is the continuous sampling in time of all TES bolometers. It prevents the SQUID noise from aliasing into the baseband and therefore decreases the readout noise by up to $\sqrt{N}$ compared to TDM. Since CDM

[2] Other CDM configurations, such as CDM with flux summation, are not discussed in this thesis, but rely on the same basic principles [66]

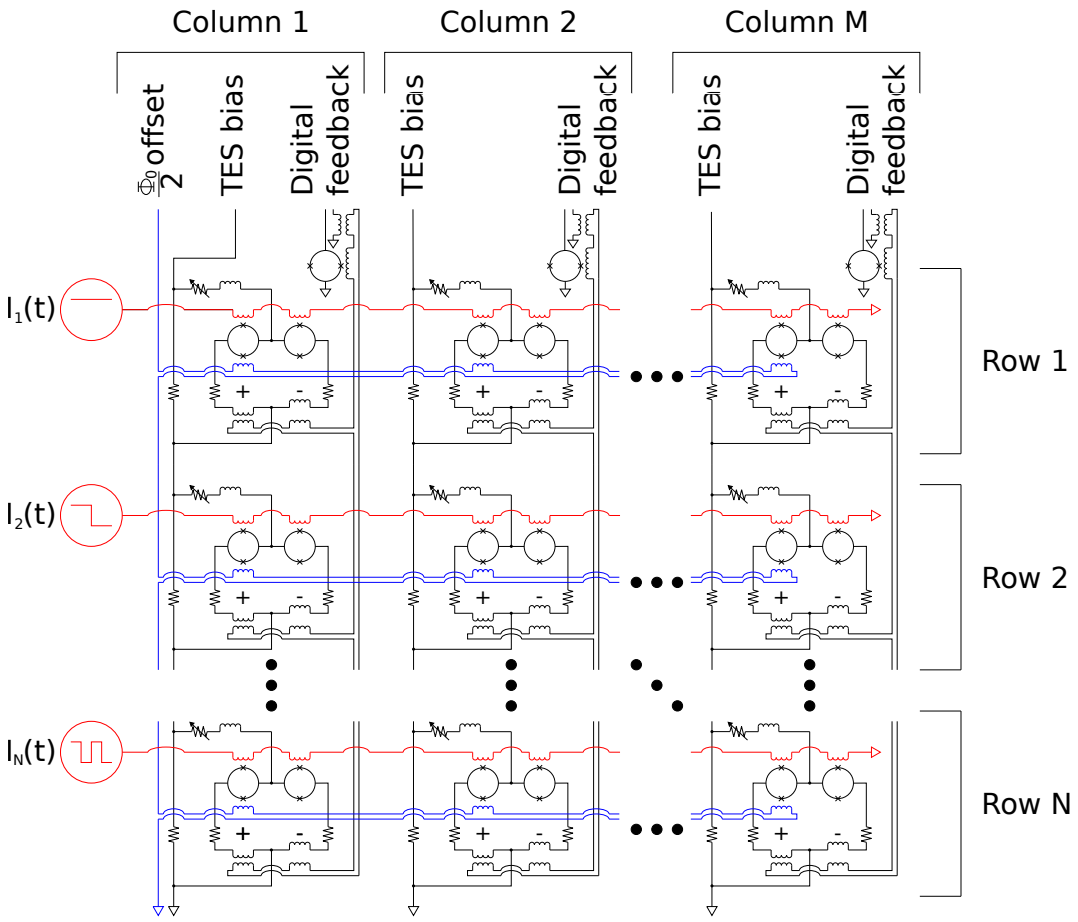

Figure 5–3: Schematic of a $N \times M$ CDM array. The TES are operated in a RL bandwidth limiting filter and are read by a polarity selecting SPDT switch composed of two single-SQUIDs with $\frac{\Phi_0}{2}$ flux bias offset and opposite polarity coils. The polarity is selected by applying a $\frac{\Phi_0}{2}$ flux bias to both single-SQUIDs and the single-SQUID with a half integer flux bias is driven normal by the bolometer signal [67].

is evolved from TDM, the other characteristics are the same for both techniques. A multiplexing factor of 4×1 is currently achieved with CDM [67].

5.2.3 Frequency-Division Multiplexing

The frequency domain multiplexing (FDM) was first proposed at University of California, Berkeley and was developed at University of California, Berkeley,

Lawrence Berkeley National Lab and McGill University [68]. FDM is a mature multiplexing technique exploited by experiments such as the APEX-SZ project [61], the SPT [69], EBEX [38], POLARBEAR [70] and the SPT-Pol [71]. Figure 5–4 shows the schematic of a multiplexed module of the FDM. The N TES bolometers on a multiplexed module are separated in the frequency domain and are continuously sampled. A voltage bias composed of N different carrier frequencies and amplitudes $\sum_{i=1}^{N} V_i(f_i)$ biases the N bolometers wired in parallel, each in series with a LC bandpass selecting filter. The TES resistances are amplitude modulated by radiation from the sky, encoding the signals in the carrier sidebands through negative electro-thermal feedback. A signal appears in the bolometer as a current inversely proportional to the incident optical power. The currents from the bolometers in a multiplexed module are summed at the input of a SQUID-array with a nulling comb of sinusoids 180° out of phase compared to the biasing signals. These nulling signals drastically reduce the dynamic range requirements of the SQUID-array by removing the carrier signals without affecting their sidebands. The electric biases are routinely nulled to 0.1%. The nulled signals are converted to voltage by a 4 K SQUID-array, amplified by room-temperature electronics and mixed with a demodulator signal $\sum_{i=1}^{N} V_i'(f_i)$. FDM decreases the number of wires reaching the sub-kelvin stage compared to a non multiplexed system from 2N to 2 per multiplexed module : one wire provides the voltage bias and one wire transmits the bolometer signal. The number of wires reaching the sub-kelvin stage for a camera multiplexed with M modules is therefore 2M.

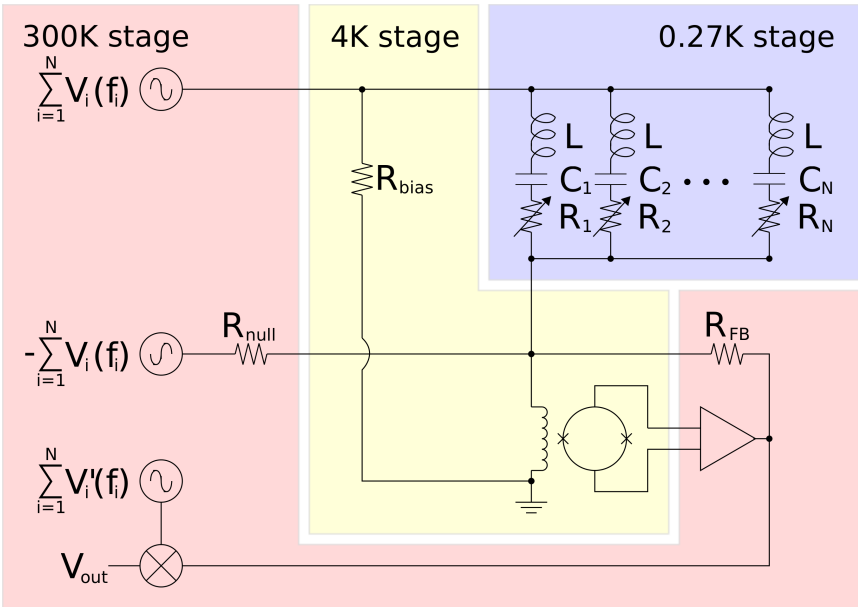

Figure 5–4: A sinusoid comb voltage biases bolometers. The bolometer bias frequency is selected by a RLC bandpass filter. The output signal is nulled by a 180° out of phase signal at the SQUID coil and then, demodulated. The room-temperature stage is shown in red, the 4 K stage is shown in yellow and the sub-kelvin stage is shown in blue [68].

The multiplexing factor for FDM has no theoretical limits. It is however limited, in practice, by the total bandwidth of the electronics and the electrical crosstalk between bolometers. The total bandwidth is currently limited to a few MHz by the phase shift from the wires connecting the SQUID-arrays to the room temperature electronics. A phase shift approaching 180° applied to the signal within the flux-locked loop (FLL) of the SQUID creates positive feedback and instabilities. The minimum wire length is constrained to be $\sim$ 20 cm by the cryostat physical size. The minimal bias frequency is set by the condition $f_{0\ min} \gg \frac{1}{2\pi\tau_{ETF}}$, so the TES bolometers do not respond to the time-dependent voltage bias. The physical size of

the filtering capacitors also constrains $f_{0\ min}$ since the bias frequencies are inversely proportional to their cross-section area and the physical space by the focal plane is limited. The minimum bias frequency is typically $\sim$ 200 kHz. The frequency spacing between the detectors is constrained by the voltage bias leakage from the neighbouring bolometers and is discussed in more details in Section 5.4.2. The bolometer bandpass is

$$\Delta f = \frac{R}{2\pi L}, \tag{5.5}$$

typically $\sim$ 10 kHz with 1 Ω TES bolometers and 16 μH bandpass inductors. The bandpass must respect the condition

$$\Delta f > \frac{5.8}{2\pi\tau_{etf}} \tag{5.6}$$

so the bolometers are operated in the critically damped regime and do not oscillate [72]. A multiplexing factor of 16 has been achieved with FDM.

The relevant stray components of the FDM cold system are shown in Figure 5–5. The inductive stray "p3" is due to the traces on the circuit board between the bias resistor and its four-point connection and needs to be accounted for with FDM when calculating the voltage bias of the TES bolometers at high frequencies. The bias resistor stray inductance is typically 4.0 nH and increases the effective bias

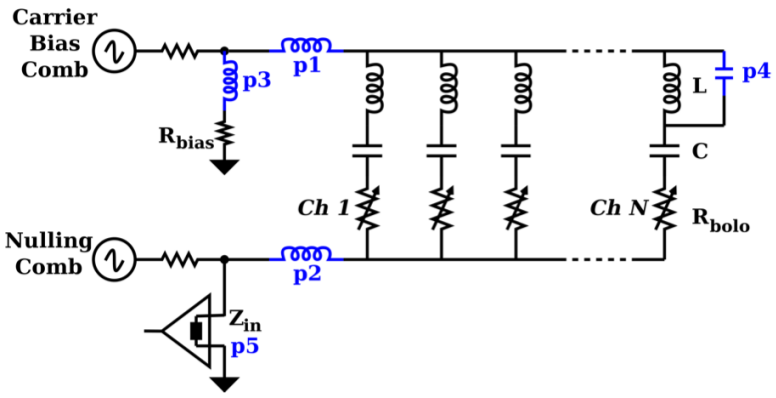

Figure 5–5: Stray components in the FDM curcuit. The wiring between the bias resistor and the multiplexed modules introduces the inductive strays p1 and p2. The inductive stray p3 is caused by the traces on the SQUID board in series with the bias resistor. A stray capacitance p4 is in parallel to the selecting RLC bandpass filters. The non-zero input impedance of the trans-amplifier is modelled by p5 [73].

impedance to R_{bias}+jωL_{stray}^{bias}. Therefore, the voltage bias increases by up to 42% at 1.2 MHz. The sub-kelvin wiring (p1 and p2) has a typical inductance of 100 nH and increases the impedance of the RLC bandpass limiting filters to R+jωL_{stray}^{wire}. The effects of these inductive strays can be reduced by adding a resonant capacitor that partially cancels the inductor effects. The voltage bias applied to the bolometer is reduced by up to 47%, for a 0.7 Ω bolometer, and up to 7%, for a 2.0 Ω bolometer, at 1.2 MHz, when such a capacitor is not included in the circuit. These strays are well understood and can be corrected for, as long as sufficient voltage bias is provided to the bolometers to maintain them in their superconducting transition. However, care has to be taken so they do not cause instabilities when the bolometer is dropped deep in its superconducting transition and its resistance becomes small.

The FDM electronics do not dissipate heat on the sub-kelvin stage since only passive components are located at the detector stage, allowing FDM to achieve theoretically higher multiplexing than TDM and CDM. The modulation of the TES signals by hundreds of kilohertz signals also decreases their pollution by low frequency noise sources, such as the mechanical vibrations of the telescope. The FDM benefits from high modularity to design focal planes and allows TES biases to be individually configured for every detector. FDM is therefore more robust against detector non-uniformity on a multiplexed module than systems that require the bias to be the same for all bolometers in a module, like TDM and CDM.

The main characteristics of the TDM, CDM and FDM are summarized in Table 5–1. EBEX uses FDM to read out its detectors.

Table 5–1: Characteristics of the TDM, CDM and FDM readout systems.

Property	TDM	CDM	FDM
Achieved multiplexing factor N	40	4	16
# of multiplexed wires	4M+N	4M+N	2M
# of multiplexed wires for a 1024 pixel camera*	160	160	128
Sub-kelvin power dissipation	(N+M) × 10 nW	(N+M) × 10 nW	0 W
Bandwidth per TES	∼5 kHz	∼5 kHz	∼ 5 kHz
Total bandwidth	∼1 MHz	∼1 MHz	∼1 MHz

* A multiplexing of 32×32 is assumed for TDM and CDM (though for CDM a factor of 4 has been achieved and published, we anticipate it can easily achive the same factor as TDM). A multiplexing factor of 16 is assumed for FDM.

5.3 The Digital Frequency Domain Multiplexed Readout System

The analog frequency domain multiplexing (fMUX) readout system was originally developed at University of California, Berkeley [68]. The analog fMUX system power consumption is $\sim 3\ kW$ [74] for a ~ 1000 bolometer focal plane. Since the total power budget for a balloon experiment is limited to $\sim 1\ kW$, a digital version of the analog fMUX (DfMUX) was developed at McGill University [75].

A DfMUX motherboard and its two mezzanine boards are shown in Figure 5–6. The sinusoidal voltage biases and the nulling currents for a single multiplexed module are digitally synthesized at 25 MHz by firmware algorithms implemented on a Xilinx Field-Programmable Gate Array (FPGA) located on the motherboard. The nulled bolometer signals are transmitted to the ambient temperature DfMUX electronics through 4 K SQUIDs operated in a flux-locked loop. The detector signals are lock-in demodulated by firmware algorithms on the FPGA. The mezzanine boards are populated with analog components amplifying the signals, the 16 bit digital-to-analog converters (DAC) and the 14 bit analog-to-digital converters (ADC). The signals are low-pass filtered on the analog side of the converters to avoid aliasing [54]. The mezzanine boards are customizable to fullfil the requirements of different cameras.

The demodulated bolometer signals are processed through a series of digital filters. A primary cascaded integrator-comb (CIC) filter decimates the 25 MHz signal to 195.3 kHz and a second CIC filter, to 12.21 kHz. Afterwards, finite impulse response (FIR) filters each decimate the signals by a factor of two. The output frequency is selectable. The unitary digital gain of the FIR filters allows to change the bandwidth without affecting the transfer function and represents a useful debugging

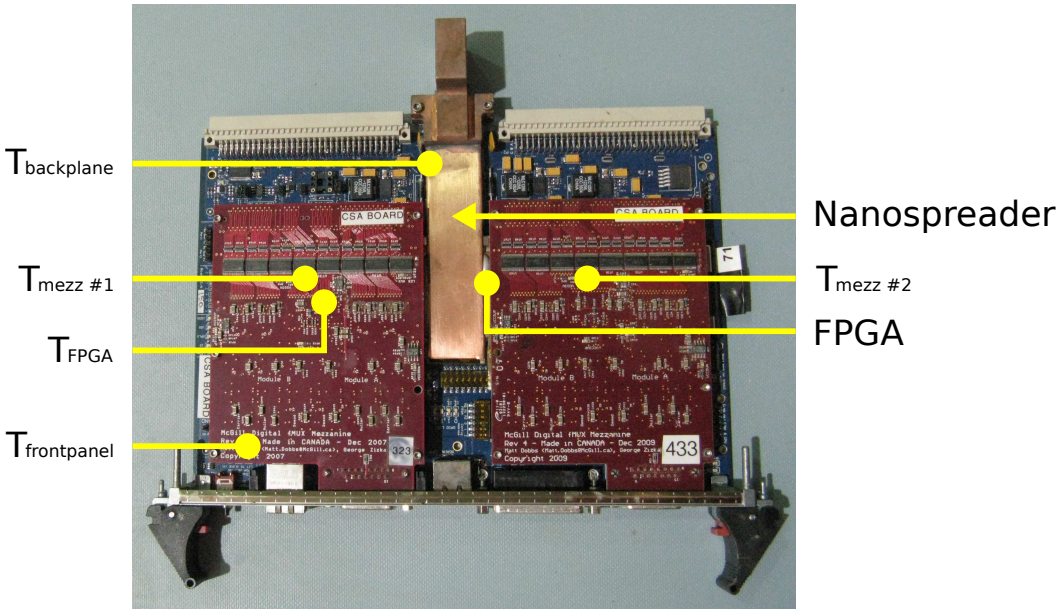

Figure 5–6: A DfMUX board. Two red mezzanine boards with the analog processing of the bolometer signals are attached on the blue motherboard. A 'NanoSpreader' heat-pipe, specific to EBEX readout electronic boards, is visible conducting the heat from the FPGA and ICs to the backplane of the readout crate. The location of the five temperature sensors are also shown.

feature. Table 5–2 shows the sampling frequency and the bandwidth of the signal as a function of the filtering stage. EBEX records data at 190.7 Hz.

The DfMUX is designed to operate in two distinct noise modes. The "camera tuning noise" mode allows a dynamic range of 29 μA for the un-nulled voltage biases during the bolometer biasing procedure. However, this mode suffers from high digitization and truncation noise. The "observing noise" mode was also implemented to allow the digitization noise to become negligible since less dynamic range is required when the sky is observed. The "observation noise" mode is selected by increasing the analog gain applied to the demodulated signal and, with the firmware that will be

Table 5–2: Sampling frequency and bandwidth of the different digital filter stages of the DfMUX.

Filter	Sampling frequency	3 dB analog bandwidth
CIC1	195.3 kHz	1.37 kHz
CIC2	12.21 kHz	1.37 kHz
FIR1	6104 Hz	1.37 kHz
FIR2	3052 Hz	1.22 kHz
FIR3	1526 Hz	610 Hz
FIR4	762.9 Hz	305 Hz
FIR5	381.5 Hz	153 Hz
FIR6	190.7 Hz	76 Hz

used for the LDB flight, by also increasing the digital gain applied to the streamed data by selecting the truncated bits. The LDB firmware allows more flexibility to select the gain and decreases the railing of the ADC converters.

The DfMUX readout system has been designed to optimize the setup time of the camera, therefore maximizing the camera observing time. On every DfMUX board, a software DfMUX algorithm manager (dalgman) program listens for requests sent over Ethernet in JavaScript Object Notation (JSON) protocol and executes algorithms on the camera. Examples of algorithm includes heating the SQUIDs above their critical temperature, selecting the SQUID operation parameters, electrically biasing the bolometers above and into their superconducting transition, increasing the analog demodulation gain, etc [76]. This architecture allows for the parallelization of the actions performed on the camera. For the NA flight, the dalgman on each motherboard could only execute algorithms sequentially. The time to perform a task on the camera with the DfMUX readout system is equivalent to the time to perform the same action on one DfMUX board worth of SQUIDs (a DfMUX board reads out

4 SQUIDs) or bolometers (a DfMUX board reads out 4N bolometers) and is independent of the number of DfMUX boards. The execution of up to four algorithms has been simultaneously implemented for the LDB flight, improving the processing time by a factor of four and the parallelization of the software to the multiplexed module level.

Due to the balloon-platform of EBEX, the DfMUX have to be operated in near-vacuum and so convective cooling is negligible at float. The DfMUX boards are cooled conductively by commercial 'NanoSpreader' heat pipes[3] , as shown in Figure 5–6, in thermal contact with the hottest components of the DfMUX motherboards and mechanically attached to the gondola so the heat is radiated away. Thermal compound conduct the heat from the FPGA and the ICs to the 'NanoSpreaders'. For the Antarctic long duration flight, for which there will be a higher power density to dissipate in the readout crates compared to the NA flight, a liquid coolant system has been implemented to improve the distribution of the heat over a larger surface area of the gondola. Also, the thermal compound has been replaced by custom-machined copper blocks that conduct heat from the ICs. Three sensors per motherboard and one sensor per mezzanine board, as shown in Figure 5–6, allow for the monitoring of the DfMUX board temperatures.

[3] 'NanoSpreader' is the brand name for commercially available heat pipes with sealed vapor chambers. The chambers contain pure liquid water forming a reservoir while vapor convectively conducts the heat. http://www.celsiatechnologies.com

5.4 Multiplexing Factor Development

During its engineering flight, EBEX operated the original multiplexed configuration of the DfMUX readout system of eight bolometers per multiplexed module. The bolometer normal resistances were $\sim 1\ \Omega$, the bandpass selecting inductors were 13, 16 or $22\mu H$, due to inductor availability, and the bolometers were biased at frequencies from 280 to 700 kHz with a 60 kHz spacing. For the LDB flight, the readout portion of the EBEX power budget permits 28 DfMUX boards to be operated, allowing a maximal number of 896 bolometers to be read out with the N=8 multiplexing configuration. EBEX will operate 1564 bolometers during its LDB flight. To increase the number of operable bolometers, the multiplexing factor has been increased from N=8 to N=16. To demonstrate the nominal performance of the readout system with the increased multiplexing factor, the stability of the SQUIDs and detectors is required to be shown since the electrical load at the SQUID coil is doubled and the highest voltage bias frequency is increased. Also, the crosstalk has to be shown to be negligible and the nominal noise performance of the bolometers has to be demonstrated so the expected sensitivity of the camera can be achieved.

5.4.1 Stability

To show the proper performance of bolometers operating when configured with N=16, the POLARBEAR bolometer wafer KT7, known to have nominal performance, was reconfigured and operated within a light-tight box. This wafer was chosen because no EBEX bolometer wafers had a sufficiently high yield of detectors when this development was initiated. Also, this wafer was easily reconfigurable and already had the proper bandpass selecting inductors. Four multiplexed modules were

Table 5–3: Bolometer bias frequencies per multiplexing module configured to have up to 8 and 16 bolometers for the POLARBEAR bolometer wafer KT7.

Multiplexed module		Bias frequency Hz
$KT7_{\times 15}$-1	$KT7_{\times 7}$-0	252603
		362466
		470222
		581957
		698373
		805662
		911780
	$KT7_{\times 8}$-1	306189
		416051
		525330
		642330
		749267
		853632
		961622
		1071485

Multiplexed module		Bias frequency Hz
$KT7_{\times 11}$-7	$KT7_{\times 4}$-6	316368
		375336
		497717
		1107288
	$KT7_{\times 7}$-7	442026
		556686
		676845
		793259
		915290
		1032174
		1155257

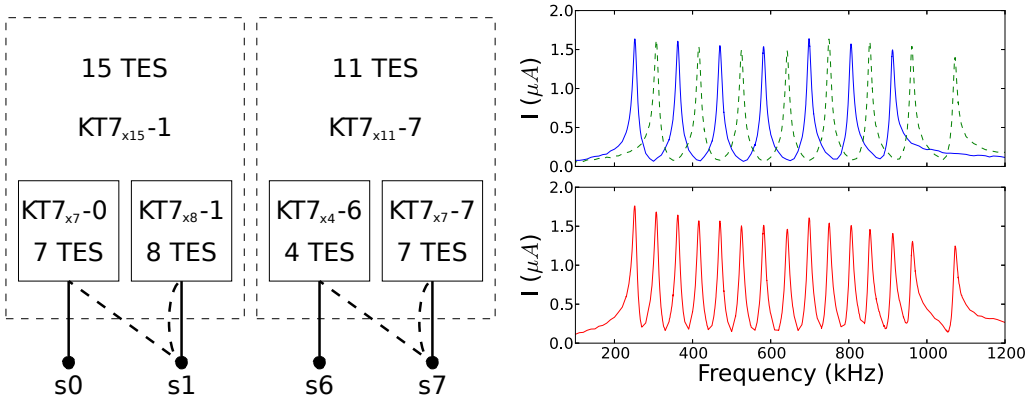

(a) (b)

Figure 5–7: Figure a) shows the multiplexing configuration of POLARBEAR wafer KT7. Two pairs of multiplexed modules each configured to have up to 8 bolometers (solid lines), $KT7_{\times 7}$-0 with $KT7_{\times 8}$-1 and $KT7_{\times 4}$-6 with $KT7_{\times 7}$-7, were wired in parallel to form the two multiplexed modules $KT7_{\times 15}$-1 and $KT7_{\times 11}$-7 configured to have up to 16 bolometers (dashed lines). The top panel of Figure b) shows the network analysis of the multiplexing modules $KT7_{\times 7}$-0 (solid) and $KT7_{\times 8}$-1 (dashed) and the bottom panel of Figure b) shows the network analysis of the multiplexed module $KT7_{\times 15}$-1.

configured to have up to eight bolometers with 22 μH filtering inductors : $KT7_{\times 7}$-0, $KT7_{\times 8}$-1, $KT7_{\times 4}$-6 and $KT7_{\times 7}$-7. The multiplexed modules are named $KT7_{\times N} - s$, where N is the number of bolometers on the module and s, the SQUID channel (from 0 to 7). The two multiplexed modules $KT7_{\times 7}$-0 and $KT7_{\times 8}$-1 were wired in parallel to be configured to have up to 16 bolometers and this modified module is $KT7_{\times 15}$-1. Similarly, the two multiplexed modules $KT7_{\times 4}$-6 and $KT7_{\times 7}$-7 were wired to form the multiplexed module $KT7_{\times 11}$-7. The bias frequencies, shown in Table 5–3, were set from 250 to 1075 kHz with a frequency spacing of 55 kHz. Figure 5–7 shows

the multiplexing configuration of the bolometer wafer KT7 and the network analysis for the multiplexed modules $KT7_{\times 7}$-0, $KT7_{\times 8}$-1 and $KT7_{\times 15}$-1 measured in two separate cryogenic runs.

The 15 TES bolometers of the multiplexed module $KT7_{\times 15}$-1 were first biased into their superconducting transition at 70% of their normal resistance. The SQUID showed nominal and stable DC level demonstrating the stability of the SQUID with the increased electrical current in the SQUID coil due to the multiplexed factor doubling. The increased effects of stray inductances degrade the voltage bias, but does not prevent the biasing of the bolometers in their superconducting transition.

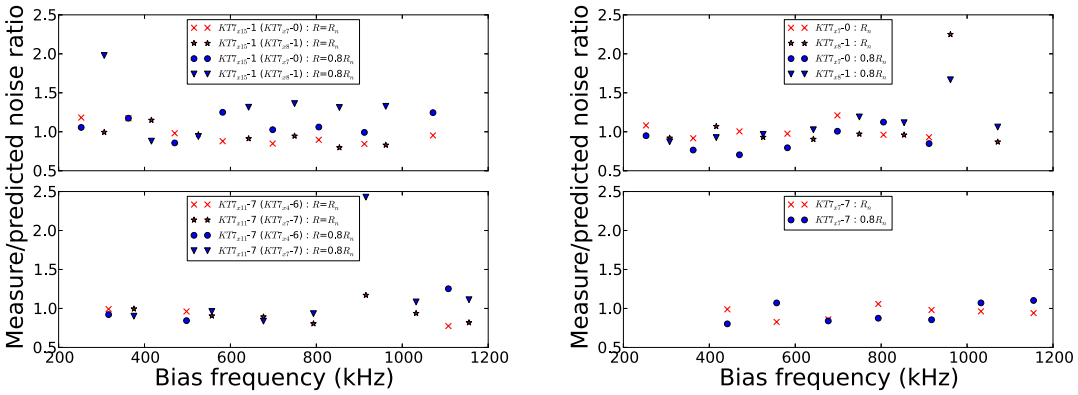

(a) (b)

Figure 5–8: Figure a) shows the measured-to-predicted noise ratio as a function of the bolometer bias frequency for the multiplexed modules $KT7_{\times 15}$-1 (upper panel) and $KT7_{\times 11}$-7 (lower panel) and Figure b), for the multiplexed modules $KT7_{\times 7}$-0 and $KT7_{\times 8}$-1 (upper panel) and $KT7_{\times 7}$-7 (lower panel). Each panel shows the measurement performed with detectors biased above their superconducting transition and at 80% of their normal resistance in their superconducting transition.

The noise performance of the bolometers was then compared to the N=8 multiplexing configuration. Figure 5–8 shows the measured-to-predicted noise ratios of

the bolometers biased above their superconducting transition and at 80% of their normal resistance in their superconducting transition for both multiplexing configurations. The multiplexing module $KT7_{\times 4}{-}6$ was not studied due to a wiring issue. Figure 5–9 shows the measure to predicted noise ratio distributions for those measurements. The noise distributions show nominal performance for the bolometers biased above their superconducting transition for both multiplexing configurations : the measured-to-predicted noise ratio is 0.9 ± 0.1 and 1.0 ± 0.1 for the multiplexed modules configured to have up to 8 and 16 bolometers, respectively, not considering the outlying detector with a measured-to-predicted noise ratio of 2.2. When biased in their superconducting transition, the bolometers show a measured-to-predicted noise ratio of 1.1 ± 0.2 and 1.0 ± 0.1 for the multiplexed modules configured to have up to 8 and 16 bolometers, respectively, not considering the three outlying detector with a noise ratio greater than 1.5.

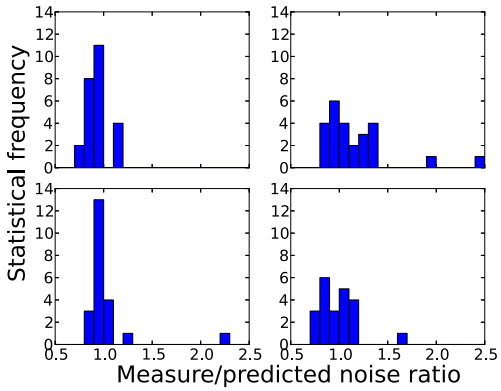

Figure 5–9: Distributions of the measured-to-predicted noise ratio for the multiplexed modules configured to have up to 16 bolometers (upper row) and 8 bolometers (lower row) with bolometers biased above their superconducting transition (left column) and at 80% of their normal resistance in their superconducting transition (right column).

The outlying detector present on a multiplexed module configured to have up to 8 bolometers shows degraded noise performance when biased above and into its superconducting transition. The same detector shows nominal noise performance when previously operated within a multiplexed module configured to have up to 16 bolometers. Also, the first cooling of this wafer after its initial reconfiguration to form the multiplexed modules $KT7_{\times 15}$-1 and $KT7_{\times 11}$-7 was aborted. A total of two bolometers had to be un-wired since they polluted the noise performance of all bolometers. This was caused by damaged wire-bonds. These facts suggest the instability is not caused by the multiplexing configuration, but by wire-bond alterations during the multiplexing re-configuration.

The two outlying bolometers present on a multiplexed module configured to have up to 16 bolometers show nominal noise performance when biased above their superconducting transition, but their noise performance greatly decreases as they are dropped into their superconducting transition only when present on a multiplexed module configured to have up to 16 bolometers. They consequently show instabilities which are not observed subsequently when operated on multiplexed modules configured to have only up to 8 bolometers. The bolometer parameters of all KT7 bolometers, including those two bolometers, are uniform and the instability of those two bolometers is unexplained. Moreover, EBEX is now using a similar configuration with up to 16 bolometers per multiplexed module and nominal noise performance is achieved across many dozen combs. These instabilities are therefore exceptional and assumed to be caused by the properties of these specific detectors or damaged wiring. Given the history of damaged wire-bonds and bolometers in handling this

bolometer wafer, the instability of these two bolometers has not been shown to be caused by the multiplexing factor increase.

Finally, no frequency dependence is observed in the noise performance of the detectors demonstrating that the stray inductances do not prevent the operation of bolometers with bias frequencies up to 1.2 MHz. The bolometers therefore show nominal noise performance when operated within multiplexed module configured to have up to 16 bolometers.

5.4.2 Crosstalk

Crosstalk is defined to be the signal caused by the i^{th} bolometer onto the neighbouring k^{th} bolometer on the multiplexed module. Multiplexing introduces three sources of electrical crosstalk. The electrical crosstalk is required to be smaller than the optical crosstalk, which is typically 1%. The first source of electrical crosstalk is the magnetic cross-coupling of the bandpass selecting inductors. The amplitude modulation of the resistance of the i^{th} bolometer on a multiplexed module with a biasing frequency f_{0_i} and a bandpass selecting inductor L_i induces a voltage $|V_k| = 2\pi f_i M_{ik} I_i$ on the k^{th} bandpass selecting inductor, where $M_{ik} = \alpha_{ik}\sqrt{L_i L_k}$ is the mutual inductance between inductors. The induced current through the k^{th} bolometer $I_k = |V_k|/Z_k(f_{0_i})$ is small and can be made negligible by ensuring physically neighbouring inductors have large frequency bias spacing and hence, minimizing α_{ik}.

The second source of electrical crosstalk is due to leaking biases in the neighbouring bolometers. The i^{th} bolometer on a multiplexed module has a frequency dependent impedance given by Equation 4.25. The fraction $\frac{Z_i(f_{0_i})}{Z_i(f_{0_j})}$ of the current

going through the i^{th} bolometer leaks into the j^{th} bolometer on the multiplexing module. The amplitude modulation of the bolometer resistance R_i generates current variations modulating the resistance from the other bolometers. The produced crosstalk is approximated by

$$X_{ik}^{leak} \simeq \left(\frac{R_i}{2\Delta\omega L}\right)^2 \tag{5.7}$$

when $R_i \ll 2L\Delta\omega$ [73].

The third source of electrical crosstalk is the non-zero SQUID and the wiring stray impedances. The modulation of the resistance of the i^{th} bolometer modulates the voltage bias at frequency ω_i across the stray wiring inductances p1 and p2 and the SQUID stray impedance p5. In turn, the leakage current through the k^{th} is also modulated. The magnitude of this source of crosstalk is

$$X_{ik}^{stray} = -\frac{I_k(f_i)}{I_i(f_i)}\frac{j4\pi f_i L_{stray}}{Z_k(f_i)} \simeq -j4\pi L_{stray}\frac{Z_i(f_i)}{Z_k^2(f_i)}, \tag{5.8}$$

where L_{stray} is the effective stray inductance of the wiring and of the SQUID input impedance and is typically $\sim$ 100 nH, assuming the bias voltage is uniform for the bolometers in the multiplexed module [73].

To measure crosstalk, a voltage bias of 0.14 μV was applied at a frequency of 375342 Hz to the multiplexing module $KT7_{\times 11}$-7, amplitude modulating at 6 Hz

the resistance of the bolometer biased at 375336 Hz. A 6 Hz current response was measured in all bolometers and Figure 5–10 shows the normalized bolometer response as a function of the bolometer bias frequency spacing. The same measurement was repeated at a frequency of 442035 Hz, amplitude modulating at 9 Hz the resistance of the bolometer biased at 442026 Hz.

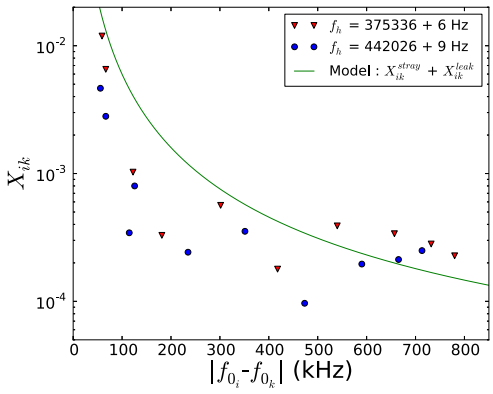

Figure 5–10: Crosstalk measurements as a function of the bolometer frequency spacing measured on the multiplexed module formed by the wiring of $KT7_{\times 4}$-6 and $KT7_{\times 7}$-7 in parallel. The 6 Hz response of the bolometers when a voltage bias of 0.14 μV is applied at 375342 Hz and the 9 Hz response when the same voltage bias is applied at 442035 Hz is measured. The crosstalk expectation from leakage currents and from wiring and SQUID input stray impedances is also shown.

The crosstalk is smaller than the predictions for frequency spacings smaller than 500 kHz. At higher frequency spacing, the measured crosstalk becomes independent of frequency spacing. The crosstalk model does not include the inductor cross-coupling and the crosstalk of the wires. The excess crosstalk at high frequency spacing is negligible. The multiplexed modules configured to have up to 16 bolometers are found to meet the requirement for the crosstalk to be smaller than the $\sim 1\%$ expected optical crosstalk.

The stability of the SQUIDs and bolometers for multiplexed modules configured to have up to 16 bolometers has been demonstrated and the crosstalk has been shown to be within specifications. Following these measurements, the increased multiplexing factor is implemented in EBEX. The bias frequencies of the detectors will be set between 200 and 1160 kHz with 24 μH bandpass selecting inductors.

5.5 Summary

The FDM multiplexing technique has been chosen for the EBEX receiver and the DfMUX readout system been developed for EBEX. The multiplexed modules were configured to have up to 8 bolometers for the EBEX engineering flight. The multiplexing factor of the DfMUX system has been increased from 8 to 16 and has been shown to allow for the stable operation of bolometers with nominal noise performance. The electrical crosstalk within a multiplexed module has been shown to be lower than the required level of 1%. EBEX will operate multiplexed modules configured to have up to 16 bolometers for its LDB flight.

CHAPTER 6
Results from the EBEX Engineering Flight

During its science flight, EBEX will circumnavigate Antarctica for 11 days. Balloon platform telescopes allow for the observation of the sky while avoiding most of the atmosphere, greatly increasing the data quality compared to ground-based telescopes. However, Antarctic flights are costly and the risk of a technical malfunction degrading the quality of the science results derived from the data is high compared to ground-based experiments. Consequently, NASA requires a proof of concept of the technology that will be used at float before the LDB flight is approved. To fulfill this constraint, EBEX performed an engineering flight in June 2009 to achieve the following goals :

- to demonstrate the first operation of a SQUID-based frequency multiplexed readout system and of TES bolometers in a space-like environment;
- to characterize the noise performance of the bolometers at float;
- to verify the proper daytime operation of the different EBEX subsystems at float;
- to verify the electronic boards do not overheat in a near vacuum environment during daytime;
- to calibrate the bolometer response to on sky sources;
- to measure the optical loading at float;
- to test the remote operation of the bolometer and ACS systems;

- to assess the ability of the ACS to point the receiver.

EBEX was launched for its engineering flight on June 11^{th} 2009 from Fort Sumner, New Mexico, and landed near the western border of Arizona. Figure 6–1 shows the trajectory and altitude of the payload during the flight. The EBEX flight lasted over 13 and a half hours, 10 of those at float at an average altitude of 34 km, fulfilling requirements contracted by CSBF. This chapter first presents a general summary of the NA flight. The performance of the readout system, its power consumption, the setup and the stability of the camera, the noise performance of the camera and the optical loading as a function of altitude are then discussed.

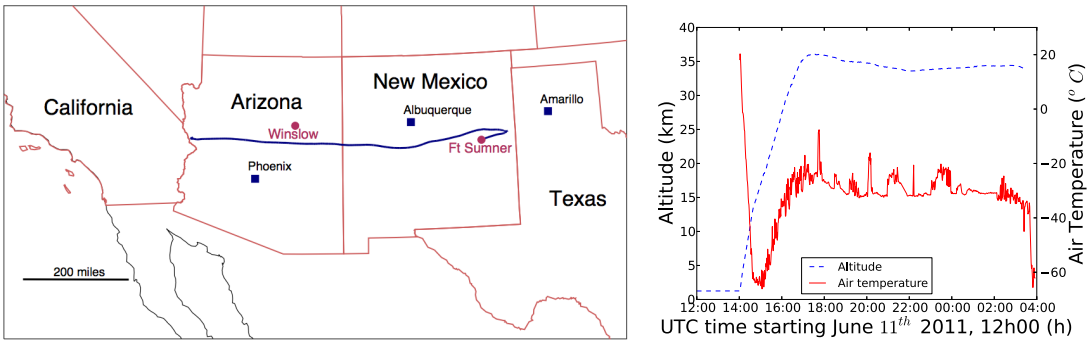

(a) (b)

Figure 6–1: Figure a) and b) show, respectively, the trajectory and altitude (blue dashed line) of the payload during the EBEX engineering flight. EBEX was launched at 14h02 UTC on June 11^{th} 2011 and the flight was terminated at approximately 3h29 UTC on June 12^{th}. Figure b) also shows the air temperature (red solid line) during the same flight. The ambient air temperature cools with altitude until the payload reaches the tropopause and warms ups with altitude once the tropopause is passed.

6.1 Summary of the EBEX NA Flight

Table 6–1 presents chronologically the events relevant to this thesis that occurred during the NA flight. EBEX was launched at 14h02 UTC on June 11^{th} 2009.

Table 6–1: Chronology of event during the NA flight relevant to this thesis.

Day UTC	Time UTC	Duration	Event
June 11^{th}	8h09	4h53	EBEX is on the launch pad.
	14h02	—	EBEX is launched.
	14h02	—	The elevation actuator breaks.
	15h08	1h14	The optical loading is measured as a function of altitude.
	16h20	—	The SQUIDs trapped magnetic flux.
	17h25	11 min	The SQUIDs are diagnosed.
	17h34	—	The payload reaches its maximal altitude of 36 km.
	17h35	6 min	The SQUIDs are heated.
	17h52	9 min	The SQUIDs are tuned.
	17h59	4 min	The bolometers are electrically biased above their superconducting transition.
	18h49	51 min	The bolometers are dropped in their superconducting transition.
	19h33	26 min	A calibration scan on Saturn is performed.
	20h13	11 min	The camera is set in "observing noise" mode.
	20h21	5h44	ACS test scans are performed.
	22h13	3h44	Bolometer noise is measured as a function of deepness in transition.
June 12^{th}	2h53	24 min	A CMB dipole scan is performed.
	3h29	—	Last log entry is logged by the flight computer.

At launch, SQUIDs were tuned and detectors were electrically biased above their superconducting transitions while the detector stage temperature had stabilized at 280 mK, below the bolometer critical temperature. Figure 6–2 shows the temperature of the three bolometer wafers during the NA flight. The torque applied to the inner frame at launch caused the elevation actuator to bend preventing relative movements between the "inner" and "outer" frames and constrained the elevation of the telescope to 15° for the remainder of the flight [36]. This failure forced a complete rethinking of the observing strategy during flight since only constant elevation telescope scans could be performed. Heating from vibrations also caused the temperature of the wafers to rise to 500 mK. Once the payload reached an altitude of 18 km, at 15h08 UTC, the optical loading as a function of altitude was measured. One detector per frequency band was dropped into its superconducting transition at 70% of its normal resistance and, right afterwards, biased above its superconducting transition. This procedure was repeated at many altitudes as the payload was ascending. The bolometer wafer temperature was still cooling at this time. Results are discussed in Section 6.7. This measurement was interrupted at 16h22 UTC, as the payload reached 31 km, due to the realization that all SQUIDs were showing an unrecoverable non-zero noise DC level, meaning the SQUID stopped amplifying nominally. This behaviour was debugged remotely for 11 minutes. This event is discussed in detail in Section 6.4 and forced a complete re-tuning of the camera from 17h35 to 20h24 UTC. The camera tuning involved thermally cycling the SQUIDs above their critical temperature to remove any trapped magnetic flux, tuning the SQUIDs to their optimal operating point and electrically biasing the bolometers

above their superconducting transition while the TES were thermally maintained above their critical temperature, dropping the bolometers in their superconducting transition and setting the camera in "observing noise" mode.

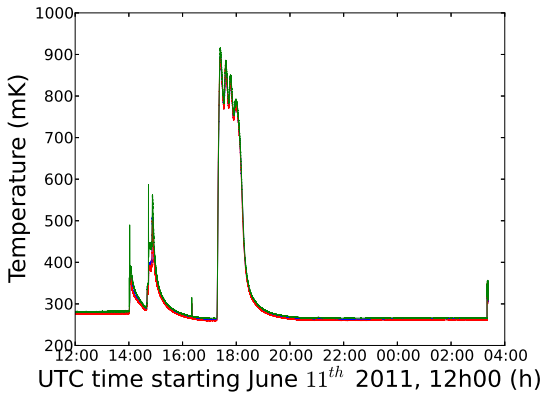

Figure 6–2: Temperature of the bolometer wafers during the EBEX engineering flight. The blue, red and green curves show respectively the temperatures of wafers 150-G17, 250-G20 and 410-G18.

The failure of the elevation actuator constrained the time period when calibration scans could be performed on Saturn. Only one such scan could be attempted during the NA flight given the elevation of the telescope could not be modified. The forced complete re-tuning of the camera prevented the camera from being setup nominally before the time Saturn crossed 15° elevation. In order to attempt to observe Saturn, the re-tuning of the camera was performed minimizing the setup time instead of maximizing the stability of the camera. Consequently, the bolometers were biased at 70% of their normal resistance at 17h59 UTC, while the wafer temperatures were 290 mK and still cooling towards 270 mK : the equilibrated wafer temperature at float. The Saturn calibration scan was performed from 19h33 to 19h59 UTC while the last bolometers were still being dropped in their superconducting transition and the

wafer temperature had not stabilized [36]. The camera was set in "observing noise" mode at 20h13 UTC, after the Saturn scan was finished due to time constraints, and completed by 20h24 UTC.

To access the capacity of the ACS to point the telescope, various scans were performed from 20h21 UTC until 2h05 UTC on June 12^{th} [36]. Meanwhile, bolometer noise as a function of the deepness of the bolometers in their superconducting transition was measured for a subset of the bolometers from 22h13 UTC, June 11^{th}, to 1h57 UTC, June 12^{th}, ending with those bolometers being superconducting. This measurement is discussed in Section 6.6.5. From 2h53 to 3h17 UTC on June 12^{th}, the dipole of the CMB was observed [77]. The last entry in the flight computer happened at 3h29 UTC, just before the flight was finally terminated, to avoid overflying California : state laws prevent scientific payloads from flying over California.

The elevation drive failure and the complete re-tuning of the camera were not expected during the NA flight. However, one of the goals of the engineering flight was to reveal the failure modes of the payload to avoid catastrophic failures during the science flights. Those events unfortunately prevented Saturn from being detected, but improved the robustness of the EBEX payload for its LDB flight.

6.2 The Readout Electronics Performance

The thermal aspect of building electronics for a balloon flight is non-trivial because of the uncommon ambient environment. The payload flies in a near-vacuum environment and sees the Sun for extended periods of time. The cooling of the electronics through air conduction is negligible. The power generated by the electronics

has to be conducted to the gondola from where it is radiated, as discussed in Section 5.3. Even if the air temperature is well below the freezing point at float, as shown in Figure 6–1 b), the challenge is to prevent the electronics from overheating. The LDB flight represents as well a worst case thermally compared to the NA flight because it will be in diurnal conditions 24 hours per day.

The electronic chip with the lowest temperature rating on the DfMUX boards is the Ethernet PHY chip with a rating of $70°C$. The FPGA is rated to $100°C$ and is the warmest component on the board. A temperature sensor is located 6 cm from the center of the FPGA and measures a temperature lower than the actual FPGA temperature. For those reasons, the temperature of the DfMUX is aimed to be kept below $65°C$, providing a $5°C$ margin. The DfMUX boards are routinely operated at a temperature approaching $65°C$ in the lab.

The temperatures and the voltages (shown in Appendix C) of the DfMUX were recorded at two minute intervals during the engineering flight. Figure 6–3 shows the temperature of the five different temperature sensors located on DfMUX boards 038 and 040, the coolest and the warmest boards during the NA flight. All boards show the same temperature profile at float. The position of the temperature sensors are shown in Figure 5–6. Table 6–2 shows the maximal temperature reached by every DfMUX board during the NA flight.

On the launch pad, the 12 DfMUX boards housed in two separate radio frequency interference (RFI) free BROs are cooled through air convection driven by the in-crate fans. The air exchange between the inside and outside of the crates is small due to the design of the BROs. The board temperatures decrease as the payload

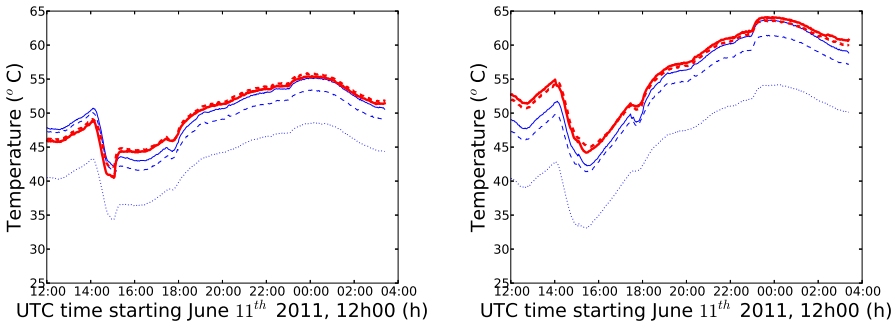

(a) (b)

Figure 6–3: Figure a) and b) show, respectively, the temperature of DfMUX boards 038 and 040, the coolest and warmest boards during the EBEX engineering flight. The solid, dashed and dotted blue lines show the temperature of the DfMUX board near the backplane, the FPGA and the frontpanel. The solid and dashed red lines show the temperature of the mezzanines #1 and #2.

cools with the ambient air at night. As the Sun rises (11h45 UTC, June 11^{th}), the temperature of the in-crate air as well as the gondola, to which the BRO crates are heat-sunk, rises. Consequently, the DfMUX boards temperature increases. As the payload ascends, the temperature of the DfMUX boards decreases drastically due to

Table 6–2: Maximal temperature measured during the NA flight per DfMUX board.

BRO1	
DfMUX ID	T_{max} ($^\circ C$)
011	59.5
012	60.9
013	59.5
022	60.6
023	61.5
038	55.9

BRO2	
DfMUX ID	T_{max} ($^\circ C$)
035	58.3
036	59.3
037	59.8
039	63.4
040	64.1
041	58.8

the rapid cooling of the ambient air and gondola temperatures, as shown in Figure 6–1 b). The in-crate fans were turned off at 15h05 UTC to avoid a malfunction due to the decreasing air density. The convective cooling was designed for ground operation of the DfMUX boards. Convection cooling subsequently becomes negligible and conduction through the gondola becomes the dominant cooling mechanism in this near-vacuum environment. From that time, the temperature of the boards rises continuously until 0h00 UTC, June 12^{th}, close to the sunset time of $\sim$2h00 UTC, June 12^{th}. Exceptionally, the DfMUX boards cool for a brief period of time when they were not furnishing any biases due to the complete retuning of the camera at 17h25 UTC on June 11^{th}. The board temperatures decrease as the Sun sets after 0h00 UTC on June 12^{th}.

Even though none of the boards exceeded the set temperature limit of $65°C$ during the NA flight, the temperature did not equilibrate during the day-time operation of the boards. This data show risks of the electronics reaching $70°C$ for the LDB flight that will be in diurnal conditions 24 hours per day. After the flight, the quantity of thermal compound applied to conduct the heat from the integrated circuits (IC) and the FPGA to the RFI shields on the DfMUX, where the DfMUX are heat-sunk to the gondola, was found to be not insufficient on the components of some DfMUX boards, explaining the variability of the temperatures from board to board. This step of the heat-sinking of the boards has been carefully re-done for the FPGA and the thermal compound has been replaced by copper heat-sinking before the LDB flight. Moreover, the two additional BRO crates for the LDB flight have 33% more DfMUX boards housing capacity and require additional cooling. A

thermal link circulating liquid to increase the heat flow from the BRO crates to a panel which will ultimately radiate the power to the sky has been designed and is being implemented. The dedicated radiating panel was not implemented for the NA flight.

6.3 Power Consumption

Ballooning highly constrains the power budget available at float. A limited number of batteries and solar panels can be flown due to the lifting capacity of the balloon and the limited solar panel area available on the payload. The DfMUX boards are an evolution from the analog fMUX readout system developed to lower its power consumption. The DfMUX boards are powered by $\pm 6\ V$ and $\pm 10\ V$ voltages.

The main power consumption (46%) comes from the +6 V for the basic functionalities of the board : powering the FPGA, the ICs, etc. The $\pm 6\ V$ each consumes most of the remaining power to enable the analog amplification chain of the carrier, nuller and demodulator signal with 19% of the total consumption each, a fraction which increases as biases are produced. The $\pm 10\ V$ power consumption is negligible and produces the SQUID biases. Table 6–3 shows the power consumption per DfMUX board measured after the NA flight with current limited power supplies. The power consumption is shown for the four voltage sources and at different steps during the camera tuning. The number of boards used for the different measurements is limited by the 16 SQUIDs and the single bolometer wafer operable in the testing cryostat.

The measurement with bolometers biased above their superconducting transition represents an upper limit of power consumption for a given bolometer wafer

Table 6–3: Measured power consumption per DfMUX board for the NA flight.

Configuration	# of DfMUX averaged	P_{+6V} W	P_{-6V} W	P_{+10V} W	P_{-10V} W	P_{Total} W
DfMUX boards on	6	8.6	0.0	0.0	0.0	8.6
DfMUX and mezzanine boards on	6	12.5	3.1	0.00	0.00	15.6
DfMUX, mezzanine and SQUID controller boards on	6	13.1	3.5	0.03	0.07	16.7
SQUIDs tuned	4	13.7	3.8	0.05	0.05	17.6
SQUIDs tuned	2	12.8	3.8	0.05	0.05	16.7
Bolometers biased above their superconducting transition	2	14.4	4.0	0.05	0.05	18.5

since all the components of the readout chain are used and the bolometer biases are maximal. The DfMUX are therefore measured to consume, on average, 18.5 W. However, this measurement shows limitations. The power consumption is only consistent to 5% when the SQUIDs operated by two and four DfMUX boards are tuned. Also, the +6 V power consumption goes down when the SQUIDs are tuned with two DfMUX boards with respect to when the SQUIDs are not tuned. This is due to the DfMUX power draw variability. The power consumption is also dependent on the SQUID and bolometer biases : the number of biasing channels and their amplitude. This therefore points to the requirement for the power consumption to be measured in the EBEX cryostat with detector wafers meeting the LDB flight detector yield targets and specifications. A power margin is also required.

Table 6–4 shows the comparison between the test measurement and a measurement performed with six DfMUX boards and with detectors biased above their superconducting transition in the EBEX cryostat, both with the DfMUX firmware used during the NA flight. Table 6–4 also shows the latter measurement performed in the EBEX cryostat with 28 DfMUX boards and with the firmware that will be used for the LDB flight. Results are shown for the following configurations : one DfMUX board, two DfMUX boards, one BRO crate of six DfMUX boards, the NA flight configuration and the LDB flight configuration. The power consumption for the measured configurations are extrapolated to the other configurations by scaling by the number of DfMUX boards.

Table 6–4: Measured and extrapolated power consumption of the readout system for the NA and LDB flight with detectors biased above their superconducting transition.

Configuration Firmware	# of DfMUX	Test setup NA W	EBEX setup NA W	EBEX setup LDB W
One DfMUX board	1	18.5 †	20.4 †	21.2 †
Two DfMUX boards	2	37.0 *	40.7 †	42.4 †
One BRO crate	6	111.0 †	122.2 *	127.2 †
NA flight	12	222.0 †	244.4 †	254.4 †
LDB flight	28	518.0 †	570.2 †	593.6 *

* Measured value.
† Extrapolated value.

The measurement performed with the NA flight firmware in EBEX is 10% higher than the test measurement. A similar board-to-board variation is measured when comparing the two configurations in the test setup with SQUIDs tuned. The power consumption of 18.5 W per DfMUX board is expected to be lower than average

for the four DfMUX boards used. The power consumption measurement performed with the EBEX setup is more reliable because of the higher number of DfMUX boards used. The power consumption presented in this section is from the readout system only. The 28 V power consumption delivered by the batteries to the DC to DC converters, providing the power to the BRO crates, is higher due to the 82% inefficiency of the DC to DC converters. The power delivered by the batteries to the readout system was therefore 298 W for the NA flight. For the LDB flight, this number is 724 W. Even though the power consumption per DfMUX board has been optimized, it slightly increased between the NA and the LDB flight due to added functionalities in firmware. The readout power consumption meets the EBEX power budget constraints.

6.4 The Camera Setup at Float

For the NA flight, EBEX was launched with its SQUIDs tuned and its detectors electrically biased above their superconducting transition, planning to drop the detectors in their superconducting transition at float. This strategy was selected to maximize the observing time at float. Commands to perform actions on the camera were uploaded individually by the commanding crew. The availability of line of sight communication for the entire flight ensured adequate realtime feedback on the ground : all result files from the camera setup, all recorded voltage and temperature values and a third of the bolometer timestream data were reliably downlinked to the command center in realtime. Commands were initially sent to the payload from the Fort Sumner command center and, for the last four hours and a half of the flight, from the command center located in Winslow, Arizona.

At 16h20 UTC, on June 11^{th}, the SQUID noise DC level had become non-zero and was unfixable on all SQUIDs. The wafer temperature also rose by 35 mK at the same time and cooled rapidly afterwards, as shown in Figure 6–2. The SQUIDs were therefore diagnosed by performing the standard SQUID tuning algorithm on a subset of SQUIDs. The peak-to-peak voltage response of SQUID B15 as a function of the applied current bias ($V^{PP} - I_b$ curve) was first measured, as shown in Figure 6–4 a). This figure also shows the nominal tuning curve performed on this SQUID on the ground 16 hours before launch. The maximal voltage response of SQUID B15 was 4.00 V^{PP} before launch and only 0.76 V^{PP} at float after the non-zero DC level appeared. The voltage response of the SQUIDs as a function of the flux bias ($V - \Phi$ curve) at the tuned current bias, as shown in Figure 6–4 b), was then measured. The close to sinusoidal nominal response measured on the ground is very different from the low amplitude and irregular response measured at float. This behaviour is characteristics of the 100 elements of a SQUID array, referred as a single SQUID, possessing a space dependent trapped magnetic flux creating destructive interference in the SQUID response and degrading it.

Consequently, the SQUIDs were heated up above their critical temperature, cooled and re-tuned to liberate the trapped magnetic flux. Meanwhile, the bolometer temperature was raised to 900 mK, above the critical temperature of the bolometers, for SQUID stability during tuning. The SQUID tuning $V^{PP} - I_b$ and $V - \Phi$ curves recorded at float during the re-tuning of the camera are also shown in Figure 6–4. Comparing the SQUID tuning curves recorded on the ground and during the in-flight re-tuning, the identical $V^{PP} - I_b$ curves and the $V - \Phi$ curves having the

same peak-to-peak amplitude demonstrate the proper restored performance of the SQUIDs. The shift in Φ explains the sudden change in the SQUID DC level at the payload was reaching 31 km. The different flux bias selected to tune the SQUID at float and on the ground shows the SQUIDs were operated in a regime that became highly non-linear at float.

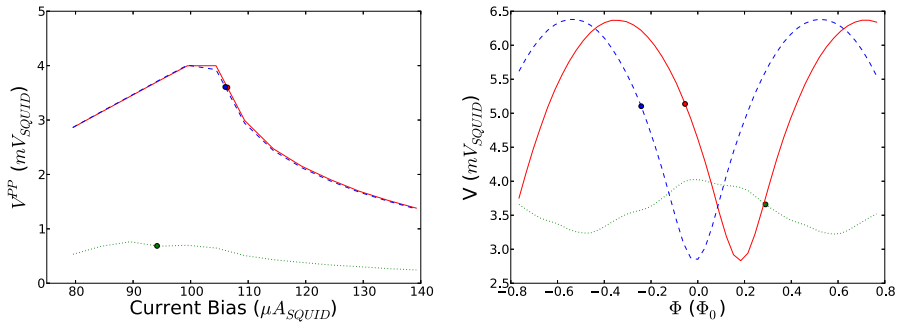

(a) (b)

Figure 6–4: Figure a) shows the peak-to-peak voltage response of SQUID B15 as a function of the provided current bias. Figure b) shows the voltage response of the same SQUID as a function of the flux bias at the tuned current bias. The blue dashed lines show the nominal tuning performed on the ground before launch. The green dotted lines show the reduced response tuning curve performed at float after the SQUID performance degraded at 16h20 UTC on June 11^{th}. The red solid lines show the restored proper performance of the SQUID after it was thermally cycled above its critical temperature. The red $V^{PP} - I_b$ curve is identical to the tuning performed on the ground. The red $V - \Phi$ curve has the same shape, but is shifted on the Φ showing the SQUID performance is restored and that the magnetic environment is different at float from on the ground. The circles on the curves show the selected SQUID current and flux bias points after the completion of the tuning procedure.

The difference in ground and at float SQUID tuning is an evidence for the magnetic environment to be different. The change in magnetic flux at float was unexpected, but allowed the demonstration of the commanding and readout system to completely set up the camera during flight. The recovery from this unexpected

event represents a major success from the NA flight. Measuring the absolute flux difference between the ground and at float is impossible due to the cyclic properties of the SQUIDs towards magnetic flux. Instead of modelling this very sensitive effect to the RFI shielding of the SQUIDs, SQUIDs are planned to be heated and tuned at float for the LDB flight to avoid such problems.

6.5 SQUID Stability at Float

The flight can be separated into three distinct time segments to analyze the stability of the readout system. The first segment is the ascension of the payload from launch (14h02 UTC on June 11^{th}) until the camera is required to be re-tuned (17h35 UTC on June 11^{th}). The second segment is the re-tuning period which occurs from 17h35 until 20h13 UTC on June 11^{th}, when the detector temperature has stabilized and the camera is in "observing noise" mode. The third segment of the flight is the observation time and represents the remainder of the flight. A number of 43 SQUIDs were tuned and operated at float. The SQUID functions properly when the DC level of its voltage output is 0 V. When the signal exceeds its dynamical range, the SQUID is said to be "jumped" a flux quanta and the DC level of the noise become a multiple of 0.7 V, becoming non-linear and losing its sensitivity.

Figure 6–5 shows the SQUID DC level of the representative SQUID A19 during the NA flight. During ascent, the SQUID system was unstable. On average, every SQUID "jumped" a flux quanta 4.2 times during this two and a half hour period and 42 of the 43 SQUIDs "jumped" a flux quanta at least once. Those SQUID "jumps" were corrected, but still represented 12% of the ascending time. This unstable period happens while the temperature of the detectors was cooling after the vibration

heating happening at launch as shown in Figure 6–2, as the payload temperature is subject to the ambient air variation as shown in Figure 6–1, and as the magnetic environment is changing as discussed in Section 6.4.

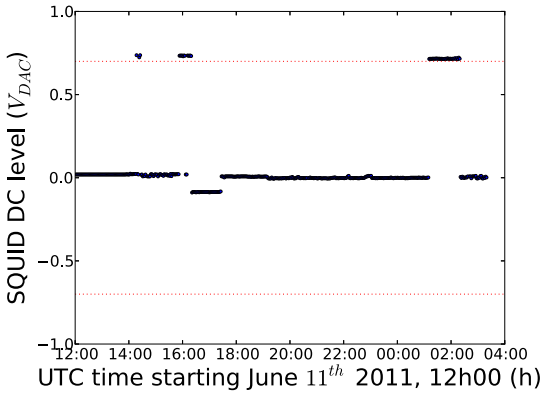

Figure 6–5: The SQUID DC level of the representative SQUID A19 during the NA flight. The dotted red lines show the limits where a SQUID has "jumped" a flux quanta. The SQUID is stable on the launchpad. It is unstable and "jumps" flux quanta regularly from launch (14h02 UTC on June 11^{th}) until the SQUID trapped magnetic flux at 16h20 UTC on June 11^{th}. The camera is retuned at 17h35 UTC on June 11^{th}. From 20h13 UTC on June 11^{th} until flight termination, the SQUID is stable except for a flux quanta "jump" recorded in 23 SQUIDs at 1h10 UTC on June 12^{th}.

After the camera was tuned, the system showed more stability. The SQUIDs "jumped" a flux quanta on average 0.6 times for the last seven hours of the flight and 24 of the 43 SQUIDs "jumped" a flux quanta at least once. A total of 23 of the SQUIDs "jumped" a flux quanta because of an unidentified event happening at 1h10 UTC on June 12^{th}. Those flux quanta "jumps" were straightforwardly recovered by the standard recovery algorithm. Removing those correlated flux quanta "jumps", only 0.05 "jump" per SQUID were recorded during the observing period of the flight. The SQUIDs were "jumped" for 12% of this period. Most of this period is explained

by the slow reaction of the commanding crew to correct the problem which left the receiver with 23 "jumped" SQUIDs for 68 minutes. The number of SQUIDs with a flux quanta "jump" during the stable operation of the flight is small given this flight was the first time a SQUID-based frequency domain multiplexed readout system was flown in a space-like environment and the facility they were recovered.

The extended delay before the SQUIDs were recovered exposed the omission of having display mechanisms to identify in realtime SQUID flux quanta"jumps". Such display windows have been programmed in preparation for the LDB flight and automated recovery will be implemented at opportune time (between the telescope scans) to avoid data degradation.

6.6 EBEX Detector Performance

In order to demonstrate the first proper operation of TES bolometers in a space-like environment, the understanding of the noise performance of the detectors has to be demonstrated. This section of the thesis presents the noise measurements in different configurations : the SQUIDs not attached to bolometers, the bolometers electrically biased above their superconducting transition, the bolometers electrically biased within their superconducting transition while being dark and at float. Each measurement introduces different components of noise studied separately. Bolometer measurements are performed at various deepness in their superconducting transition to adress the stability of the detectors.

6.6.1 SQUID Noise Measurements

For the NA flight, two SQUIDs were made dark by not being electrically connected to bolometers. The signals from those SQUIDs were demodulated at eight

evenly distributed frequencies from 200 to 900 kHz, covering the frequency band used to bias the bolometers. The demodulated frequencies were rounded to the nearest multiple of 117 Hz. This procedure ensured the undesired intermodulation distortion of the multiple voltage biases with one another is measured as a single peak at 117 Hz. The intermodulation distorsion is due to the non-linearities of the readout electronic components and are dominated by the SQUID. By forcing all carrier and demodulator frequencies to be multiple of 117 Hz, the intermodulation products can therefore only be demodulated to 0 or 117 Hz, outside of the bolometer bandwidth.

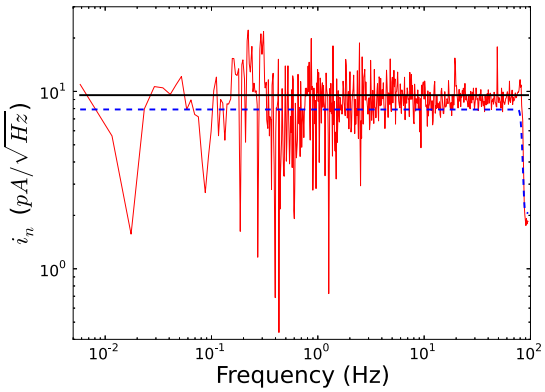

Figure 6–6: Power spectral density of SQUID B13 demodulated at 199836 Hz (red). The thick horizontal black line is the average measured noise between 2.2 and 2.7 Hz. The noise prediction is shown as a blue dashed line. The white noise level is measured to be 20% higher than the prediction. No HWP template is present in the timestream.

Figure 6–6 shows the PSD of the signal from SQUID B13 demodulated at 199836 Hz during the NA flight. No HWP peaks are present in the dark SQUID timestreams. Figure 6–7 a) shows the measured and predicted demodulated noise as a function of the demodulated frequency for dark SQUIDs B13 and B15 and Figure 6–7 b), the

distribution of their measured over predicted noise ratio. An excess noise superior to a factor of 2 with respect to the prediction is observed at 600 and 900 kHz. Excluding those two misbehaved frequencies, the SQUID noise is measured to be 11.0 $\frac{pA}{\sqrt{Hz}}$ on average, 40% higher than predictions.

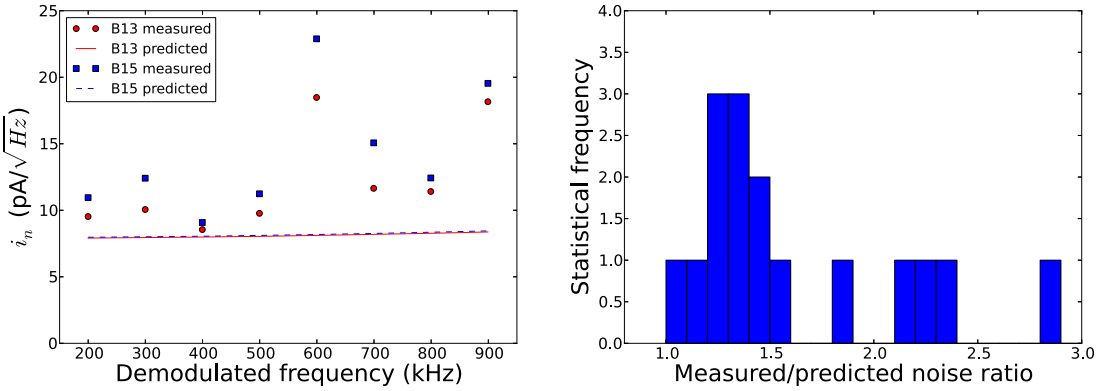

(a) (b)

Figure 6–7: Figure a) shows the measured (symbols) and predicted (lines) noise for SQUIDs B13 and B15 during the NA flight. The measured noise is superior to a factor of 2 when demodulated at 600 and 900 kHz as the other demodulated frequencies average 40% excess noise. Figure b) shows the distribution of the measured-to-predicted noise ratio for the same SQUIDs during the NA flight.

Post-flight, the excess noise demodulated at 600 and 900 kHz was not reproduced with the EBEX cryostat alone (i.e. when the cryostat was operated in the lab separate from the gondola). It is assumed to be due to a misconfiguration of the grounding between the subsystems before the NA flight, which may allow signals from elsewhere in the experiment, such as from switching power supplies operating at this frequency, to contaminate the SQUID signals as a ground bounce. The grounding configuration has been studied and a new, cleaner scheme implemented.

The proper noise performance of the SQUIDs is being verified during the pre-LDB flight integration of EBEX in Palestine, Texas in last Summer 2012.

The excess white noise is assumed to be due to having tuned the detectors when the bolometer stage had not yet reached its nominal operating temperature. After tuning, the stage cooled further, dropping the detectors lower into their transition. The detectors reached a point so low in their transition that they became unstable, and began to oscillate. This behaviour has been shown in the laboratory to contaminate the noise performance from neighbouring SQUIDs, presumably through electrical or magnetic crosstalk of high noise between squid channels.

Noise from SQUIDs was also measured in a testing cryostat closed to outside light located in a well controlled RFI free environment. The four SQUIDs P6-s1, P6-s2, P6-s5 and P6-s7 were attached to bolometers and demodulated at frequencies between TES bias frequencies to avoid bolometer Johnson noise. The bolometer wafer was maintained at $\sim$800 mK, above the critical temperature of the bolometers, to avoid SQUID instabilities. Figure 6–8 shows the measured and predicted noise as a function of the demodulated frequency and the measured-to-predicted noise ratio distribution. This measurement was performed after the NA flight and used the 16 demodulator channels to probe a larger frequency range. The noise is measured to be nominal, 8.3 $\frac{pA}{\sqrt{Hz}}$. The latest measurement shows nominal noise can be achieved, ruling out the possibility of the noise prediction being systematically underestimated for the NA flight results since the same methodology is followed.

For the reminder of this chapter, the components of the bolometer noise predictions present in the SQUID noise configuration are corrected to take into account

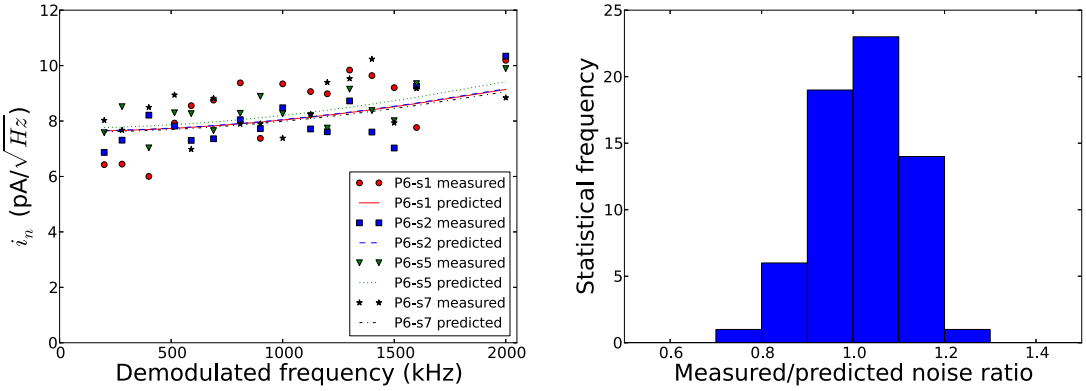

(a) (b)

Figure 6–8: Figure a) shows the measured (symbols) and predicted (lines) noise for SQUIDs P6-s1, P6-s2, P6-s5 and P6-s7 measured in a testing cryostat located in a RFI free environment at McGill University. Figure b) shows the distribution of the measured-to-predicted noise ratio for the same SQUIDs. The noise measured is coherent with the prediction.

the measured value : those components are increased by 40% for the NA flight measurements and by the measured SQUID noise value for ground measurement if an excess noise is measured. High noise in the SQUID configuration can be due to the SQUIDs being too warm, in band pick up, out of band noise pick-up aliased down in the band, misconfiguration of the grounding, etc.

6.6.2 Bolometers Maintained Above their Superconducting Transition Noise

Noise with detectors electrically biased above their superconducting transition is measured to cross-check the behaviour of the whole readout chain since the detectors theoretically behave as resistors in this state. This bolometer state includes all components of the readout chain down to the detectors except for the most challenging noise components : the phonon and photon noise. During the NA flight, the camera

was always set in "camera tuning noise" mode while the detectors were electrically kept normal, causing the digitization noise to dominate other noise sources. The analysis of this data therefore does not bring any knowledge of the system unless the contributions of the noise are drastically high. Post-flight, such measurements were performed with the NA flight bolometers in the EBEX cryostat not integrated to the gondola.

In order to separate the excess of noise measured on the SQUID and readout from the bolometer noise, the components of the noise predictions present in the SQUID noise configuration due to the abnormally high SQUID temperature during this particular cryogenic run are replaced by their measured value. The top panels of Figures 6–9 a), b) and c) show the distribution of the measured to corrected prediction noise ratio for the 150, 250 and 410 GHz bolometers electrically biased above their superconducting transition, respectively. The median noise due to adding the sub-kelvin chain is a factor of 1.4, 1.2 and 1.4 times the prediction. The 250 GHz detectors show close to nominal noise as the 150 and 410 GHz detectors show noise noticeably higher than expectation with a greater number of anomalously high noise channels. Despite the slight noise excess, the measurement of bolometers in transition is pursued.

6.6.3 Dark Bolometer Noise as a Function of Deepness in Their Superconducting Transition

In the same post-flight setup described in Section 6.6.2, noise measurements as a function of deepness in transition are performed while the detectors are dark to improve the understanding of the noise performance at float. The detectors are made dark by closing the window of the cryostat and by taping over the feed-horns and

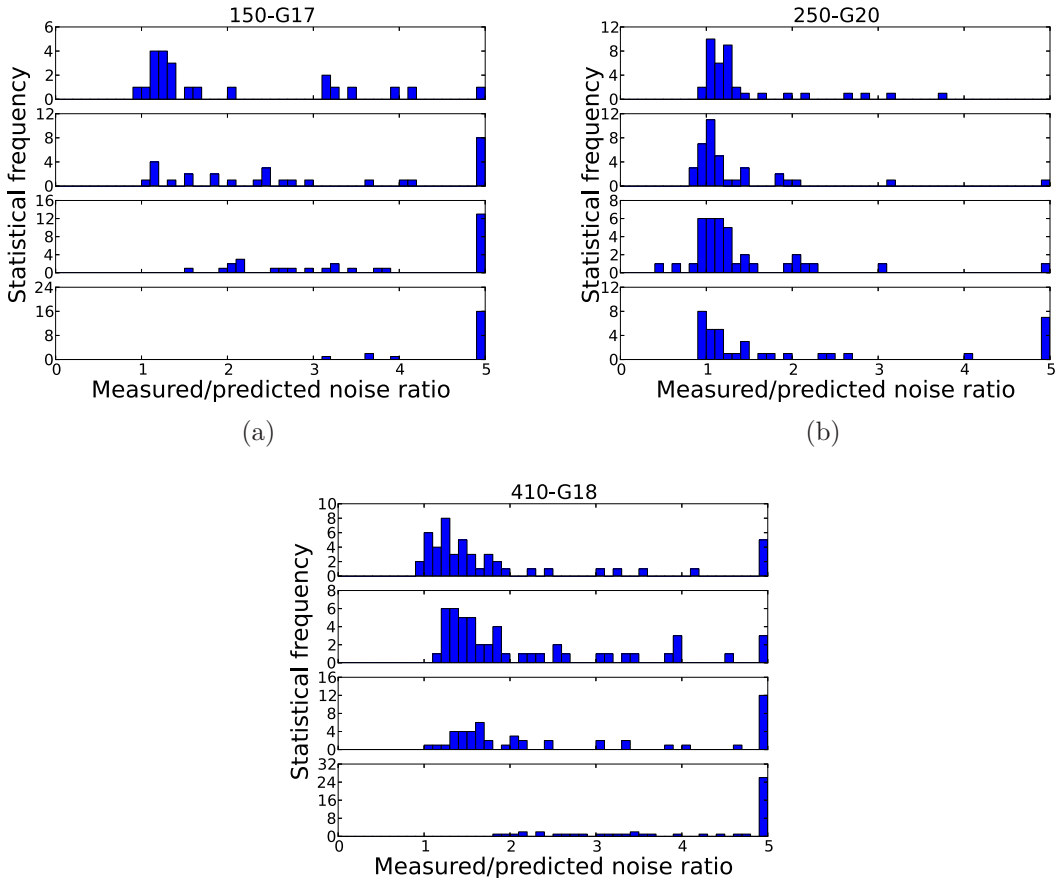

Figure 6–9: Figures a), b) and c) show the distributions of measured-to-predicted noise ratio for wafers 150-G17, 250-G20 and 410-G18, respectively, measured on the ground after the NA flight with the cryostat closed to light and not integrated with the gondola. Each figure shows such a distribution for, from top to bottom, bolometers electrically biased above their superconducting transition and bolometers dropped in their superconducting transition at 90%, 80% and 70% of their normal resistance. The noise prediction has been corrected for the excess noise measured with the SQUID only. All values greater than 5 are shown in the last bin and have been verified not to be clustered. The 250 GHz detectors are shown to be stable as they are dropped in their superconducting transition and the 150 and 410 GHz detectors are shown not to be.

the waveguides. No leaking light reaching the bolometers is assumed. Dark detector measurements have the same noise contributions as bolometers electrically biased above their superconducting transition with an extra noise source : the phonon noise from the bolometers. Figure 6–9 shows the distributions of the measured to corrected predicted noise ratio for the three NA flight wafers as a function of three operating points in the transition : 90%, 80% and 70% of their bolometer normal resistance. The readout components of the noise are corrected by the measured noise value from the SQUID noise configuration.

The detectors from the bolometer wafer 150-G17 show a median noise of 2.4, 3.6 and 13.2 times the predicted noise when the TES are operated at 90%, 80% and 70% of their normal resistance. Similarly, the detectors on wafer 410-G18 show a median noise of 1.7, 2.0 and 5.3 times the predicted noise when operated at the same deepnesses in their superconducting transition. Those measurements show the instability of the two wafers when operated too deeply in their superconducting transition. Similar noise degradation can be recreated in the lab when a SQUID dynamic range is used by signals picked up from unstable detectors that are oscillating. The time constant of the TES is inversely proportional to the loop gain $\mathcal{L}$. The loop gain increases as the detector is dropped further into his superconducting transition and therefore, the TES response becomes faster. When the TES responds faster to optical signals than the bolometer can thermally equilibrate, the TES is electro-thermally oscillating and its noise properties degrade. TES oscillations precede bolometers becoming superconducting.

The detectors from wafer 250-G20, however, show a median noise of 1.1, 1.1 and 1.3 times the predicted noise when the TES are operated at 90%, 80% and 70% of their normal resistance. Even though a few detectors have measured noise noticeably higher than prediction, the average detector only show a slight increase of noise when operated deep in transition, but close to nominal. Typically, experiments such as the SPT and APEX-SZ operate their TES bolometers 60-80% and 80-90% into their superconducting transition, respectively [73]. The depth into transition a bolometer can be stably operated at can vary significantly for different bolometer designs and parameters. Due to the lack of pre-flight knowledge about the at float loading and the bolometer resistance dependence to the applied voltage bias when the bolometer is maintained above its superconducting transition, the EBEX bolometers were operated 70% into transition. Post-flight measurements showed they should have been operated 80-90% into their superconducting transition to have stable performance. The 250 GHz detectors are judged to show stable performance.

The bolometer wafers flown for the engineering flight were prototypes and their parameters had not been tuned to the design values for science grade operation. The measurements presented in this section were done after the NA flight and their conclusions could not impact the decision of exploiting these three wafers for flight. However, the stability of wafer 250-G20 fullfils the requirement for the first operation of TES in a space-like environment [78]. The three wafers would have been flown even if the conclusions presented in this section would have been known before flight. The usage of these three NA flight wafers at float allowed a better understanding of the behaviour of the wafers so improvements could be implemented for the following

generation of TES bolometers that will be used for the LDB flight. As a result of those measurements, the thermal contact between the spiderweb, the thermal ballast and the TES of the bolometer has been improved for the LDB flight in detector fabrication, increasing the difficulty for the TES and the spiderweb to thermally decouple. Consequently, it will reduce bolometer electro-thermal oscillations and improve their stability.

6.6.4 Bolometer Noise During the NA Flight

Given results from section 6.6.3 and the operation of the detectors at 70% of their normal resistance during the NA flight, the 150 and 410 GHz bolometers are expected to be oscillating during the NA flight and we concentrate on the 250 GHz bolometers. Figure 6–10 a) shows the PSD of bolometer 250-G20-03-10 with a nominal noise performance during the NA flight. The residual of the HWP template are present on the timestream at harmonics of 2 Hz. Figure 6–10 b) shows the measured-to-predicted noise ratio for all bolometers properly tuned during the NA flight and fully characterized on the ground. The components of the noise predictions present in the dark SQUID measurements are corrected for the measured 40% excess noise at float, as described in Section 6.6.1.

The 150 and 410 GHz detectors show a noise distribution with a median noise of 1.9 and 2.8 times the predicted noise. However, the shapes of the distributions show a total incoherence between detectors in their noise performance that is consistent with the detectors oscillating. The 250 GHz detectors show a median noise that is 40% higher than prediction. All the detectors present in the last bin of the 250 GHz bolometer distribution are operated through the same SQUID. This

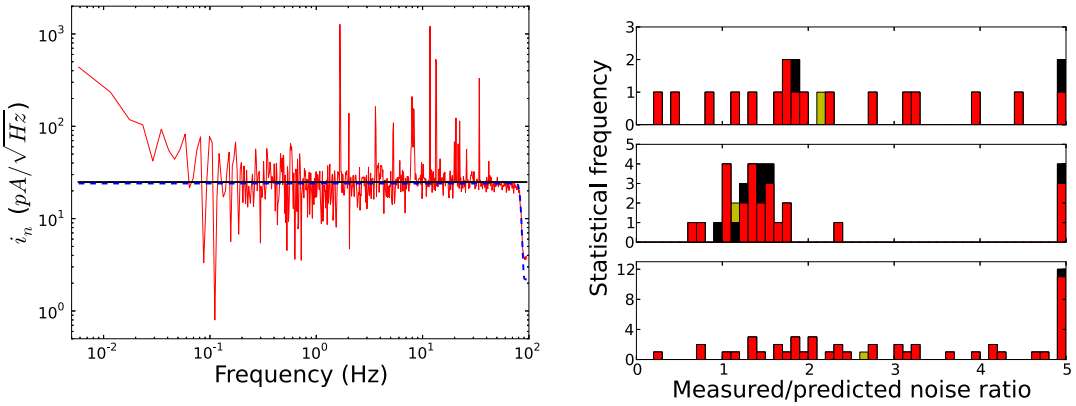

(a) (b)

Figure 6–10: Figure a) shows the power spectral density of detector 250-G20-03-10 in red. The thick horizontal black line is the average measured noise between 2.2 and 2.7 Hz. The noise prediction is shown as a blue dashed line. The white noise level is measured to be 4% higher than the prediction, i.e. nominal. The top, middle and lower panel of Figure b) show the distributions of measured-to-predicted noise ratio for NA flight bolometer wafers 150-G17, 250-G20 and 410-G18, respectively. The components of the predicted noise present in the dark SQUID measurements have been corrected for the 40% excess measured noise at float. The elements of the distributions are coloured red for bolometers opened to light, black for the bolometers closed to light and yellow for the bolometers covered with a neutral density filter. The highest bin in all three histograms include all values higher than 5 which have been verified not to be clustered.

multiplexed bolometer module shows bad performance such as a bolometer became superconducting and contaminated the noise performance of the other bolometers on the same multiplexed bolometer unit. The dark and "eccosorb" detectors are dispersed within the distribution of "light" bolometers showing the impossibility of a misevaluation of the photon noise by the measurement of the optical power at float being the source of the excess noise. The optical load is assumed to be zero for dark bolometers.

The bolometers were dropped in their superconducting transition while the bath temperature was 290 mK and still cooling towards its equilibrated temperature of 270 mK. From Equations 4.1 and 4.6, the bolometer resistance depends on the bath temperature according to

$$R(T_0) = \frac{V_b}{\sqrt{\bar{G}(T_0)(T_c - T_0) - P_{rad}}}. \quad (6.1)$$

The bolometers are therefore calculated to be on average 7, 4, 3% deeper in transition for the 150, 250 and 410 GHz bolometer, respectively. Consequently, the noise performance degrades due to the increased instabilities of the detectors.

Nevertheless, a fraction of the 250 GHz bolometers show nominal noise. Consequently, a proof of concept of the first proper operation of TES bolometers in a space-like environment was achieved during the EBEX NA flight.

6.6.5 Bolometer Noise as a Function of Deepness in Transition During the NA Flight

Towards the end of the flight, a subset of detectors was dropped at various fraction of their normal resistance. Figure 6–11 a) shows the measured resistance as a function of the voltage bias for bolometers 250-G20-11-01 and 410-G18-01-01. No 150 GHz detector is presented due to their SQUID instabilities during the measurement. The bolometers were initially electrically biased above their superconducting transition while the camera was in "camera tuning noise" mode. The bolometers were dropped at 90% of their normal resistance, the camera was set in "observing noise" mode, noise was recorded and the camera was set back in "camera tuning noise"

mode again. This succession of events is indicated by circles in Figure 6–11 a). This procedure was repeated, biasing the bolometers every time at 90% of their previous resistance until the bolometers became superconducting. Figure 6–11 b) shows the measured-to-predicted noise ration for bolometers 250-G20-11-01 and 410-G18-01-01 as a function of the fraction of the normal resistance of the detectors. The data recorded while the bolometers are superconducting are not shown in Figure 6–11.

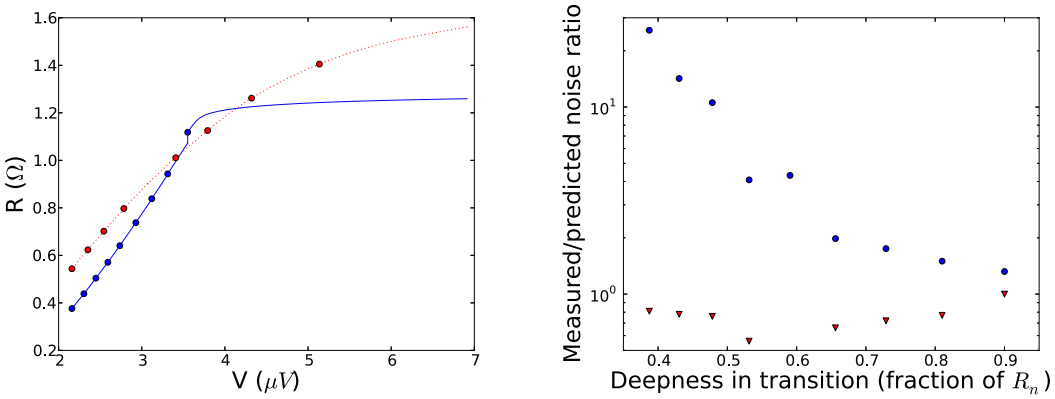

(a) (b)

Figure 6–11: Figure a) shows the bolometer resistance recorded as a function of the voltage bias applied to the bolometers 250-G20-11-01 (dotted red curve) and 410-G18-01-01 (solid blue curve). The circles present on these resistance curves show the resistances at which the noise performance of the bolometers were measured. Figure b) shows the measured-to-predicted noise ratio as a function of the fraction of the normal resistance of the bolometers 250-G20-11-01 (red triangles) and 410-G18-01-01 (blue circles).

Bolometer 250-G20-11-01 shows noise lower than prediction in general during the flight. This bolometer is an exceptionally low noise detector and, unfortunately, no other 250 GHz detector had its SQUID stable during the measurement. The measured noise is consequently stable as a function of deepness in transition, as

shown in Section 6.6.3. The average measured noise is 70% of the prediction with a standard deviation of 10%. Bolometer 410-G18-01-01 shows the same behaviour as when this measurement was performed on the ground. The noise increases as the detector is deeply dropped into superconducting transition. When the resistance is 70% of their normal resistance, both detectors show measured noise compatible with the noise measurements at float presented in Section 6.6.4.

Those results confirm the tendency of 410 GHz detectors to show noise degradation when operated too deeply in their superconducting transition as well as showing repeatable results for the measurements presented in Section 6.6.4.

6.7 Optical Loading

During the ascent of the payload, one detector per frequency band was repeatably dropped into its superconducting transition and re-biased above its transition. This procedure allows the measurement of the optical loading absorbed by the detectors as a function of altitude. This measurement is an unessential achievement of the NA flight since only the loading at float is required to proceed with the noise prediction. However, measuring the variation of loading with altitude is useful data to prepare EBEX for its LDB flight. The optical loading model used and the data analysis is presented.

6.7.1 Optical Loading Model

The transmission coefficient of a layer of atmosphere (τ_{atm}) at altitude z, with uniform pressure, temperature (T_{atm}) and precipitable water vapor, is calculated using a library based on the Atmospheric Transmission at Microwave (ATM) model developed for the Atacama Large Millimeter Array (ALMA) : ATM for ALMA [79].

The transmission coefficient is calculated as a function of frequency given the frequency resolution and the observing elevation angle. The ATM library also includes the absorption lines from the molecules present in the atmosphere that include oxygen (H_2O, O_2, O_3, ...). Oxygen is the dominant absorber and emitter of millimetre light in the atmosphere. The power emitted by a layer of atmosphere is calculated to be the absorbed power by the atmosphere due to a blackbody. The atmospheric power incident on the cryostat window is therefore the integral of the contributions from all the layers in the line of sight of the telescope

$$P_{atm} = A\Omega \int_{z_0}^{\infty} \int_{\nu_{low}}^{\nu_{high}} B(\nu, T_{atm}(z))[1 - \tau_{atm}(z)]d\nu dz, \tag{6.2}$$

where $A\Omega$ of the telescope throughput, z_0 is the telescope altitude, ν_{low} and ν_{high} are the frequency band limits of the telescope and B(ν, T_{atm}(z)) is the blackbody spectrum of a layer of atmosphere with thickness dz. The simulations presented in this thesis are a courtesy of Chaoyun Bao, University of Minnesota.

6.7.2 Optical Loading as a Function of Altitude

As the payload was ascending, bolometers were repeatably biased into and above their superconducting transition. By measuring the saturation power of the bolometers, the optical loading absorbed by the bolometers can be calculated. The end-to-end efficiency of the telescope and the non-atmospheric loading can be calculated by comparing the optical loading measured as a function of altitude to theoretical model presented in Section 6.7.1.

Figure 6–12 shows the electrical power provided to bolometers 250-G20-09-03 and 410-G18-12-01, respectively, as a function of the voltage bias as the TES bolometers are dropped into their superconducting transition at various altitudes. Bolometer 410-G18-12-01 is operated with strong electro-thermal feedback. When a bolometer is operated deep enough in its superconducting transition, the decrease of the voltage bias is compensated by the decrease of the bolometer resistance in the electrical bias power due to the strong electro-thermal feedback. The electrical power biasing the bolometer is then independent of the voltage bias as described in Section 4.2. This is visible in Figure 6–12 b) wherein the electrical power becomes flat deep in the transition (on the left hand side of each curve).

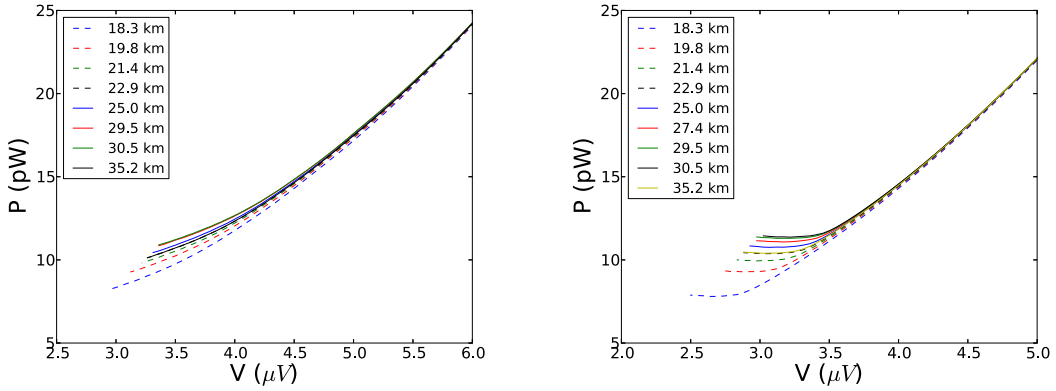

(a) (b)

Figure 6–12: Figures a) and b) show the electrical power biasing bolometers 250-G20-09-03 and 410-G18-12-01, respectively, as a function of the voltage bias for different altitudes.

When bolometer 250-G20-09-03 is biased into its superconducting transition, the region of strong electro-thermal feedback is not reached since the electrical biasing power decreases as the voltage bias is decreased and the detector does not

reach a point where the feedback is strong enough to flatten out the electrical bias power on the left hand side of the curves in Figure 6–12 a). The voltage dependence of the biasing power implies the bolometer response is not linear. This bolometer should have been biased deeper into its superconducting transition to be operated with strong electro-thermal feedback, as is the case for the 410 GHz detector. The uncertainty on the measurement of the saturation power of the detector and, therefore, of the optical loading absorbed by the detector as a function of altitude for bolometer 250-G20-09-03 is thus larger than for 410-G18-12-01.

The saturation power of the bolometers depends on the bath temperature and on the incident power. From Equation 4.27, the optical power absorbed by bolometers is $P_{rad} = P(T_0) - P_e(T_0)$. Figure 6–2 shows the variation of the bath temperatures after launch. The power conducted through the bolometer thermal link was obtained after the flight, as described in Section 4.6.2, and is calculated for every bath temperature the saturation power was measured. The measurement performed on the 150 GHz detector is not presented because post-flight characterization could not be performed. Figure 6–13 shows the optical power absorbed by both bolometers as a function of the altitude after the temperature dependence of the bath is removed.

In addition to the absorbed power as a function of altitude, the simulated atmospheric loading $P_{atm}(z)$, described in Section 6.7.1, is also shown in Figure 6–13. As EBEX reaches float altitude, only the atmospheric loading is expected to change. Therefore, the absorbed power by the bolometer follows

$$P_{rad}(z) = \eta P_{atm}(z) + P_{DC}, \tag{6.3}$$

where η is the end-to-end absorption efficiency of the experiment and P_{DC} is the non-atmospheric power absorbed by the bolometers. The relation between the measured and theoretical optical loading as a function of altitude is fitted for η and P_{DC}. The resulting fits are shown as green curves in Figure 6–13. From these fits, bolometers 250-G20-09-03 and 410-G18-12-01 have total end-to-end efficiencies of 4.5 and 3.4% and absorb 5.9 and 0.5 pW of non-atmospheric loading, respectively.

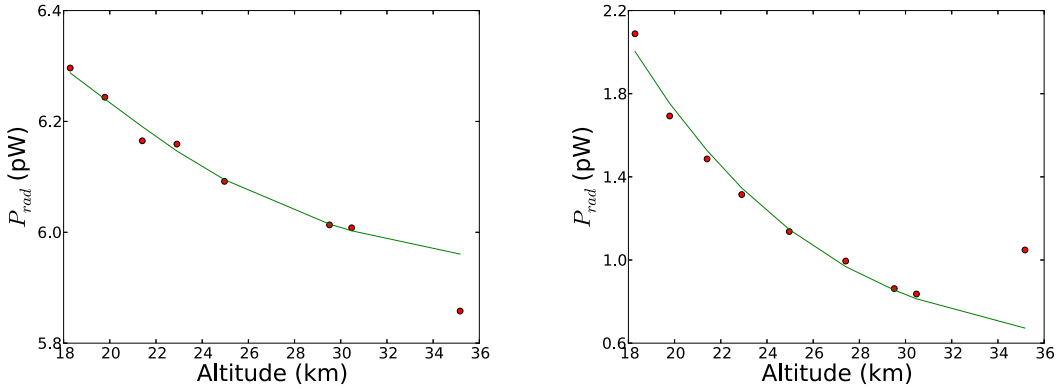

(a) (b)

Figure 6–13: Figures a) and b) show the optical loading measured (circles) by bolometers 250-G20-09-03 and 410-G18-12-01, respectively, as a function of altitude. The green curves are the fitted theoretical models.

The data measured at 35.2 km is inconsistent with the rest of the dataset, and has been excluded for the purposes of the fit. The optical power absorbed by the bolometers is expected to decrease as the altitude increases. This behaviour is observed for the data measured at all altitudes except at float. The excess of 0.4 pW measured for bolometer 410-G18-12-01 compared to the model suggests unexpected loading was present when the bolometers were dropped in their superconducting

transition at float. A period of two hours and 27 minutes separate the loading measurements performed at 30.5 and 35.2 km. During this time period, the array was fully re-setup and the gondola was mistakenly pointed towards the azimuth of the Sun. However, the Sun's elevation was 55^o above the fixed elevation of the gondola, meaning the telescope did not point directly at the Sun. The heating of the teflon filter of the cryostat by 40 K would account for this extra loading. However, since no temperature sensor was located on the cryostat filters during flight, its temperature is impossible to verify directly. This potential heating of the teflon filter would create an excess loading of 0.2 pW in bolometer 250-G20-09-03. This detector shows a decrease of 0.1 pW when comparing the data and the fitted simulation in Figure 6–13, which is small compared to the total 5.9 pW absorbed by the bolometer. This decrease as well as a potential excess loading of 0.2 pW are both consistent with the simulated curve due to the operation of this bolometer not deep enough in its superconducting transition.

A potential excess loading caused not only by the teflon filter, but by a combination of the optical elements located at the 77 K stage, which is more problematic than a single optic element being warm, would decrease the required temperature of the teflon filter needed to explain this outlying data point measured at 35.2 km. Given that this last data point was measured in different conditions than all the previous ones, it is justified to disregard it for the data fit.

6.8 Summary

Transition edge sensor bolometers with a multiplexed SQUID readout have been operated from a balloon platform for the first time during the EBEX engineering flight on June 11^{th} 2009. The digital frequency domain readout electronics designed for EBEX successfully tuned, monitored and operated the TES detectors and SQUIDs in a space-like environment. Bolometer sensitivity at the expected level was achieved for a subset of the detector channels and the SQUIDs were shown to be stable in "observing noise" mode. The readout system did not overheat during the NA flight, but showed potential risk of overheating during the LDB flight. Additional cooling is being implemented. The optical loading was successfully determined at float altitude. This demonstration increases the technology readiness for TES bolometers and the DfMUX with SQUID readout system for satellite applications. The NA flight was overall a success, showing a proof of concept that the technology EBEX is exploiting is suitable for an Antarctic science flight.

CHAPTER 7
Readiness for the EBEX Long Duration Flight

The June 2009 engineering flight allowed to successfully test the EBEX telescope and camera before the LDB flight, an expected 11 day flight in Antarctica scheduled for the Austral Summer of 2012-2013, could be approved by NASA. This LDB flight presents the challenges of allowing only one selection of detectors to be flown and operating a large number of bolometers with limited human interactions with the hardware. This chapter describes the calculation of the bolometer specifications, the expected noise performance of the bolometers, the camera setup procedure and the software for monitoring the performance of the camera during the LDB flight.

7.1 Bolometer Specification Calculations

The optimization of the thermal conductance parameter of the bolometers is essential to maximize the sensitivity of the camera. The readout electronic noise and the bolometer Johnson, phonon and photon noise contribute to degrade the performance of the camera. Photon noise is intrinsic to photon detection and dominates the noise performance of optimized cameras. The thermal conductance and the critical temperature of the TES bolometers are required to be optimized so the noise contributions to the camera are minimized. Bolometers with excessively high thermal conductance have most of their dynamic range used by the electrical bias instead of photons. However, bolometer saturation must be avoided since it prevents photons from being detected. An equilibrium between having an ultra-sensitive camera and

the risk of saturating the bolometers must be achieved. The readout electronics has to be built to provide a small noise contribution compared to the photon noise. The bolometer Johnson noise, after suppression, also has to be small compared to the photon noise.

This section describes the cold optics of EBEX, calculates of the expected incident power on the bolometers for the LDB flight and derives the bolometer specifications.

7.1.1 The Optics of the EBEX Telescope

The optical path of photons in the EBEX camera is described in Section 3.3.3. The optic elements are poor electrical conductors to minimize the fraction of light they absorb. The fraction of absorbed light by the i^{th} optical element is

$$A_i(\nu) = 1 - exp\left(-\left[\frac{2\pi n_i \nu}{c}\right] tan(\delta_i) d_i\right), \tag{7.1}$$

where n_i is its refractive index, $tan\delta_i$ is its loss tangent, d_i is its thickness, c is the speed of light and ν is the photon frequency. The absorption coefficient increases with photon frequency. The characteristics of the optic media are obtained from tabulated values [80, 39, 81]. The first optical element is defined to be the primary mirror and the n_{el}^{th} optical elements, the closest element to the bolometers. For the purpose of this discussion, the mirrors are assumed to be perfect transmitters, so all incident photons reach the cryostat window. The reflection coefficient of each surface of the polypropylene LPE filters and the AR coated HWP are 0.010 from measurements

performed at Cardiff University. The ultra-high molecular weight polyethylene cryostat window, pupil and camera lenses and the Rexolite[1] field lens are anti-reflection coated with ultra-high molecular weight polyethylene and the reflection coefficients of each surface are 0.013, 0.020 and 0.013 within the 150, 250 and 410 GHz bands, respectively, from measurements performed at Cardiff University. Assuming normal incidence for the photons, the reflexion coefficient of the teflon filter is

$$R_4 = \left| \frac{n_i - 1}{n_i + 1} \right|^2 . \tag{7.2}$$

The fraction of transmitted light through the i^{th} optical element is therefore, to first order,

$$\tau_i(\nu) = 1 - A_i(\nu) - 2R_i, \tag{7.3}$$

where each optical element has two surfaces. Table 7–1 shows the transmission coefficients calculated from Equation 7.3 for all the optical elements of the EBEX telescope [30]. The cumulative transmission coefficient of the optics of the EBEX camera to a single focal-plane is 35, 28 and 21% for 150, 250 and 410 GHz photons,

[1] www.rexolite.com

so 70, 56 and 42% of the incident light onto the cryostat reaches the two EBEX focal planes.

Table 7–1: Transmission coefficients of the different optical elements in the EBEX cryostat to a single focal plane for the LDB flight within the 150, 250 and 410 GHz observing frequency bands calculated from Equation 7.3.

Optical element	150 GHz	250 GHz	410 GHz
Primary mirror	1.00	1.00	1.00
Secondary mirror	1.00	1.00	1.00
Cryostat window	0.97	0.96	0.97
Teflon filter	0.95	0.93	0.88
LPE1 filter	0.98	0.98	0.97
LPE2 filter	0.98	0.98	0.96
Field lens	0.96	0.93	0.83
LPE2b filter	0.98	0.97	0.96
HWP	0.94	0.93	0.91
Pupil lens 1	0.97	0.93	0.90
Pupil lens 2	0.97	0.93	0.90
Polarizing grid	0.50	0.50	0.50
Camera lens	0.97	0.94	0.91
Total	0.35	0.28	0.21

The optical model of the cold optics allows to understand the path of the photons in the EBEX cryostat. In the next section, this model is used to estimate the optical power incident on the detectors.

7.1.2 Optical Loading

The optical loading absorbed by the bolometers defines the lowest allowed thermal conductance of the bolometers. The incident power on the bolometers from the cold optical elements in the EBEX cryostat is calculated to be

$$P_{i\ inc} = A\Omega \int_{\nu_{low}}^{\nu_{high}} \epsilon(\nu) I(\nu, T_i) \prod_{j=i+1}^{n_{el}} \tau_j(\nu) d\nu, \tag{7.4}$$

where $A\Omega$ is the detector throughput, $\epsilon(\nu)$ is the emissivity of the source, $I(\nu, T_i)$ is the blackbody intensity spectrum with temperature T_i and ν_{low} and ν_{high} are the limits of the observed EBEX frequency band. The atmosphere also contributes to the loading on the detectors. Figure 7–1 shows simulations[2] of the emitted atmospheric power as a function of altitude for various elevations within the EBEX frequency bands. These simulations are described in Section 6.7.1. At the lowest elevation EBEX will observe (30°) and assuming a conservatively low altitude of 30 km for the payload, the incident atmospheric power on the cryostat window is calculated to be 0.12, 1.2 and 6.4 pW within the 150, 250 and 410 GHz bands, respectively.

The expected incident power on the bolometers emitted by the different thermal sources are summarized in Table 7–2 for the three different EBEX observing bands. The expected incident power on the bolometers within the 150, 250 and 410 GHz bands is 2.8, 8.5 and 15.3 pW, respectively, and is dominated by the optical elements in the cryostat. This power is then absorbed by the bolometers with an absorption efficiency η_{bolo}. The CMB contributes only a small fraction to the total power on the bolometers.

[2] Courtesy of Chaoyun Bao, University of Minnesota.

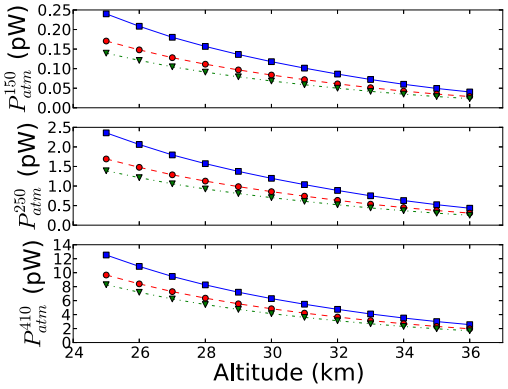

Figure 7–1: Atmospheric power incident on the cryostat window for telescope elevations of 30^0 (squares), 45^0 (circles) and 60^0 (triangles) in the 150, 250 and 410 GHz EBEX frequency bands. [Figure courtesy of Chaoyun Bao, University of Minnesota]

7.1.3 Bolometer Specifications

To calculate the saturation power specifications for the bolometers, typical bolometer absorption efficiencies of 60, 50 and 40% for the 150, 250 and 410 GHz bolometers are assumed. The absorbed optical to electrical ratio by the bolometers is assumed to be 1:1.5, which provides a small safety margin and decreases the chances of saturating the bolometers. The saturation power specifications of the detectors are therefore calculated by multiplying the incident power on the bolometers by the bolometer absorption efficiency and the electrical biasing power margin factor of 2.5. The saturation power specifications are 3.6, 8.7 and 12.0 pW for the 150, 250 and 410 GHz bolometers, respectively.

Separate measurements were performed to increase the confidence in the specifications. Two 150 GHz bolometer wafers were characterized dark in both the EBEX cryostat and a cryostat optimized for wafer characterization. The bolometer wafers

Table 7–2: Incident power on the EBEX bolometers emitted by the different thermal sources as a function of the photon frequency.

Source	T K	150 GHz pW	250 GHz pW	410 GHz pW
CMB	2.73	0.2	0.1	0.0
Atmosphere	263	0.0	0.4	1.4
Primary mirror	263	0.4	1.0	1.1
Secondary mirror	263	0.4	1.0	1.1
Cryostat window	263	0.0	0.1	0.3
Teflon filter	110	0.8	2.8	5.2
LPE1 filter	95	0.0	0.2	0.6
LPE2 filter	20	0.0	0.0	0.1
Field lens	9	0.0	0.1	0.3
LPE2b filter	7	0.0	0.0	0.0
HWP	50	0.4	1.2	1.8
Pupil lens #1	1.5	0.0	0.0	0.0
Pupil lens #2	1.5	0.0	0.0	0.0
Polarizing grid	2.5	0.0	0.0	0.0
Camera lens	1.5	0.0	0.0	0.0
Total	n/a	2.4	6.9	12.0

were located in a light tight box when characterized in the testing cryostat as the optical path of photons was blocked by taping over the feed-horns and the waveguides in the EBEX cryostat, which had its window closed. The two bolometer wafers have a saturation power measured to be 1.2 pW higher, on average, in the testing cryostat, showing hints of unaccounted power in the EBEX cryostat. In the same conditions, a 250 GHz wafer shows a saturation power measured to be 3.8 pW higher in the testing cryostat. To account for this extra power, the saturation power specifications of the bolometers are therefore increased to 4.8, 12.5 and 14.6 pW for the 150, 250 and 410 GHz frequency bands, respectively. The 410 GHz excess power is calculated to be 2.6 pW by extrapolating the excess power from the 150 and 250 GHz to 410 GHz by assuming a 4 K blackbody source.

Fabricating bolometer wafers with the proper specified parameters is an iterative process. The bolometers are fabricated in the facilities of University of California, Berkeley. The size of the nitride legs conducting the heat from the spiderweb of the bolometers to the bath is initially set. The legs dominate the thermal conductance of the bolometers. The saturation power is then measured in the McGill University or the University of Minnesota facilities. The fabrication process is then adjusted to modify the critical temperature of the following bolometers by varying the ratio of aluminum to titanium layers forming the TES. This procedure fine tunes the saturation power and also modifies the normal resistance of the detectors. Table 7–3 summarizes the specifications of the bolometer wafers for the LDB flight. The normal resistances and critical temperatures shown in Table 7–3 were measured on fabricated wafers and are free to vary. The geometry of the legs is only modified when the critical

temperature required to meet the thermal conductance specifications leads to values lower than 400 mK or higher than 600 mK. The lower limit is set by the detector stage temperature and the higher limit, by the noise performance of the camera.

Table 7–3: Specifications of the EBEX LDB flight bolometers.

Parameter		150 GHz	250 GHz	410 GHz
P_{rad}	(pW)	2.6	7.3	7.4
P_0	(pW)	4.8	12.5	14.6
G	$\left(\frac{pW}{K}\right)$	41	86	100
T_c	(mK)	450	510	500
R_n	(Ω)	1.8	1.5	1.4
V_b	(μV_{RMS})	1.8	2.5	2.8

A series of bolometer wafers is fabricated and tested, aiming to meet the specifications of the detectors through an iterative process. The 14 bolometer wafers possessing the closest characteristics to the specifications, the best uniformity in their parameters and with the highest number of bolometers, together maximizing the mapping speed of the sky, will be selected for the LDB flight. Enough bolometer wafers to fill the two EBEX focal planes, meeting specifications and minimum yield, have been produced. However, to optimize the sensitivity of the camera, the fabrication process and the wafer characterization will continue until the final integration of EBEX in Antarctica so the detector yield is increased, the parameters better match specifications and the parameter distributions are more uniform.

7.2 Camera Noise Performance Predictions

Assuming the detector specifications are met, the noise performance of the bolometers has to be shown to meet requirements so EBEX can achieve its science

goals. The detector stage temperature and the absorbed power by the bolometers can both vary from expectations and impact on the noise performance of the camera. This section calculates the expected bolometer noise performance as a function of these parameters.

The bath temperature of the EBEX cryostat is expected to be 270 mK from measurements performed in past cryogenic runs. However, it can change by up to 30 mK due to variations in the temperatures of the EBEX optical elements and to the variability in the assembly of the thermally conducting interfaces in the cryostat from one cryogenic run to another. Figure 7–2 shows the expected noise performance of the 150, 250 and 410 GHz bolometers for the LDB flight as a function of the bath temperature. The detailed calculation of the noise performance of the bolometers is described in Appendix B. The average thermal conductance is inversely proportional to $(T-T_0)$ and the voltage bias is calculated to be $V_b = \sqrt{R(P_0 - P_{rad})}$. The thermal conductance increases as the bath temperature approaches the bolometer critical temperature and also causes the phonon component of noise to increase. The effects of the phonon noise increase on the total noise performance of the bolometers is small for detector stage temperatures smaller than 350 mK. The readout electronics and the bolometer Johnson noise contributions are mostly independent of the detector stage temperature. The possible variations of detector stage temperature in the EBEX cryostat with respect to the expected value will therefore not degrade the noise performance of the detectors during the LDB flight.

The absorbed power by the detectors could differ from expectations during the LDB flight due to the uncertainties in the calculations presented in Section 7.1.2.

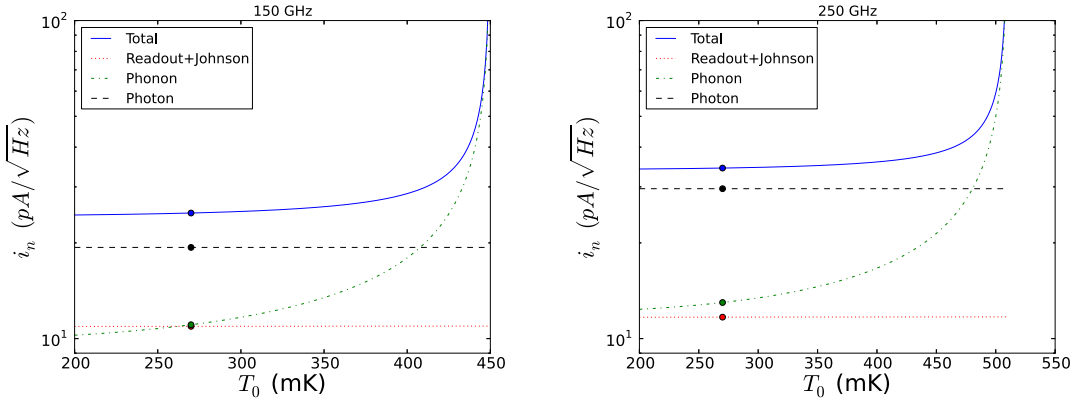

(a)

(b)

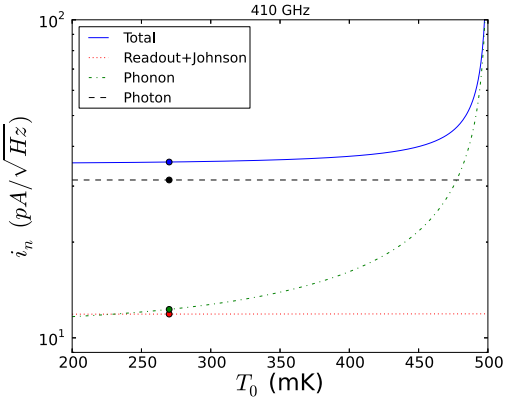

(c)

Figure 7–2: Figure a), b) and c) show the predicted noise performance of the 150, 250 and 410 GHz bolometers, respectively, for the LDB flight as a function of the temperature of the detector stage. The readout electronics, bolometer Johnson, phonon, photon and total noise curves are shown. The circles show the noise performance of the detectors at the expected bath temperature of 270 mK. The highest bath temperature shown on the plots are set by the critical temperature specifications for the LDB flight bolometers.

Figure 7–3 shows the expected noise performance of the 150, 250 and 410 GHz bolometers for the LDB flight as a function of the absorbed power in the bolometers. The readout electronics and the bolometer Johnson noise contributions are mostly

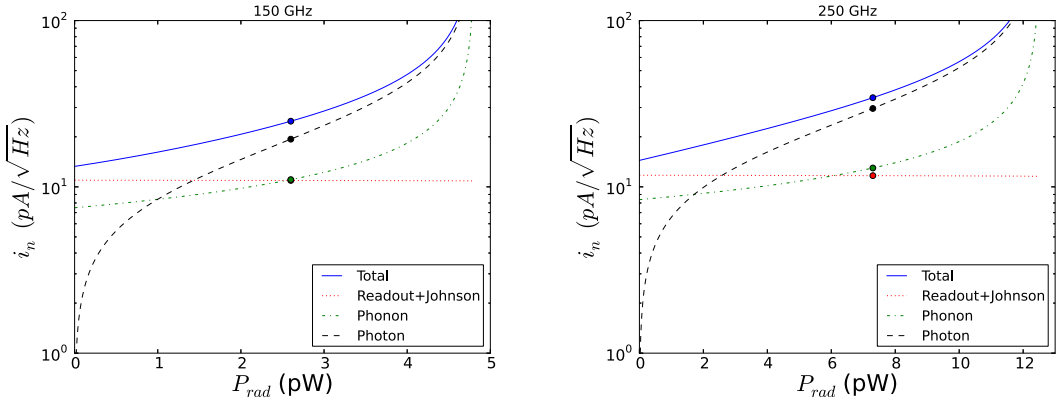

(a) (b)

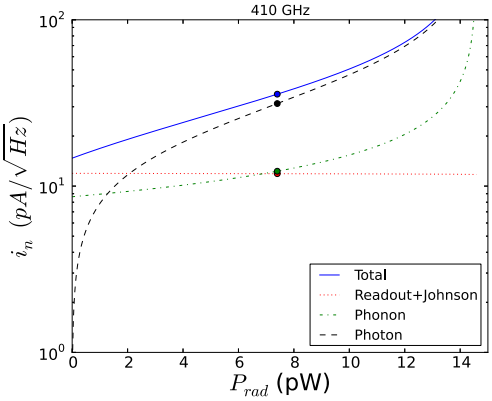

(c)

Figure 7–3: Figure a), b) and c) show the predicted noise performance of the 150, 250 and 410 GHz bolometers, respectively, for the LDB flight as a function of the absorbed power by the bolometers. The readout electronics, bolometer Johnson, phonon, photon and total noise curves are shown. The circles show the noise performance of the detectors with the expected absorbed power. The highest absorbed power shown on the plots are set by the saturation power specifications for the LDB flight bolometers.

independent of the absorbed power by the bolometers. The bolometer bias voltage decreases as the optical power absorbed by the bolometers increases. The phonon and the photon noise therefore drastically increases when the optical loading approaches

the saturation power of the bolometers. The camera is expected to be photon noise dominated in its three frequency bands. If the power absorbed by the bolometers were to be much smaller than expected for the nominal bolometer parameters, the performance of the camera would degrade significantly. The camera would then be dominated by readout electronics, bolometer Johnson and phonon noise and the camera sensitivity would be much lower than nominally expected. The calculation of the expected absorbed power by the bolometers is dominated by the optical elements in the cryostat and has been crosschecked with measurements performed using a temperature controlled thermal load located on the cryostat window to increase confidence in the specifications of the saturation power.

The readout electronics and the bolometers have been designed so their noise contributions are small compared to the photon noise. Table 7–4 summarizes the expected noise performance of the bolometers for the LDB flight. The demodulation factors of $\sqrt{2}$ are emphasized. EBEX is expected to have a photon noise dominated camera during its LDB flight.

Table 7–4: Bolometer noise predictions for the EBEX LDB flight.

Noise source	150 GHz $\frac{pA}{\sqrt{Hz}}$	250 GHz $\frac{pA}{\sqrt{Hz}}$	410 GHz $\frac{pA}{\sqrt{Hz}}$
Warm readout	$\sqrt{2} \cdot 4.0$	$\sqrt{2} \cdot 4.2$	$\sqrt{2} \cdot 4.3$
Cold readout	$\sqrt{2} \cdot 5.2$	$\sqrt{2} \cdot 5.2$	$\sqrt{2} \cdot 5.3$
Johnson	$\sqrt{2} \cdot 4.2$	$\sqrt{2} \cdot 4.8$	$\sqrt{2} \cdot 5.0$
Phonon	11.1	13.0	12.3
Photon Poison	16.6	25.9	29.1
Photon correlation	9.5	14.4	11.7
Total	24.8	34.4	35.7

7.3 EBEX Focal Plane Monitoring

During the EBEX LDB flight, 112 SQUIDs and 1564 bolometers will be operated. The efficient monitoring of the performance of this system represents a challenge in a 11 day balloon flight due to the limited interaction with the camera. This section describes the methodology that will be followed to ensure the proper setup of the camera and the monitoring of the bolometers while the telescope is in "observing noise" mode.

To monitor the performance of the camera during the camera setup, a result file will be written to disk summarizing the actions performed and the state of the SQUIDs or bolometers after every operation. The monitoring of the camera setup could be automated within the FCP or performed from the ground station by the camera operator using the downlinked result files. EBEX is the first experiment to have operated TES bolometers in a space-like environment and will be the first experiment to operate them in a long-duration flight. The complexity of the possibly unexpected malfunctions at float increases the risks of implementing a fully automated algorithm on the FCP. Unexpected situations could lead to unnecessary long operations and shutdown of SQUIDs and bolometers. For instance, the event causing all SQUIDs to trap magnetic flux was unexpected during the NA flight, as described in Section 6.4, and the camera would not have been recovered by an automated program if such an algorithm would have been implemented in the FCP for the NA flight. The limited observing time at float due to limited cryogenics motivates a more conservative approach. During the EBEX LDB flight, the monitoring of the array will be performed on the ground using the downlinked result files. The

downlinking bandwidth will allow for all result files to be available to the camera operator. Operations to correct the array malfunctions will be initiated by the camera operator.

The standard camera setup procedure involves raising the temperature of the bolometers above their critical temperature, tuning the SQUIDs, biasing the bolometers above their superconducting transition, cooling the detector stage temperature below the critical temperature of the bolometers and biasing the bolometers in their superconducting transition once the detector stage temperature has stabilized. The SQUIDs will be heated above their critical temperature before their first tuning at float and will be re-heated only if they trap magnetic flux afterwards. The stabilization of the detector stage temperature is the most time consuming step in the procedure ($\sim$4 hours). To optimize the observing time, the camera is set up while the refrigerators are being cryogenically cycled since this procedure already involves raising the detector stage temperature above the critical temperature of the bolometers.

Figure 7–4 shows the algorithm followed during the setup of the bolometer array. The tuned SQUIDs are verified not to have trapped magnetic flux. Faulty SQUIDs are reheated above their critical temperature to restore their proper performance. A nominal tuned SQUID has a minimal voltage-to-magnetic flux response and a DC level of 0 V. The bolometers, when biased above or into their superconducting transition, are verified not to be latched in a superconducting state. The required current required to null the current though a voltage biased bolometer latched in a superconducting state is greater than the maximal current that can be generated by

the DfMUX readout electronics. Misbehaved multiplexed modules will be turned off by removing the SQUID and bolometer biases and will be re-biased during the next refrigerator cycle. SQUIDs and bolometers with unclear status will be investigated, trading off investigating time for potential camera sensitivity gains. A typical investigation involves the perturbation of the current nulling the bolometer bias and the comparison of the result with the expected response.

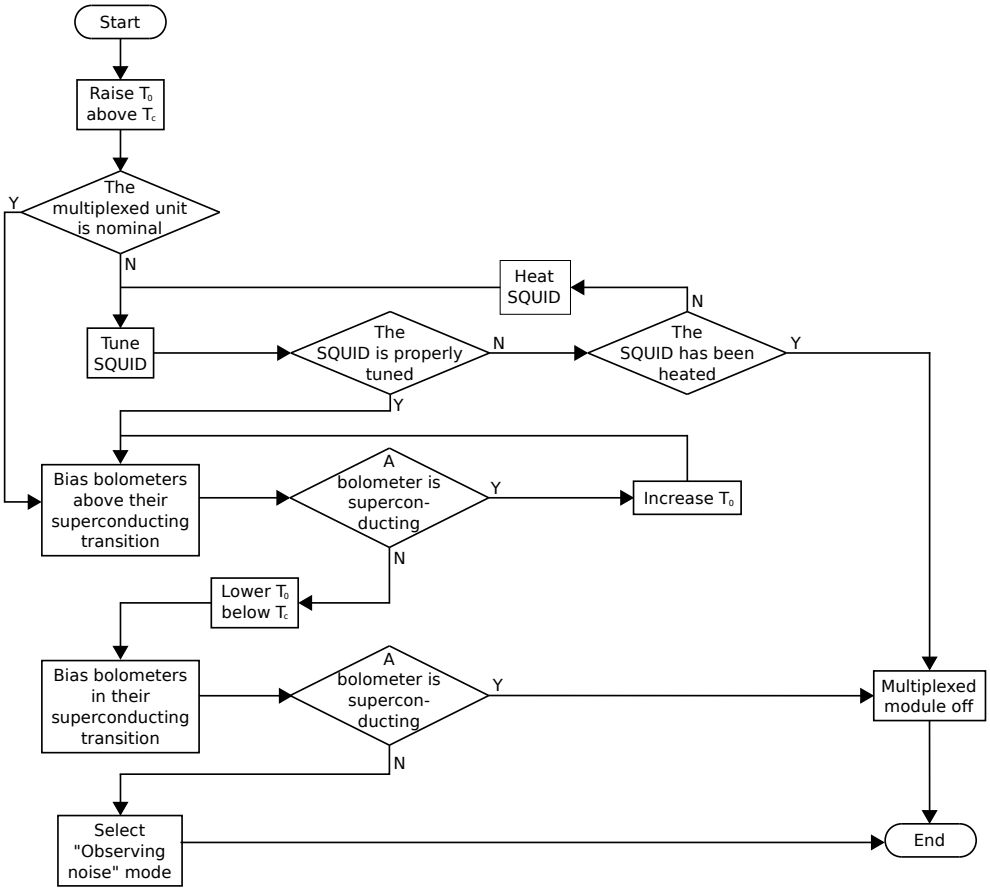

Figure 7–4: Algorithm ensuring the nominal setup of the EBEX camera is achieved during the LDB flight.

The status of the bolometer array will be continuously monitored during the telescope observing time of the LDB flight to identificate malfunctioning SQUIDs and bolometers. For example, SQUID "jumps" and bolometer latching must be identified to prevent data degradation. The average and root mean square of the bolometer current for all channels will be written to disk every second. Figure 7–5 shows the methodology used to identify problematic SQUIDs and bolometers. All downlinked data will be processed as it becomes available to the camera operator. When a SQUID "jumps", the SQUID will be added to a list and a correcting algorithm will be performed on the faulty SQUIDs at opportune times to avoid data degradation. The bolometers will be monitored for latching in a superconducting state. Bolometers rarely latch when the operating conditions of the camera are stable. However they can become superconducting, for instance, when the temperature of the bolometer stage greatly decreases after the bolometers were dropped into their superconducting transition or when the incident power suddenly decreases. Special care is taken so the operating conditions of the camera are stable prior to dropping the bolometers into their superconducting transition. The signature of a superconducting detector is a sudden change in the current through it due to the decrease in the bolometer resistance. Also, this decrease of the bolometer resistance causes the Johnson noise to increase significantly, polluting the signals from the other bolometers on the same multiplexed module through current leakage and, at a lower magnitude, the other bolometers in the array through electrical crosstalk. The multiplexed modules with a latched bolometer, when the telescope is in "observing noise" mode, will have all

of their bolometer and SQUID biases turned off immediately and will be re-biased during the following refrigerator cryogenic cycle.

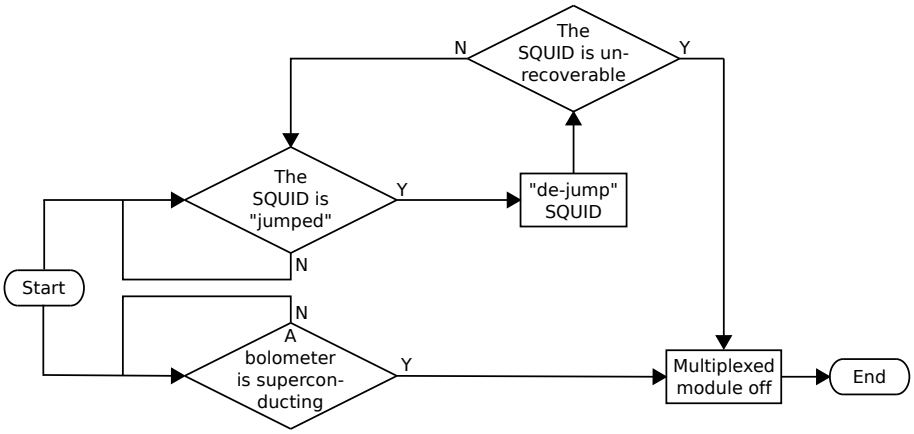

Figure 7–5: Algorithm ensuring the nominal performance of the EBEX camera during the LDB flight telescope observing time.

The monitoring software will parse every status file and will produce warnings to the camera operator. The operator will investigate, if necessary, the status of the multiplexed module and will upload to the FCP the required commands when the status of the telescope will allow for operations to be performed on the camera while minimizing data degradation. This conservative methodology minimizes the number of deactivated multiplexed modules due to malfunctions and allows to maximize the exposure of the camera.

7.4 Summary

The transmission through each EBEX optical element has been determined. This allows for the calculation of the expected incident power on the bolometers from all photon sources. The specified saturation power of the bolometer within the three EBEX observing frequency bands has therefore been calculated, providing enough

dynamic range to avoid saturation while maximizing the camera sensitivity. A series of bolometer wafers meeting the specified saturation power, critical temperature and normal resistance has been produced and characterized. The expected noise performance at float of these bolometers has been shown to be dominated by photon noise, allowing for the maximization of the camera sensitivity. An algorithm to allow for the monitoring of the camera setup and performance at float has been elaborated for the camera operator to optimize both the observing time of the telescope and the sensitivity of the camera. The EBEX camera has therefore been optimized and built to maximize the science return during its LDB flight in the Austral Summer of 2012-2013 over Antarctica.

CHAPTER 8
Conclusion

The CMB temperature anisotropies have been well-measured and its E-mode polarization has been observed by contemporary experiments. The signature of inflationary gravity waves is encoded in the B-mode polarization of the CMB, which EBEX will attempt to measure. Detection of this signature in the B-mode polarization would represent strong evidence for the postulated inflationary period of the universe. Concurrently to this goal, EBEX will characterize the polarized galactic dust and the gravitational lensing effects for scales $\ell > 100$.

EBEX is a state of the art telescope based on a mixture of innovative technologies and technologies well tested on balloon-borne platforms. The EBEX telescope was tested in a space-like environment for the first time during the June 2009 engineering 13.5 hour flight, flying over New Mexico and Arizona, USA. The SQUID-based DfMUX readout system and TES bolometers have been operated at float for the first time. The DfMUX readout system successfully tuned, monitored and operated the EBEX camera during the engineering flight. A subset of bolometers was shown to have nominal noise performance and to be stable while observing. The incident power absorbed by the bolometers has been measured. The NA flight was a success and represents a proof of concept of the technology EBEX will exploit during its LDB flight in Antarctica. This engineering flight increased the level of readiness for a potential future satellite mission for which EBEX represents a milestone.

In preparation for the science flight, the specifications of candidate bolometer wafers were characterized, allowing wafers to be chosen for the science flight that will have the required sensitivity and noise performance to meet the EBEX science goals. A series of TES bolometer wafers has been produced and characterized. Science grade wafers were produced to populate the 14 positions of the two EBEX focal planes. The multiplexing factor of the DfMUX system was improved from 8 to 16 bolometers per multiplexed module to maximize the number of operated bolometers. The bolometers were shown to be stable and to meet electrical crosstalk requirements. To ensure the proper performance of the receiver at float, a series of algorithms which will be applied on the downlinked data has been developed and tested.

In conclusion, the EBEX telescope has been built with the sensitivity to meet its LDB goal during its science flight scheduled for 11 days in the Austral Summer of 2012-2013 in Antarctica.

APPENDIX A
The DfMUX Transfer Functions

The transfer functions to convert the raw DfMUX board values to volts and amperes at the detectors are crucial before any data analysis can be performed. In the absence of on-sky calibration, EBEX uses a mixture of transfer functions theoretically calculated and measured in the laboratory. This appendix describes the SQUID theory as well as the transfer functions for SQUIDs operated in a flux-locked loop, the bolometer voltage bias, the nulling current and the demodulated current through the bolometers.

A.1 SQUID Theory

A SQUID is composed of two identical parallel Josephson junctions forming a closed loop. A Josephson junction is the interruption of a superconducting line by a normal weak link. If the thickness of the link is small compared to the coherence length of the Cooper pairs present in the superconductor, the Cooper pairs tunnel through the link and the voltage across the Josephson junction is

$$V = R_J\sqrt{I^2 - I_c^2}, \tag{A.1}$$

where R_J is the Josephson junction resistance and I_c is the critical current of the junction [82].

Due to the quantization of the magnetic flux Φ in the SQUID, the superconducting current through the SQUID is

$$I = 2I_c cos\left(\frac{\pi\Phi}{\Phi_0}\right), \tag{A.2}$$

where $\Phi_0 = \frac{h}{2e}$ is the SQUID flux quanta [82]. Combining Equations A.1 and A.2, the voltage difference across the SQUID is

$$V = R_J I\sqrt{1 - \left[2\frac{I_c}{I}cos(\frac{\pi\Phi}{\Phi_0})\right]^2}. \tag{A.3}$$

This equation summarizes the operation of SQUIDs. Figure A–1 shows the modelled voltage response of a SQUID as a function of the flux bias ($V - \Phi$ curve) for various current biases. In practice, the two Josephson junctions are rarely identical and we neglected the self-inductance of the SQUID by assuming $LI_c \ll \Phi_0$ to derive Equation A.2. Those two factors contribute to a non-zero DC voltage response of the SQUID adding to the simulated response shown in Figure A–1 a). At a constant current bias I, the peak-to-peak response of a SQUID is

$$V^{PP} = \begin{cases} R_J I & I \leq 2I_c \\ R_J I\left[1 - \sqrt{1 - \left(\frac{2I_c}{I}\right)^2}\right] & I > 2I_c. \end{cases} \tag{A.4}$$

Figure A–1 b) shows the modelled peak-to-peak SQUID response as a function of the current bias ($V^{PP} - I_b$ curve). SQUIDs are typically biased with a current slightly greater than $2I_c$ and a flux bias maximizing the negative slope $\left|\frac{dV}{d\Phi}\right|$ to optimize the SQUID voltage response amplitude and linearity.

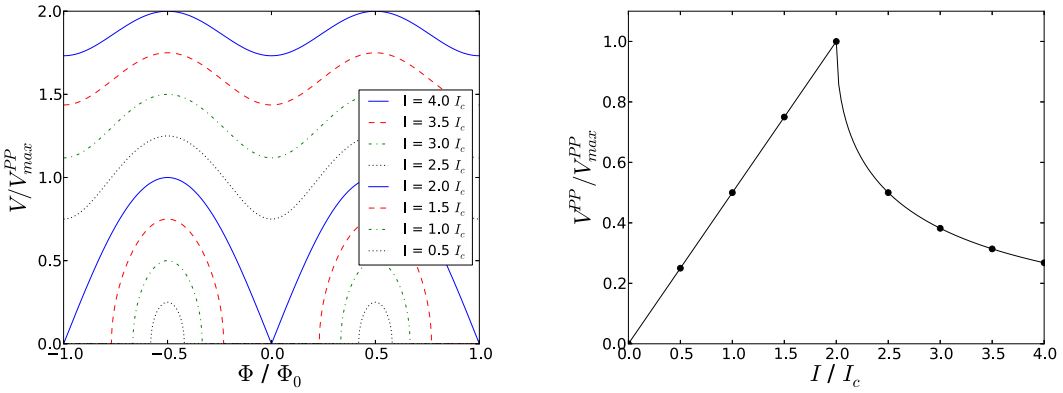

(a) (b)

Figure A–1: Figure a) shows the modelled voltage response of a SQUID as a function of the flux bias for eight different current biases. Figure b) shows the modelled peak-to-peak voltage response of a SQUID as a function of the applied current bias for the current biases shown in Figure a). The voltage response is normalized by the maximal voltage response $V_{max}^{PP} = 2I_cR_J$.

A.2 SQUIDs Operated in a Flux-Locked Loop

With frequency domain multiplexing, SQUIDs are operated in series with an operational amplifier in shunt feedback within a flux-locked loop (FLL) to increase their linearity and dynamic range. The schematic of the FLL circuit is shown in Figure A–2. The feedback resistor R_{FB} is selected to be 10, 5 or 3.3 $k\Omega$. To increase the stability of the SQUID, a lead-lag filter composed of R_{LL} and C_{LL} is implemented within the feedback loop. The SQUID impedance is modelled by the resistor R_{SQ}. The transfer function of the lead-lag filter is

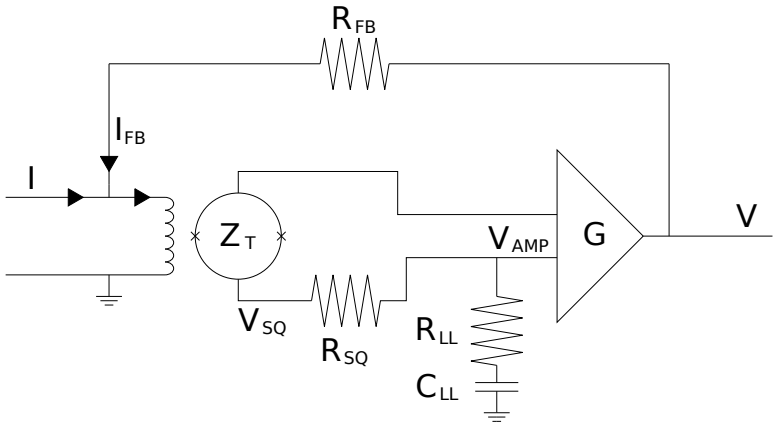

Figure A–2: Schematic of the electrical circuit used when operating a SQUID in series with an operational amplifier in shunt feedback within a flux-locked loop. A SQUID with trans-impedance Z_T is in series with an operational amplifier with gain G and a lead-lag filter composed of the resistor R_{LL} and the capacitor C_{LL}. The current through the feedback resistor R_{FB} nullifies the current through the SQUID coil. The SQUID impedance is R_{SQ}, the voltage at the SQUID output is V_{SQ} and the voltage at the amplifier input is V_{AMP}.

$$T_{LL}(f) \equiv \frac{V_{SQ}}{V_{AMP}} = \left| \frac{R_{SQ} + R_{LL} + \frac{1}{j\omega C_{LL}}}{R_{LL} + \frac{1}{j\omega C_{LL}}} \right|, \tag{A.5}$$

where V_{SQ} is the voltage at the SQUID output, V_{AMP} is the voltage at the amplifier input, R_{SQ} is 100 Ω, R_{LL} is 10 Ω and C is 1 nF. The output voltage of the FLL is

$$V = (I + I_{FB}) Z_T \left(\frac{G}{1 + j\omega\tau_G} \right) \left(\frac{R_{LL} + \frac{1}{j\omega C_{LL}}}{R_{SQ} + R_{LL} + \frac{1}{j\omega C_{LL}}} \right), \tag{A.6}$$

where I is the input current, I_{FB} is the current in the feedback loop, Z_T is the SQUID trans-impedance, G is the gain of the in-loop amplification and τ_G is the in-loop amplification time-constant. Substituting the feedback current $I_{FB} = \frac{V}{R_{FB}}$ and the trans-impedance $Z_T = \frac{dV}{dI} = M\frac{dV}{d\Phi}$ into the previous equation, the transfer function of the FLL becomes

$$\begin{aligned} \frac{V}{I} &= \frac{M\frac{dV}{d\Phi}\left(\frac{G}{1+j\omega\tau_G}\right)\left(\frac{1+j\omega\tau_1}{1+j\omega\tau_2}\right)}{1-\frac{1}{R_{FB}}M\frac{dV}{d\Phi}\left(\frac{G}{1+j\omega\tau_G}\right)\left(\frac{1+j\omega\tau_1}{1+j\omega\tau_2}\right)}, \\ &= R_{FB}\left(\frac{\mathcal{L}_{FLL}}{1-\mathcal{L}_{FLL}}\right), \end{aligned} \tag{A.7}$$

where $\tau_1 \equiv R_{LL}C_{LL}$ and $\tau_2 \equiv (R_{SQ}+R_{LL})C_{LL}$ are the time-constants of the lead-lag filter and the loop gain of the FLL is defined as $\mathcal{L}_{FLL} = \frac{M}{R_{FB}}\frac{dV}{d\Phi}\left(\frac{G}{1+j\omega\tau_G}\right)\left(\frac{1+j\omega\tau_1}{1+j\omega\tau_2}\right)$.

For EBEX, the mutual inductance M is $\frac{1\Phi_0}{26\mu A}$. The in-loop amplification is shown in Figure A–3 and is $G = \left(\frac{69800\Omega}{20\Omega}\right)\left(\frac{10\Omega}{121\Omega+10\Omega}\right) = 266$. The slope $\frac{dV}{d\Phi}$ is set by the operating point of the SQUID in Figure A–1 a) and can be approximated to $-\frac{4\pi}{\Phi_0}$ mV. Therefore, at low frequency, the FLL loop gain is minimally 13 when the feedback resistor is maximally set to 10 $k\Omega$ and the FLL transfer function is

$$\frac{V}{I} \approx R_{FB}. \tag{A.8}$$

A.3 Voltage Bias Transfer Function

The user input to the DfMUX boards to produce the voltage bias is a unit-less amplitude A_C, such that the maximal DAC output of 10 mA^{PP} is produced when the A_C from the N DfMUX channels (usually 16) are set to 1. The current produced is converted to a voltage by two 100 Ω resistors in parallel. The voltage bias is then amplified twice. One of the four resistors R_{GC} (2000, 820, 200 and 0 Ω corresponds to the carrier gains 0, 1, 2 and 3, respectively) can be selected to choose the gain of the second amplification. This allows for the optimization of the biasing dynamic range. The output voltage of the second stage of amplification is finally divided and bolometers are voltage biased by the 30 mΩ bias resistor. If the carrier frequency f_C is set to the reasonnant frequency of the RLC bolometer bandpass filter, the inductor and capacitor perfectly cancel out and V_b^{RMS} is the voltage across the bolometer. The detailed schematic of the voltage bias circuit is shown in Figure A–3. The transfer function is given by

$$\begin{aligned} V_b^{RMS} =& A_C \times \left(\frac{0.01A^{PP}}{N}\right) \times \left(\frac{1}{\frac{1}{50\Omega+50\Omega}+\frac{1}{100\Omega}}\right) \times \left(\frac{200\Omega}{200\Omega}+1\right) \times \\ & \left(\frac{1000\Omega}{(50+50+R_{GC})\Omega}\right) \times \left(\frac{\frac{1}{\frac{1}{200\Omega}+\frac{1}{50\Omega+50\Omega+50\Omega+50\Omega+0.03\Omega}}}{50\Omega+\frac{1}{\frac{1}{200\Omega}+\frac{1}{50\Omega+50\Omega+50\Omega+50\Omega+0.03\Omega}}+50\Omega}\right) \times \\ & \left(\frac{1}{50\Omega+50\Omega+50\Omega+50\Omega+0.03\Omega}\right) \times 0.03\Omega \times \frac{V^{RMS}}{2\sqrt{2}V^{PP}} \times \epsilon_C \\ =& A_C \frac{1.66\times10^{-3}}{(100+R_{GC})}\epsilon_C. \end{aligned} \tag{A.9}$$

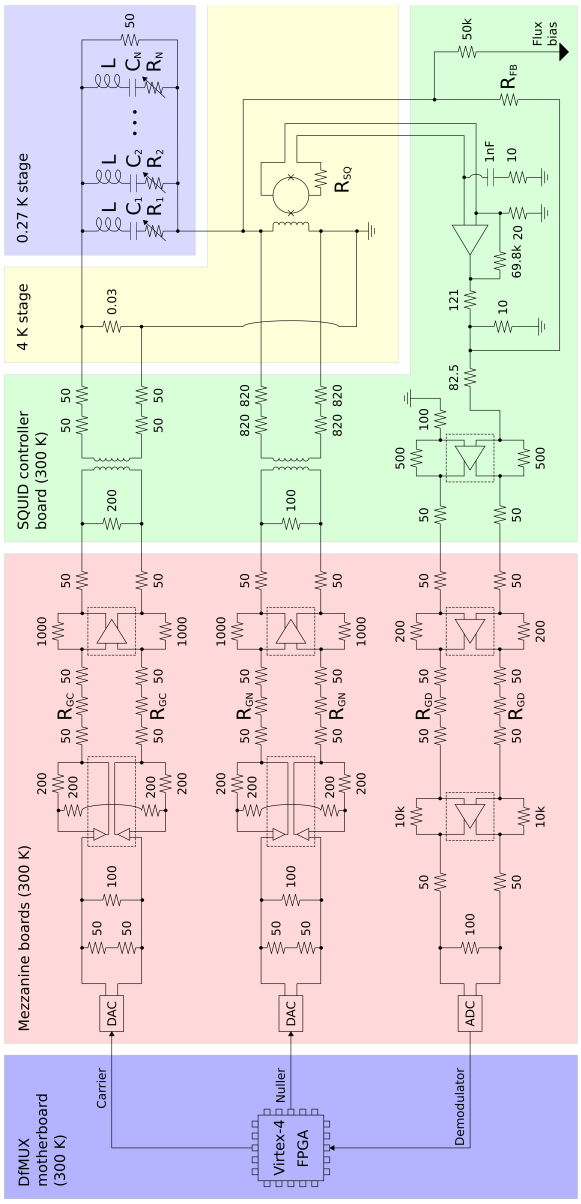

Figure A–3: Detailed schematic of the DfMUX readout system per board and temperature. The resistors R_{GC}, R_{GN} and R_{GD} can be selected to choose the different gains. The SQUID normal resistance is modelled by R_{SQ}. The SQUID feedback loop resistor is R_{FB}. The voltage bias bandpass selecting RLC filter are composed of the inductor L, the capacitor C_i and the bolometer resistance R_i.

An efficiency factor $\epsilon_C \equiv \frac{V_{b\ measured}^{RMS}}{V_{b\ theoretical}^{RMS}}$ is applied to correct for imperfections of the analog carrier circuit. This efficiency is measured only on the warm DfMUX electronics by an Agilent 4195a spectrum analyzer since a precise measurement involving the cold components of the circuitry is very challenging. The efficiency is 88.6% for carrier gains 0, 1 and 2 and 83.7% for carrier gain 3. The gain dependence of the efficiency is due to the stray resistance in the voltage bias gain selecting resistance circuitry. The effects of this few ohms stray resistance are only observable when the highest voltage bias gain is selected.

A.4 Nulling Current Transfer Function

The electronics providing the biasing voltages and the nulling currents present on the DfMUX boards are identical. The user input nulling current amplitude is A_N and the gain selecting resistors R_{GN} have the same values as for the voltage bias gain selecting resistors R_{GC}. On the SQUID controller board, the output voltage of the second stage of amplification of the nulling current is voltage divided and converted to a current through the SQUID coil by four 820 Ω resistors. The detailed schematic of the voltage bias circuit is shown in Figure A–3. The transfer function is given by

$$
\begin{aligned}
I_N^{RMS} =& A_N \times \left(\frac{0.01 A^{PP}}{N}\right) \times \left(\frac{1}{\frac{1}{50\Omega+50\Omega}+\frac{1}{100\Omega}}\right) \times \left(\frac{200\Omega}{200\Omega}+1\right) \times \\
& \left(\frac{1000\Omega}{(50+50+R_{GN})\Omega}\right) \times \left(\frac{\frac{1}{\frac{1}{100\Omega}+\frac{1}{4\times 820\Omega}}}{50\Omega+\frac{1}{\frac{1}{100\Omega}+\frac{1}{4\times 820\Omega}}+50\Omega}\right) \times \\
& \left(\frac{1}{4\times 820\Omega}\right) \times \frac{A^{RMS}}{2\sqrt{2}A^{PP}} \times \epsilon_N \\
=& A_N \frac{3.32\times 10^{-3}}{(100+R_{GN})}\epsilon_N. \qquad \text{(A.10)}
\end{aligned}
$$

An efficiency factor $\epsilon_N \equiv \frac{I_{N\ measured}^{RMS}}{I_{N\ theoretical}^{RMS}}$ is applied to correct for imperfections of the analog nulling current circuit. The nulling circuit is only wired to the SQUID coil in the cryostat, which considerably simplifies the characterization of the circuit. The output of the SQUID controller has been measured as a function of frequency and gain by an Agilent 4195a spectrum analyzer. The efficiency is

$$
\epsilon_N(f_N, G_N) = \frac{X_N(G_N)}{\sqrt{1+\left(\frac{f_N}{2.365\times 10^6}\right)^3}}, \qquad \text{(A.11)}
$$

where X_N is 94.9%, 93.9%, 93.1% and 89.5% when the nulling gain G_N is 0, 1, 2 and 3, respectively.

A.5 Demodulated Current Through the Bolometer Transfer Function

The current through the bolometers is amplified twice on the SQUID controller boards and twice on the DfMUX mezzanine boards. The first amplification is performed by a SQUID operated within a FLL with feedback resistor R_{FB}, as described

in Section A.2. The second stage amplification present on the SQUID controller board as well as the third and fourth amplification on the mezzanine boards are performed by simple amplifiers. One of the four resistors R_{GD} can be selected to choose the gain of the fourth amplification (10000, 2000, 200 and 0 Ω corresponds to the demodulator gains 0, 1, 2 and 3, respectively). The output voltage is then divided before it is digitized by a 14 bit ADC counts with a dynamic range of 2 V. The digital gain G_{dig} is finally applied and takes into account the demodulation normalisation and the gains of the different CIC and FIR filters. The digital gain is 1.9074 for a quasi-sine mixer and 2.0000 for a sinusoidal mixer.[1] Finally, the number of bits stored to disk is selected and the data are truncated. The truncation gain is

$$G_{trunc} = 2^{8-n_{trunc}}, \tag{A.12}$$

where n_{trunc} is the number of truncated bits. The number of truncated bits is typically 8 so G_{trunc}=1. The demodulated current recorded by the DfMUX electronics is I_{ADC}. The detailed schematic of the voltage bias circuit is shown in Figure A–3. The transfer function is given by

[1] The quasi-sine mixer has been used by EBEX during the NA flight and until December 2011. The sinusoidal mixer started to be used in preparation for the EBEX LDB flight.

$$
\begin{aligned}
I^P_{bolo} =& I_{ADC} \times \left(\frac{1}{G_{trunc}G_{dig}}\right) \times \left(\frac{2V}{2^{14}}\right) \times \left(\frac{50\Omega + 100\Omega + 50\Omega}{100\Omega}\right) \times \\
& \left(\frac{(50 + R_{GD} + 50)\Omega}{10000\Omega}\right) \times \left(\frac{50\Omega + 50\Omega + 50\Omega + 50\Omega}{200\Omega + 200\Omega}\right) \times \\
& \left(\frac{100\Omega + 82.5\Omega + \frac{1}{\frac{1}{10\Omega} + \frac{1}{121\Omega}}}{500\Omega + 500\Omega}\right) \times \left(\frac{1}{R_{FB}}\right) \times \frac{1}{\epsilon_D} \\
=& I_{ADC} \frac{2.34 \times 10^{-9}(100 + R_{GD})}{\epsilon_D R_{FB} G_{trunc} G_{dig}}
\end{aligned} \tag{A.13}
$$

An efficiency factor $\epsilon_D \equiv \frac{I^{RMS}_{bolo\ measured}}{I^{RMS}_{bolo\ theoretical}}$ is applied to correct for imperfections of the analog demodulation circuit. This efficiency is measured only on the warm Df-MUX electronics by an Agilent 4195a spectrum analyzer since a precise measurement of the cold components of the circuitry is nearly impossible. The efficiency is 88.6% for demodulation gains 0, 1 and 2 and 83.7% for demodulation gain 3. The gain dependence of the efficiency is due to the stray resistance in the demodulation gain selecting resistance circuitry. The effects of this few ohms stray resistance are only observable when the highest demodulator gain is selected.

The conversion from A^P to A^{RMS} depends on the demodulation frequency. The bolometer signal can be decomposed into the voltage bias frequency and its much smaller amplitude sidebands. The RMS of the sinusoidal voltage bias is simply $\sqrt{2}$ smaller than its peak amplitude because the bolometer cannot respond to the 25 MHz voltage bias. The sidebands represents the amplitude modulation of the voltage bias and their RMS and peak values are identical since they are much lower frequency than the bolometer response. The demodulation transfer function is therefore

$$I_{bolo}^{RMS}(f_D) = \begin{cases} I_{ADC}\frac{1.66\times10^{-9}(100+R_{GD})}{\epsilon_D R_{FB} G_{dig}} & , \ f_D = f_C \\ I_{ADC}\frac{2.34\times10^{-9}(100+R_{GD})}{\epsilon_D R_{FB} G_{dig}} & , \ f_D \neq f_C, \end{cases} \tag{A.14}$$

where f_D is the demodulation frequency.

Table A–1: The DfMUX readout transfer functions. A quasi-sine mixer and n_{trunc}=8 are assumed for the demodulator transfer functions.

Transfer function \ Gain		0	1	2	3
V_B^{RMS}/A_C	μV^{RMS}	0.700	1.60	4.90	13.9
$I_N^{RMS}(f_N = 500\ kHz)/A_N$	μA^{RMS}	1.49	3.37	10.4	29.6
$I_{bolo}^{RMS}(f_D = f_C, R_{FB} = 5\ k\Omega)/I_{ADC}$	pA^{RMS}	1980	411	58.8	20.7
$I_{bolo}^{RMS}(f_D \neq f_C, R_{FB} = 5\ k\Omega)/I_{ADC}$	pA^{RMS}	2800	582	83.1	29.3
$I_{bolo}^{RMS}(f_D = f_C, R_{FB} = 10\ k\Omega)/I_{ADC}$	pA^{RMS}	989	206	29.4	10.4
$I_{bolo}^{RMS}(f_D \neq f_C, R_{FB} = 10\ k\Omega)/I_{ADC}$	pA^{RMS}	1400	291	41.5	14.7

Table A–1 summarizes the different transfer functions. Because of the complexity of characterizing the cold temperature components in the cryostat, the nulling circuit has been more precisely characterized with its frequency dependence than the voltage biasing and the demodulation circuits. The uncertainty due to the cold components of the circuit are expected to dominate the uncertainty of the latter two transfer functions.

APPENDIX B
Bolometer Noise Predictions

This Appendix describes in detail the non-negligible noise components included in the bolometer noise predictions. The noise contributions are referred to current through the SQUID coil and the transfer functions converting the noise contribution at the source to current through the SQUID coil are described in Appendix A.

B.1 Warm Voltage Bias Sources of Noise

The electronics providing the voltage biases to the bolometers, commonly referred to as "carrier", have two amplifiers. The first stage amplifier produces $\frac{2.5nV}{\sqrt{Hz}}$ of noise and the second stage amplifier, $\frac{1.3nV}{\sqrt{Hz}}$. The current I_C through the SQUID coil produced by the voltage bias also produces the shot noise $\sqrt{2eI_C}$, where e is the elementary charge. The digitization noise of the voltage bias can be shown to be negligible as well as the Johnson noise of the other components. Table B–1 summarizes the noise sources related to the 300 K voltage bias electronics and presents those contributions referred to current through the SQUID coil.

B.2 Warm Nulling Current Sources of Noise

The electronics providing the nulling currents have two amplifiers. The first stage amplifier produces $\frac{2.5nV}{\sqrt{Hz}}$ and the second stage amplifier, $\frac{1.3nV}{\sqrt{Hz}}$. The current I_N through the SQUID coil suffers from the shot noise $\sqrt{2eI_N}$. The four 820 Ω resistors converting the nulling voltage into current through the SQUID coil also produce the current Johnson noise $\sqrt{\frac{4kT_{300K}}{4\times R_{820\Omega}}}$. The digitization noise of the nulling current can be

Table B–1: Un-demodulated 300 K voltage bias electronics noise contributions.

Noise source	Noise referred to the source	Noise referred to the SQUID coil $\frac{pA}{\sqrt{Hz}}$
$i_{n\ 1^{st}\ C}$	$2.5\ \frac{nV}{\sqrt{Hz}}$	$\frac{375}{(100+R_{GC})R_{bolo}}$
$i_{n\ 2^{nd}\ C}$	$1.3\ \frac{nV}{\sqrt{Hz}}$	$\frac{97.5}{(100+R_{GC})R_{bolo}}$
$i_{n\ SN\ C}$	$\sqrt{2eI_{C\ DAC}}$	$23.0\sqrt{\frac{A_C}{(100+R_{GC})R_{bolo}}}$

shown to be negligible as well as the Johnson noise of the other components. Table B–2 summarizes the noise sources related to the 300 K nulling current electronics and shows those contributions referred to current through the SQUID coil.

Table B–2: Un-demodulated 300 K nulling current electronics noise contributions.

Noise source	Noise referred to the source	Noise referred to the SQUID coil $\frac{pA}{\sqrt{Hz}}$
$i_{n\ 1^{st}\ N}$	$2.5\ \frac{nV}{\sqrt{Hz}}$	$\frac{751}{(100+R_{GN})}$
$i_{n\ 2^{nd}\ N}$	$1.3\ \frac{nV}{\sqrt{Hz}}$	$\frac{195}{(100+R_{GN})}$
$i_{n\ 4\times820\Omega}$	$\sqrt{\frac{4kT_{300K}}{4\times R_{820\Omega}}}$	2.2
$i_{n\ SN\ N}$	$\sqrt{2eI_{N\ DAC}}$	$32.6\sqrt{\frac{A_N}{(100+R_{GN})}}$

B.3 Warm Demodulation Sources of Noise

The first stage amplifier on the SQUID controller board produces $0.85\frac{nV}{\sqrt{Hz}}$ of noise, its 20 Ω gain defining resistor produces the voltage Johnson noise $\sqrt{4kT_{300K}R_{20\Omega}}$ and the FLL feedback resistor produces the current Johnson noise $\sqrt{\frac{4kT_{300K}}{R_{FB}}}$. The second stage amplifier on the SQUID controller board produces $1.3\frac{nV}{\sqrt{Hz}}$ of noise. The 50 kΩ resistor providing the flux bias to the SQUID produces the current Johnson

noise $\sqrt{\frac{4kT_{300K}}{R_{50k\Omega}}}$. The demodulating electronics present on the DfMUX mezzanine boards have two amplifiers, both producing $\frac{1.3nV}{\sqrt{Hz}}$ of noise, which can be shown to have negligible noise contributions. The 25 MHz digitization of the demodulated current generates the noise $\frac{1\ LSB}{\sqrt{12\times12.5MHz}}$. The digital processing of the demodulated signal produces the truncation noise $\frac{1\ LSB}{\sqrt{12\times\frac{f_s}{2}}}$, where f_s is the output sampling frequency of the DfMUX board (f_s=190.7 Hz for EBEX). The other components of the 300 K demodulation circuit can be shown to be negligible. Table B–3 summarizes the noise sources related to the 300 K demodulation electronics and shows those contributions referred to current through the SQUID coil.

Table B–3: Un-demodulated 300 K demodulation electronics noise contributions.

Noise source	Noise referred to the source	Noise referred to the SQUID coil $\frac{pA}{\sqrt{Hz}}$
$i_{n\ 1^{st}\ SQctrl}$	$0.85\ \frac{nV}{\sqrt{Hz}}$	$\frac{850T_{LL}(f)}{Z_T}$
$i_{n\ 20\Omega}$	$\sqrt{\frac{4kT}{R_{20\Omega}}}$	$\frac{575T_{LL}(f)}{Z_T}$
$i_{n\ R_{FB}}$	$\sqrt{\frac{4kT}{R_{RB}}}$	$\frac{4.069}{\sqrt{R_{FB}[k\Omega]}}$
$i_{n\ 2^{nd}\ SQctrl}$	$1.3\ \frac{nV}{\sqrt{Hz}}$	$\frac{1.3\times10^{-3}}{R_{FB}}$
$i_{n\ 50k\Omega}$	$\sqrt{\frac{4kT}{R_{50k\Omega}}}$	0.58
$i_{n\ digit\ D}$	$\frac{1\ LSB}{\sqrt{12\times12.5MHz}}$	$\frac{191(100+R_{GD})}{R_{FB}}$
$i_{n\ trunc\ D}$	$\frac{1\ LSB}{\sqrt{12\times\frac{f_s}{2}}}$	$\frac{956(100+R_{GD})}{G_{trunc}G_{dig}\sqrt{f_{samp}}R_{FB}}$

B.4 Cold Readout Sources of Noise

The SQUIDs have been empirically found to produce 3.5 $\frac{pA}{\sqrt{Hz}}$ of noise. The 30 mΩ bias resistor produces the voltage Johnson noise $\sqrt{4KT_{4.2K}R_{0.03\Omega}}$. The 50 Ω bolometer termination resistor produces the current Johnson noise $\sqrt{\frac{4KT_{0.27K}}{R_{50}}}$.

Table B–4 summarizes the noise sources related to the 4 K and the sub-kelvin readout components and shows those contributions referred to current through the SQUID coil.

Table B–4: Un-demodulated cold readout noise predictions.

Noise source	Noise referred to the source	Noise referred to the SQUID coil $\frac{pA}{\sqrt{Hz}}$
$i_{n\ SQ}$	$3.5\ \frac{pA}{\sqrt{Hz}}$	3.5
$i_{n\ 30m\Omega}$	$\sqrt{4KT_{4.2K}R_{bias}}$	$\frac{2.64}{R_{bolo}}$
$i_{n\ 30m\Omega}$	$\sqrt{\frac{4KT_{0.27K}}{R_{50\Omega}}}$	0.55

B.5 Bolometer Sources of Noise

Bolometers produce the current Johnson noise $\sqrt{\frac{4kT_{bolo}}{R_{bolo}}}$. When the bolometer is into its superconducting transition, the Johnson noise is suppressed and the power phonon noise $\sqrt{\gamma 4kT_{bolo}^2 G}$ is also produced [51]. When the bolometers absorb photons, the Poisson statistics power noise $\sqrt{2h\nu P_{rad}}$ and the correlation power noise $\sqrt{\xi \frac{P_{rad}^2}{\Delta\nu}}$ are produced. These sources of noise are discussed in details in Section 4.5.2. Table B–5 summarizes the bolometer noise contributions referred to current through the SQUID coil.

B.6 Noise Contributions for Different Receiver Configurations

The noise predictions of five receiver configurations are commonly required. The noise sources from the demodulation chain are always present when measuring noise as well as the noise produced by the two nulling current amplifiers, the four 820 Ω resistors and the 50 Ω bolometer termination resistor. In particular, this statement

Table B–5: Un-demodulated bolometer noise predictions.

Noise source	Noise referred to the source	Noise referred to the SQUID coil $\frac{pA}{\sqrt{Hz}}$
$i_{n\ Johnson}$	$\sqrt{\frac{4kT_{bolo}}{R_{bolo}}}$	$\sqrt{\frac{4kT_{bolo}}{R_{bolo}}}$
$i_{n\ phonon}$	$\sqrt{\gamma 4kT_{bolo}^2 G}$	$S_I\sqrt{\gamma 4kT_{bolo}^2 G}$
$i_{n\ \gamma\ Pois}$	$\sqrt{2h\nu P_{rad}}$	$S_I\sqrt{2h\nu P_{rad}}$
$i_{n\ \gamma\ corr}$	$\sqrt{\xi\frac{P_{rad}^2}{\Delta\nu}}$	$S_I\sqrt{\xi\frac{P_{rad}^2}{\Delta\nu}}$

is true for dark SQUIDs and SQUIDs demodulated with frequencies outside the bolometer bandpass filters. When the demodulating frequency is set to a bolometer biasing frequency while the bolometer is not provided a voltage bias, the two carrier amplifiers, the bias resistor and the bolometer Johnson noise are present. When a voltage bias is provided to the bolometers, all the voltage bias and the nulling current sources of noise become present. Phonon noise adds when the bolometer is dropped into its superconducting transition and no photons are absorbed by the bolometers. When the bolometers absorb light, photon noise also contributes to the noise performance of the system. Table B–6 summarizes the sources of noise present for the five configurations described.

In order to compare the noise predictions derived in this section with data demodulated by the DfMUX readout system, the demodulating factor described in Section 4.5.2 must be applied.

Table B–6: Noise sources contributing to the measured noise performance for the different bolometer and readout configurations.

Source	Dark SQUID	SQUID bolo attached $f_D = f_C$	Bolo biased above its transition	Dark bolo in transition	Light bolo in transition
$i_{n\ 1^{st}\ C}$		X	X	X	X
$i_{n\ 2^{nd}\ C}$		X	X	X	X
$i_{n\ SN\ C}$			X	X	X
$i_{n\ 1^{st}\ N}$	X	X	X	X	X
$i_{n\ 2^{nd}\ N}$	X	X	X	X	X
$i_{n\ 4\times820\Omega}$	X	X	X	X	X
$i_{n\ SN\ N}$			X	X	X
$i_{n\ 1^{st}\ SQctrl}$	X	X	X	X	X
$i_{n\ 20\Omega}$	X	X	X	X	X
$i_{n\ R_{FB}}$	X	X	X	X	X
$i_{n\ 2^{nd}\ SQctrl}$	X	X	X	X	X
$i_{n\ 50k\Omega}$	X	X	X	X	X
$i_{n\ digit\ D}$	X	X	X	X	X
$i_{n\ trunc\ D}$	X	X	X	X	X
$i_{n\ SQ}$	X	X	X	X	X
$i_{n\ 30m\Omega}$		X	X	X	X
$i_{n\ 50\Omega}$	X	X	X	X	X
$i_{n\ Johnson}$		X	X	X	X
$i_{n\ phonon}$				X	X
$i_{n\ \gamma\ Pois}$					X
$i_{n\ \gamma\ corr}$					X

APPENDIX C
DfMUX Voltage Performance During the NAF

Figure C–1 shows the power voltages supplied and regulated for a representative DfMUX board (011) during the NA flight. Small variations are seen across the supplied voltages to this boards during flight. The raw +10 V is more noisy while the fans inside the BRO crates are activated to convectively cool the boards since this power line is also used by the fans. The fans were designed to be powered off during ascent and the power performance of the fans has not been optimized for noise since they cannot be used at float. The voltages variation being small, the power provided to the DfMUX boards are concluded to be nominal.

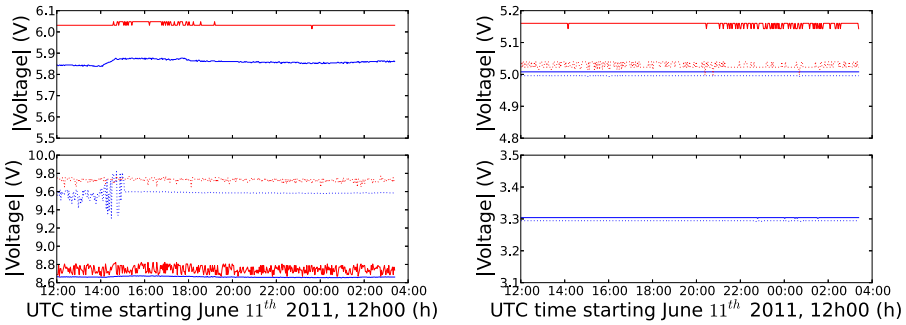

(a) (b)

Figure C–1: The top panel of Figure a) shows the ± 6 V voltages and the bottom panel, the ± 10 V voltages powering the representative DfMUX board 011 during the NA flight. The solid lines show the regulated voltages and the dotted lines show the raw supplied voltages to the DfMUX. The top panel of Figure b) shows the ± 5 V regulated voltages and the bottom panel, the +3 V regulated voltages for mezzanines #1 (solid) and #2 (dotted) of DfMUX 011. In both figures, the blue curves show positive voltages and the red curves show the absolute value of the negative voltages.

References

[1] A. A. Penzias and R. W. Wilson. A Measurement of Excess Antenna Temperature at 4080 Mc/s. *Astrophysical Journal*, 142:419–421, July 1965.

[2] J. M. Kovac, E. M. Leitch, C. Pryke, J. E. Carlstrom, N. W. Halverson, and W. L. Holzapfel. Detection of polarization in the cosmic microwave background using DASI. *Nature*, 420:772–787, December 2002.

[3] J.-M. Lamarre, J.-L. Puget, P. A. R. Ade, F. Bouchet, G. Guyot, A. E. Lange, F. Pajot, A. Arondel, K. Benabed, J.-L. Beney, A. Benoît, J.-P. Bernard, R. Bhatia, Y. Blanc, J. J. Bock, E. Bréelle, T. W. Bradshaw, P. Camus, A. Catalano, J. Charra, M. Charra, S. E. Church, F. Couchot, A. Coulais, B. P. Crill, M. R. Crook, K. Dassas, P. de Bernardis, J. Delabrouille, P. de Marcillac, J.-M. Delouis, F.-X. Désert, C. Dumesnil, X. Dupac, G. Efstathiou, P. Eng, C. Evesque, J.-J. Fourmond, K. Ganga, M. Giard, R. Gispert, L. Guglielmi, J. Haissinski, S. Henrot-Versillé, E. Hivon, W. A. Holmes, W. C. Jones, T. C. Koch, H. Lagardère, P. Lami, J. Landé, B. Leriche, C. Leroy, Y. Longval, J. F. Macías-Pérez, T. Maciaszek, B. Maffei, B. Mansoux, C. Marty, S. Masi, C. Mercier, M.-A. Miville-Deschênes, A. Moneti, L. Montier, J. A. Murphy, J. Narbonne, M. Nexon, C. G. Paine, J. Pahn, O. Perdereau, F. Piacentini, M. Piat, S. Plaszczynski, E. Pointecouteau, R. Pons, N. Ponthieu, S. Prunet, D. Rambaud, G. Recouvreur, C. Renault, I. Ristorcelli, C. Rosset, D. Santos, G. Savini, G. Serra, P. Stassi, R. V. Sudiwala, J.-F. Sygnet, J. A. Tauber, J.-P. Torre, M. Tristram, L. Vibert, A. Woodcraft, V. Yurchenko, and D. Yvon. Planck pre-launch status: The HFI instrument, from specification to actual performance. *Astronomy and Astrophysics*, 520:A9, September 2010.

[4] J. C. Mather, D. J. Fixsen, R. A. Shafer, C. Mosier, and D. T. Wilkinson. Calibrator Design for the COBE Far-Infrared Absolute Spectrophotometer (FIRAS). *apj*, 512:511–520, February 1999.

[5] C. L. Bennett, M. Bay, M. Halpern, G. Hinshaw, C. Jackson, N. Jarosik, A. Kogut, M. Limon, S. S. Meyer, L. Page, D. N. Spergel, G. S. Tucker, D. T.

Wilkinson, E. Wollack, and E. L. Wright. The Microwave Anisotropy Probe Mission. *Astrophysical Journal*, 583:1–23, January 2003.

[6] C. L. Reichardt, P. A. R. Ade, J. J. Bock, J. R. Bond, J. A. Brevik, C. R. Contaldi, M. D. Daub, J. T. Dempsey, J. H. Goldstein, W. L. Holzapfel, C. L. Kuo, A. E. Lange, M. Lueker, M. Newcomb, J. B. Peterson, J. Ruhl, M. C. Runyan, and Z. Staniszewski. High-Resolution CMB Power Spectrum from the Complete ACBAR Data Set. *Astrophysical Journal*, 694:1200–1219, April 2009.

[7] M. L. Brown, P. Ade, J. Bock, M. Bowden, G. Cahill, P. G. Castro, S. Church, T. Culverhouse, R. B. Friedman, K. Ganga, W. K. Gear, S. Gupta, J. Hinderks, J. Kovac, A. E. Lange, E. Leitch, S. J. Melhuish, Y. Memari, J. A. Murphy, A. Orlando, C. O'Sullivan, L. Piccirillo, C. Pryke, N. Rajguru, B. Rusholme, R. Schwarz, A. N. Taylor, K. L. Thompson, A. H. Turner, E. Y. S. Wu, M. Zemcov, and QUa D Collaboration. Improved Measurements of the Temperature and Polarization of the Cosmic Microwave Background from QUaD. *Astrophysical Journal*, 705:978–999, November 2009.

[8] N. Jarosik, C. L. Bennett, J. Dunkley, B. Gold, M. R. Greason, M. Halpern, R. S. Hill, G. Hinshaw, A. Kogut, E. Komatsu, D. Larson, M. Limon, S. S. Meyer, M. R. Nolta, N. Odegard, L. Page, K. M. Smith, D. N. Spergel, G. S. Tucker, J. L. Weiland, E. Wollack, and E. L. Wright. Seven-year Wilkinson Microwave Anisotropy Probe (WMAP) Observations: Sky Maps, Systematic Errors, and Basic Results. *Astrophysical Journal, Supplement*, 192:14, February 2011.

[9] E. Komatsu, K. M. Smith, J. Dunkley, C. L. Bennett, B. Gold, G. Hinshaw, N. Jarosik, D. Larson, M. R. Nolta, L. Page, D. N. Spergel, M. Halpern, R. S. Hill, A. Kogut, M. Limon, S. S. Meyer, N. Odegard, G. S. Tucker, J. L. Weiland, E. Wollack, and E. L. Wright. Seven-year Wilkinson Microwave Anisotropy Probe (WMAP) Observations: Cosmological Interpretation. *Astrophysical Journal, Supplement*, 192:18, February 2011.

[10] M. Lueker, C. L. Reichardt, K. K. Schaffer, O. Zahn, P. A. R. Ade, K. A. Aird, B. A. Benson, L. E. Bleem, J. E. Carlstrom, C. L. Chang, H.-M. Cho, T. M. Crawford, A. T. Crites, T. de Haan, M. A. Dobbs, E. M. George, N. R. Hall, N. W. Halverson, G. P. Holder, W. L. Holzapfel, J. D. Hrubes, M. Joy, R. Keisler, L. Knox, A. T. Lee, E. M. Leitch, J. J. McMahon, J. Mehl, S. S. Meyer, J. J. Mohr, T. E. Montroy, S. Padin, T. Plagge, C. Pryke, J. E. Ruhl, L. Shaw, E. Shirokoff, H. G. Spieler, B. Stalder, Z. Staniszewski, A. A. Stark,

K. Vanderlinde, J. D. Vieira, and R. Williamson. Measurements of Secondary Cosmic Microwave Background Anisotropies with the South Pole Telescope. *Astrophysical Journal*, 719:1045–1066, August 2010.

[11] A. C. S. Readhead, B. S. Mason, C. R. Contaldi, T. J. Pearson, J. R. Bond, S. T. Myers, S. Padin, J. L. Sievers, J. K. Cartwright, M. C. Shepherd, D. Pogosyan, S. Prunet, P. Altamirano, R. Bustos, L. Bronfman, S. Casassus, W. L. Holzapfel, J. May, U.-L. Pen, S. Torres, and P. S. Udomprasert. Extended Mosaic Observations with the Cosmic Background Imager. *Astrophysical Journal*, 609:498–512, July 2004.

[12] C. Dickinson, R. A. Battye, P. Carreira, K. Cleary, R. D. Davies, R. J. Davis, R. Genova-Santos, K. Grainge, C. M. Gutiérrez, Y. A. Hafez, M. P. Hobson, M. E. Jones, R. Kneissl, K. Lancaster, A. Lasenby, J. P. Leahy, K. Maisinger, C. Ödman, G. Pooley, N. Rajguru, R. Rebolo, J. A. Rubiño-Martin, R. D. E. Saunders, R. S. Savage, A. Scaife, P. F. Scott, A. Slosar, P. Sosa Molina, A. C. Taylor, D. Titterington, E. Waldram, R. A. Watson, and A. Wilkinson. High-sensitivity measurements of the cosmic microwave background power spectrum with the extended Very Small Array. *Monthly Notices of the RAS*, 353:732–746, September 2004.

[13] W. C. Jones, P. A. R. Ade, J. J. Bock, J. R. Bond, J. Borrill, A. Boscaleri, P. Cabella, C. R. Contaldi, B. P. Crill, P. de Bernardis, G. De Gasperis, A. de Oliveira-Costa, G. De Troia, G. di Stefano, E. Hivon, A. H. Jaffe, T. S. Kisner, A. E. Lange, C. J. MacTavish, S. Masi, P. D. Mauskopf, A. Melchiorri, T. E. Montroy, P. Natoli, C. B. Netterfield, E. Pascale, F. Piacentini, D. Pogosyan, G. Polenta, S. Prunet, S. Ricciardi, G. Romeo, J. E. Ruhl, P. Santini, M. Tegmark, M. Veneziani, and N. Vittorio. A Measurement of the Angular Power Spectrum of the CMB Temperature Anisotropy from the 2003 Flight of BOOMERANG. *Astrophysical Journal*, 647:823–832, August 2006.

[14] H. C. Ohanian and R. Ruffini. *Gravitation and Spacetime*. W. W. Norton & Company Ltd., 10 Coptic Street, London, WCA1 1PU, 1994.

[15] D. Baumann, M. G. Jackson, P. Adshead, A. Amblard, A. Ashoorioon, N. Bartolo, R. Bean, M. Beltrán, F. de Bernardis, S. Bird, X. Chen, D. J. H. Chung, L. Colombo, A. Cooray, P. Creminelli, S. Dodelson, J. Dunkley, C. Dvorkin, R. Easther, F. Finelli, R. Flauger, M. P. Hertzberg, K. Jones-Smith, S. Kachru, K. Kadota, J. Khoury, W. H. Kinney, E. Komatsu, L. M. Krauss, J. Lesgourgues, A. Liddle, M. Liguori, E. Lim, A. Linde, S. Matarrese, H. Mathur,

L. McAllister, A. Melchiorri, A. Nicolis, L. Pagano, H. V. Peiris, M. Peloso, L. Pogosian, E. Pierpaoli, A. Riotto, U. Seljak, L. Senatore, S. Shandera, E. Silverstein, T. Smith, P. Vaudrevange, L. Verde, B. Wandelt, D. Wands, S. Watson, M. Wyman, A. Yadav, W. Valkenburg, and M. Zaldarriaga. Probing Inflation with CMB Polarization. In S. Dodelson, D. Baumann, A. Cooray, J. Dunkley, A. Fraisse, M. G. Jackson, A. Kogut, L. Krauss, M. Zaldarriaga, and K. Smith, editors, *American Institute of Physics Conference Series*, volume 1141 of *American Institute of Physics Conference Series*, pages 10–120, June 2009.

[16] A. D. Linde. A new inflationary universe scenario: A possible solution of the horizon, flatness, homogeneity, isotropy and primordial monopole problems. *Physics Letters B*, 108:389–393, February 1982.

[17] A. Kosowsky and M. S. Turner. CBR anisotropy and the running of the scalar spectral index. *Physical Review D*, 52:1739, August 1995.

[18] S. M. Leach, A. R. Liddle, J. Martin, and D. J. Schwarz. Cosmological parameter estimation and the inflationary cosmology. *Physical Review D*, 66(2):023515, July 2002.

[19] A. Cooray. Primordial Gravitational Waves and Inflation:. *Modern Physics Letters A*, 20:2503–2519, 2005.

[20] W. Hu and M. White. A CMB polarization primer. *New Astronomy*, 2:323–344, October 1997.

[21] A. C. S. Readhead, S. T. Myers, T. J. Pearson, J. L. Sievers, B. S. Mason, C. R. Contaldi, J. R. Bond, R. Bustos, P. Altamirano, C. Achermann, L. Bronfman, J. E. Carlstrom, J. K. Cartwright, S. Casassus, C. Dickinson, W. L. Holzapfel, J. M. Kovac, E. M. Leitch, J. May, S. Padin, D. Pogosyan, M. Pospieszalski, C. Pryke, R. Reeves, M. C. Shepherd, and S. Torres. Polarization Observations with the Cosmic Background Imager. *Science*, 306:836–844, October 2004.

[22] T. E. Montroy, P. A. R. Ade, J. J. Bock, J. R. Bond, J. Borrill, A. Boscaleri, P. Cabella, C. R. Contaldi, B. P. Crill, P. de Bernardis, G. De Gasperis, A. de Oliveira-Costa, G. De Troia, G. di Stefano, E. Hivon, A. H. Jaffe, T. S. Kisner, W. C. Jones, A. E. Lange, S. Masi, P. D. Mauskopf, C. J. MacTavish, A. Melchiorri, P. Natoli, C. B. Netterfield, E. Pascale, F. Piacentini, D. Pogosyan, G. Polenta, S. Prunet, S. Ricciardi, G. Romeo, J. E. Ruhl, P. Santini, M. Tegmark, M. Veneziani, and N. Vittorio. A Measurement of the CMB

<EE> Spectrum from the 2003 Flight of BOOMERANG. *Astrophysical Journal*, 647:813–822, August 2006.

[23] C. Bischoff, L. Hyatt, J. J. McMahon, G. W. Nixon, D. Samtleben, K. M. Smith, K. Vanderlinde, D. Barkats, P. Farese, T. Gaier, J. O. Gundersen, M. M. Hedman, S. T. Staggs, B. Winstein, and CAPMAP Collaboration. New Measurements of Fine-Scale CMB Polarization Power Spectra from CAPMAP at Both 40 and 90 GHz. *Astrophysical Journal*, 684:771–789, September 2008.

[24] B. R. Johnson, J. Collins, M. E. Abroe, P. A. R. Ade, J. Bock, J. Borrill, A. Boscaleri, P. de Bernardis, S. Hanany, A. H. Jaffe, T. Jones, A. T. Lee, L. Levinson, T. Matsumura, B. Rabii, T. Renbarger, P. L. Richards, G. F. Smoot, R. Stompor, H. T. Tran, C. D. Winant, J. H. P. Wu, and J. Zuntz. MAXIPOL: Cosmic Microwave Background Polarimetry Using a Rotating Half-Wave Plate. *Astrophysical Journal*, 665:42–54, August 2007.

[25] H. C. Chiang, P. A. R. Ade, D. Barkats, J. O. Battle, E. M. Bierman, J. J. Bock, C. D. Dowell, L. Duband, E. F. Hivon, W. L. Holzapfel, V. V. Hristov, W. C. Jones, B. G. Keating, J. M. Kovac, C. L. Kuo, A. E. Lange, E. M. Leitch, P. V. Mason, T. Matsumura, H. T. Nguyen, N. Ponthieu, C. Pryke, S. Richter, G. Rocha, C. Sheehy, Y. D. Takahashi, J. E. Tolan, and K. W. Yoon. Measurement of Cosmic Microwave Background Polarization Power Spectra from Two Years of BICEP Data. *Astrophysical Journal*, 711:1123–1140, March 2010.

[26] D. Larson, J. Dunkley, G. Hinshaw, E. Komatsu, M. R. Nolta, C. L. Bennett, B. Gold, M. Halpern, R. S. Hill, N. Jarosik, A. Kogut, M. Limon, S. S. Meyer, N. Odegard, L. Page, K. M. Smith, D. N. Spergel, G. S. Tucker, J. L. Weiland, E. Wollack, and E. L. Wright. Seven-year Wilkinson Microwave Anisotropy Probe (WMAP) Observations: Power Spectra and WMAP-derived Parameters. *Astrophysical Journal, Supplement*, 192:16, February 2011.

[27] B. Gold, N. Odegard, J. L. Weiland, R. S. Hill, A. Kogut, C. L. Bennett, G. Hinshaw, X. Chen, J. Dunkley, M. Halpern, N. Jarosik, E. Komatsu, D. Larson, M. Limon, S. S. Meyer, M. R. Nolta, L. Page, K. M. Smith, D. N. Spergel, G. S. Tucker, E. Wollack, and E. L. Wright. Seven-year Wilkinson Microwave Anisotropy Probe (WMAP) Observations: Galactic Foreground Emission. *Astrophysical Journal, Supplement*, 192:15, February 2011.

[28] M. Zaldarriaga and U. Seljak. Gravitational lensing effect on cosmic microwave background polarization. *Physical Review D*, 58(2):023003, July 1998.

[29] R. Keisler, C. L. Reichardt, K. A. Aird, B. A. Benson, L. E. Bleem, J. E. Carlstrom, C. L. Chang, H. M. Cho, T. M. Crawford, A. T. Crites, T. de Haan, M. A. Dobbs, J. Dudley, E. M. George, N. W. Halverson, G. P. Holder, W. L. Holzapfel, S. Hoover, Z. Hou, J. D. Hrubes, M. Joy, L. Knox, A. T. Lee, E. M. Leitch, M. Lueker, D. Luong-Van, J. J. McMahon, J. Mehl, S. S. Meyer, M. Millea, J. J. Mohr, T. E. Montroy, T. Natoli, S. Padin, T. Plagge, C. Pryke, J. E. Ruhl, K. K. Schaffer, L. Shaw, E. Shirokoff, H. G. Spieler, Z. Staniszewski, A. A. Stark, K. Story, A. van Engelen, K. Vanderlinde, J. D. Vieira, R. Williamson, and O. Zahn. A Measurement of the Damping Tail of the Cosmic Microwave Background Power Spectrum with the South Pole Telescope. *Astrophysical Journal*, 743:28, December 2011.

[30] J. Hubmayr. *Bolometric detectors for EBEX: A balloon-borne cosmic microwave background polarimeter*. PhD thesis, University of Minnesota, 2009.

[31] N. Schneider, J. Urban, and P. Baron. Potential of radiotelescopes for atmospheric line observations: I. Observation principles and transmission curves for selected sites. *Planetary Space Science*, 57:1419–1433, October 2009.

[32] E. Pascale, P. A. R. Ade, J. J. Bock, E. L. Chapin, J. Chung, M. J. Devlin, S. Dicker, M. Griffin, J. O. Gundersen, M. Halpern, P. C. Hargrave, D. H. Hughes, J. Klein, C. J. MacTavish, G. Marsden, P. G. Martin, T. G. Martin, P. Mauskopf, C. B. Netterfield, L. Olmi, G. Patanchon, M. Rex, D. Scott, C. Semisch, N. Thomas, M. D. P. Truch, C. Tucker, G. S. Tucker, M. P. Viero, and D. V. Wiebe. The Balloon-borne Large Aperture Submillimeter Telescope: BLAST. *Astrophysical Journal*, 681:400–414, July 2008.

[33] M. Milligan, P. Ade, F. Aubin, C. Baccigalupi, C. Bao, J. Borrill, C. Cantalupo, D. Chapman, J. Didier, M. Dobbs, W. Grainger, S. Hanany, S. Hillbrand, J. Hubmayr, P. Hyland, A. Jaffe, B. Johnson, T. Kisner, J. Klein, A. Korotkov, S. Leach, A. Lee, L. Levinson, M. Limon, K. MacDermid, T. Matsumura, A. Miller, E. Pascale, D. Polsgrove, N. Ponthieu, K. Raach, B. Reichborn-Kjennerud, I. Sagiv, H. Tran, G. S. Tucker, Y. Vinokurov, A. Yadav, M. Zaldarriaga, and K. Zilic. Software systems for operation, control, and monitoring of the EBEX instrument. In *Society of Photo-Optical Instrumentation Engineers (SPIE) Conference Series*, volume 7740 of *Society of Photo-Optical Instrumentation Engineers (SPIE) Conference Series*, July 2010.

[34] W. Stallings. *Data and Computer Communications (7^{th} ed.)*. Prentice Hall, 2004.

[35] NOAA. The world magnetic model. *http://www.ngdc.noaa.gov/geomag/WMM/soft.shtml*, 2012.

[36] B. Reichborn-Kjennerud. *Building and flying the E and B Experiment to measure the polarization of the cosmic microwave background*. PhD thesis, Columbia University, 2010.

[37] I. Sagiv, A. M. Aboobaker, C. Bao, S. Hanany, T. Jones, J. Klein, M. Milligan, D. E. Polsgrove, K. Raach, K. Zilic, A. Korotkov, G. S. Tucker, Y. Vinokurov, T. Matsumara, P. Ade, W. Grainger, E. Pascale, D. Chapman, J. Didier, S. Hillbrand, B. Reichborn-Kjennerud, M. Limon, A. Miller, A. Jaffe, A. Yadav, M. Zaldarriaga, N. Ponthieu, M. Tristram, J. Borrill, C. Cantalupo, T. Kisner, F. Aubin, M. Dobbs, and K. MacDermid. The EBEX Cryostat and Supporting Electronics. In *Twelfth Marcel Grossmann Meeting on General Relativity*, page 2166, 2012.

[38] B. Reichborn-Kjennerud, A. M. Aboobaker, P. Ade, F. Aubin, C. Baccigalupi, C. Bao, J. Borrill, C. Cantalupo, D. Chapman, J. Didier, M. Dobbs, J. Grain, W. Grainger, S. Hanany, S. Hillbrand, J. Hubmayr, A. Jaffe, B. Johnson, T. Jones, T. Kisner, J. Klein, A. Korotkov, S. Leach, A. Lee, L. Levinson, M. Limon, K. MacDermid, T. Matsumura, X. Meng, A. Miller, M. Milligan, E. Pascale, D. Polsgrove, N. Ponthieu, K. Raach, I. Sagiv, G. Smecher, F. Stivoli, R. Stompor, H. Tran, M. Tristram, G. S. Tucker, Y. Vinokurov, A. Yadav, M. Zaldarriaga, and K. Zilic. EBEX: a balloon-borne CMB polarization experiment. In *Society of Photo-Optical Instrumentation Engineers (SPIE) Conference Series*, volume 7741 of *Society of Photo-Optical Instrumentation Engineers (SPIE) Conference Series*, July 2010.

[39] C. E. Tucker and P. A. R. Ade. Thermal filtering for large aperture cryogenic detector arrays. In *Society of Photo-Optical Instrumentation Engineers (SPIE) Conference Series*, volume 6275 of *Society of Photo-Optical Instrumentation Engineers (SPIE) Conference Series*, July 2006.

[40] S. Hanany, J. Hubmayr, B. R. Johnson, T. Matsumura, P. Oxley, and M. Thibodeau. Millimeter-wave achromatic half-wave plate. *Applied Optics*, 44:4666–4670, August 2005.

[41] J. Klein, A. Aboobaker, P. Ade, F. Aubin, C. Baccigalupi, C. Bao, J. Borrill, D. Chapman, J. Didier, M. Dobbs, B. Gold, W. Grainger, S. Hanany, J. Hubmayr, S. Hillbrand, J. Grain, A. Jaffe, B. Johnson, T. Jones, T. Kisner,

A. Korotkov, S. Leach, A. Lee, L. Levinson, M. Limon, K. MacDermid, T. Matsumura, A. Miller, M. Milligan, E. Pascale, D. Polsgrove, N. Ponthieu, K. Raach, B. Reichborn-Kjennerud, I. Sagiv, R. Stompor, H. Tran, M. Tristram, G. S. Tucker, A. Yadav, M. Zaldarriaga, and K. Zilic. A cryogenic half-wave plate polarimeter using a superconducting magnetic bearing. In *Society of Photo-Optical Instrumentation Engineers (SPIE) Conference Series*, volume 8150 of *Society of Photo-Optical Instrumentation Engineers (SPIE) Conference Series*, September 2011.

[42] C. Plummer, P. Roos, and L. Stagnaro. CAN Bus as a Spacecraft Onboard Bus. In *DASIA 2003*, volume 532 of *ESA Special Publication*, 2003.

[43] D. E. Polsgrove. *Calibration of the E and B EXperiment (EBEX), a balloon-borne cosmic microwave background polarimeter*. PhD thesis, University of Minnesota, 2009.

[44] B. Westbrook, A. Lee, X. Meng, A. Suzuki, K. Arnold, E. Shirokoff, E. George, F. Aubin, M. Dobbs, K. MacDermid, S. Hanany, K. Raach, A. Aboobaker, J. Hubmayr, T. Oshima, M. Kawamura, and K. Kohno. Design Evolution of the Spiderweb TES Bolometer for Cosmology Applications. *Journal of Low Temperature Physics*, 167:885–891, June 2012.

[45] M. E. Huber, P. A. Neil, R. G. Benson, D. A. Burns, A. M. Corey, C. S. Flynn, Y. Kitaygorodskaya, O. Massihzadeh, J. M. Martinis, and G. C. Hilton. DC SQUID serie array amplifiers with 120 MHz bandwidth (corrected). *IEEE Transactions on Applied Superconductivity*, 11:4048–4053, 2001.

[46] K. D. Irwin. An application of electrothermal feedback for high resolution cryogenic particle detection. *Applied Physics Letters*, 60(15):1998–2000, 1995.

[47] S.-F. Lee, J. M. Gildemeister, W. Holmes, A. T. Lee, and P. L. Richards. Voltage-Biased Superconducting Transition-Edge Bolometer with Strong Electrothermal Feedback Operated at 370 mK. *Applied Optics*, 37:3391–3397, June 1998.

[48] E. Shirokoff, B. A. Benson, L. E. Bleem, C. L. Chang, H.-M. Cho, A. T. Crites, M. A. Dobbs, W. L. Holzapfel, T. Lanting, A. T. Lee, M. Lueker, J. Mehl, T. Plagge, H. G. Spieler, and J. D. Vieira. The South Pole Telescope SZ-Receiver Detectors. *IEEE Transactions on Applied Superconductivity*, 19:517–519, June 2009.

[49] J. Mehl, P. A. R. Ade, K. Basu, D. Becker, A. Bender, F. Bertoldi, H. M. Cho, M. Dobbs, N. W. Halverson, W. L. Holzapfel, R. Gusten, J. Kennedy, R. Kneissl, E. Kreysa, T. M. Lanting, A. T. Lee, M. Lueker, K. M. Menten, D. Muders, M. Nord, F. Pacaud, T. Plagge, P. L. Richards, P. Schilke, D. Schwan, H. Spieler, A. Weiss, and M. White. TES Bolometer Array for the APEX-SZ Camera. *Journal of Low Temperature Physics*, 151:697–702, May 2008.

[50] K. D. Irwin and G. C. Hilton. *Cryogenic Particle Detection*, volume 99. Edited by C. Enss, 2005.

[51] J. C. Mather. Bolometer noise: nonequilibrium thoery. *Applied Optics*, 21:1125–1129, March 1982.

[52] J. M. Lamarre. Photon noise in photometric instruments at far-infrared and submillimeter wavelengths. *Applied Optics*, 25:870–876, March 1986.

[53] P. L. Richards. Bolometers for infrared and millimeter waves. *Journal of Applied Physics*, 76:1–24, July 1994.

[54] G. Smecher, F. Aubin, E. Bissonnette, M. Dobbs, P. Hyland, and K. MacDermid. Biasing and Demodulation Firmware for Kilopixel TES Bolometer Arrays. *ArXiv e-prints*, August 2010.

[55] M. Lueker, B. A. Benson, C. L. Chang, H.-M. Cho, M. Dobbs, W. L. Holzapfel, T. Lanting, A. T. Lee, J. Mehl, T. Plagge, E. Shirokoff, H. G. Spieler, and J. D. Vieira. Thermal Design and Characterization of Transition-Edge Sensor (TES) Bolometers for Frequency-Domain Multiplexing. *IEEE Transactions on Applied Superconductivity*, 19:496–500, June 2009.

[56] T. Montroy, P. A. R. Ade, A. Balbi, J. J. Bock, J. R. Bond, J. Borrill, A. Boscaleri, P. Cabella, C. R. Contaldi, B. P. Crill, P. de Bernardis, G. de Gasperis, A. de Oliveira-Costa, G. de Troia, G. di Stefano, K. Ganga, E. Hivon, V. V. Hristov, A. Iacoangeli, A. H. Jaffe, T. S. Kisner, W. C. Jones, A. E. Lange, S. Masi, P. D. Mauskopf, C. MacTavish, A. Melchiorri, F. Nati, P. Natoli, C. B. Netterfield, E. Pascale, F. Piacentini, D. Pogosyan, G. Polenta, S. Prunet, S. Ricciardi, G. Romeo, J. E. Ruhl, E. Torbet, M. Tegmark, and N. Vittorio. Measuring CMB polarization with Boomerang. *New Astronomy Review*, 47:1057–1065, December 2003.

[57] J. H. P. Wu, J. Zuntz, M. E. Abroe, P. A. R. Ade, J. Bock, J. Borrill, J. Collins, S. Hanany, A. H. Jaffe, B. R. Johnson, T. Jones, A. T. Lee, T. Matsumura,

B. Rabii, T. Renbarger, P. L. Richards, G. F. Smoot, R. Stompor, H. T. Tran, and C. D. Winant. MAXIPOL: Data Analysis and Results. *Astrophysical Journal*, 665:55–66, August 2007.

[58] C. Pryke, P. Ade, J. Bock, M. Bowden, M. L. Brown, G. Cahill, P. G. Castro, S. Church, T. Culverhouse, R. Friedman, K. Ganga, W. K. Gear, S. Gupta, J. Hinderks, J. Kovac, A. E. Lange, E. Leitch, S. J. Melhuish, Y. Memari, J. A. Murphy, A. Orlando, R. Schwarz, C. O'Sullivan, L. Piccirillo, N. Rajguru, B. Rusholme, A. N. Taylor, K. L. Thompson, A. H. Turner, E. Y. S. Wu, and M. Zemcov. Second and Third Season QUaD Cosmic Microwave Background Temperature and Polarization Power Spectra. *Astrophysical Journal*, 692:1247–1270, February 2009.

[59] K. D. Irwin. SQUID multiplexers for transition-edge sensors. *Physica C Superconductivity*, 368:203–210, March 2002.

[60] M. D. Audley, W. D. Duncan, W. S. Holland, A. Walton, W. Parkes, C. Dunare, A. Gundlach, T. Stevenson, K. D. Irwin, G. C. Hilton, E. Schulte, P. A. R. Ade, and C. Tucker. Fabrication of the SCUBA-2 detector arrays. *Nuclear Instruments and Methods in Physics Research A*, 520:483–486, March 2004.

[61] D. S. Swetz, P. A. R. Ade, M. Amiri, J. W. Appel, E. S. Battistelli, B. Burger, J. Chervenak, M. J. Devlin, S. R. Dicker, W. B. Doriese, R. Dünner, T. Essinger-Hileman, R. P. Fisher, J. W. Fowler, M. Halpern, M. Hasselfield, G. C. Hilton, A. D. Hincks, K. D. Irwin, N. Jarosik, M. Kaul, J. Klein, J. M. Lau, M. Limon, T. A. Marriage, D. Marsden, K. Martocci, P. Mauskopf, H. Moseley, C. B. Netterfield, M. D. Niemack, M. R. Nolta, L. A. Page, L. Parker, S. T. Staggs, O. Stryzak, E. R. Switzer, R. Thornton, C. Tucker, E. Wollack, and Y. Zhao. Overview of the Atacama Cosmology Telescope: Receiver, Instrumentation, and Telescope Systems. *Astrophysical Journal, Supplement*, 194:41, June 2011.

[62] B. P. Crill, P. A. R. Ade, E. S. Battistelli, S. Benton, R. Bihary, J. J. Bock, J. R. Bond, J. Brevik, S. Bryan, C. R. Contaldi, O. Doré, M. Farhang, L. Fissel, S. R. Golwala, M. Halpern, G. Hilton, W. Holmes, V. V. Hristov, K. Irwin, W. C. Jones, C. L. Kuo, A. E. Lange, C. Lawrie, C. J. MacTavish, T. G. Martin, P. Mason, T. E. Montroy, C. B. Netterfield, E. Pascale, D. Riley, J. E. Ruhl, M. C. Runyan, A. Trangsrud, C. Tucker, A. Turner, M. Viero, and D. Wiebe. SPIDER: a balloon-borne large-scale CMB polarimeter. In *Society of Photo-Optical Instrumentation Engineers (SPIE) Conference Series*, volume 7010 of

Society of Photo-Optical Instrumentation Engineers (SPIE) Conference Series, August 2008.

[63] R. W. Ogburn, IV, P. A. R. Ade, R. W. Aikin, M. Amiri, S. J. Benton, C. A. Bischoff, J. J. Bock, J. A. Bonetti, J. A. Brevik, E. Bullock, B. Burger, G. Davis, C. D. Dowell, L. Duband, J. P. Filippini, S. Fliescher, S. R. Golwala, M. Gordon, M. Halpern, M. Hasselfield, G. Hilton, V. V. Hristov, H. Hui, K. Irwin, J. P. Kaufman, B. G. Keating, S. A. Kernasovskiy, J. M. Kovac, C. L. Kuo, E. M. Leitch, M. Lueker, T. Montroy, C. B. Netterfield, H. T. Nguyen, R. O'Brient, A. Orlando, C. L. Pryke, C. Reintsema, S. Richter, J. E. Ruhl, M. C. Runyan, R. Schwarz, C. D. Sheehy, Z. K. Staniszewski, R. V. Sudiwala, G. P. Teply, K. Thompson, J. E. Tolan, A. D. Turner, A. G. Vieregg, D. V. Wiebe, P. Wilson, and C. L. Wong. BICEP2 and Keck Array operational overview and status of observations. *ArXiv e-prints*, August 2012.

[64] M. Dobbs, M. Halpern, K. D. Irwin, A. T. Lee, J. A. B. Mates, and B. A. Mazin. Multiplexed readout of CMB polarimeters. *Journal of Physics Conference Series*, 155(1):012004, March 2009.

[65] K. G. Beauchamp. *Walsh Functions and Their Applications*. London : Academic Press, 1975.

[66] K. D. Irwin, M. D. Niemack, J. Beyer, H. M. Cho, W. B. Doriese, G. C. Hilton, C. D. Reintsema, D. R. Schmidt, J. N. Ullom, and L. R. Vale. Code-division multiplexing of superconducting transition-edge sensor arrays. *Superconductor Science Technology*, 23(3):034004, March 2010.

[67] M. D. Niemack, J. Beyer, H. M. Cho, W. B. Doriese, G. C. Hilton, K. D. Irwin, C. D. Reintsema, D. R. Schmidt, J. N. Ullom, and L. R. Vale. Code-division SQUID multiplexing. *Applied Physics Letters*, 96(16):163509, April 2010.

[68] T. M. Lanting, H. Cho, J. Clarke, M. Dobbs, A. Lee, P. L. Richards, A. D. Smithm, and H. G. Spieler. A frequency-domain squid multiplexer for arrays of transition-edge superconducting sensors. *IEEE Transactions on Applied Superconductivity*, 13(2):626, 2003.

[69] J. Ruhl, P. A. R. Ade, J. E. Carlstrom, H.-M. Cho, T. Crawford, M. Dobbs, C. H. Greer, N. w. Halverson, W. L. Holzapfel, T. M. Lanting, A. T. Lee, E. M. Leitch, J. Leong, W. Lu, M. Lueker, J. Mehl, S. S. Meyer, J. J. Mohr, S. Padin, T. Plagge, C. Pryke, M. C. Runyan, D. Schwan, M. K. Sharp, H. Spieler,

Z. Staniszewski, and A. A. Stark. The South Pole Telescope. In C. M. Bradford, P. A. R. Ade, J. E. Aguirre, J. J. Bock, M. Dragovan, L. Duband, L. Earle, J. Glenn, H. Matsuhara, B. J. Naylor, H. T. Nguyen, M. Yun, and J. Zmuidzinas, editors, *Society of Photo-Optical Instrumentation Engineers (SPIE) Conference Series*, volume 5498 of *Society of Photo-Optical Instrumentation Engineers (SPIE) Conference Series*, pages 11–29, October 2004.

[70] B. Keating, S. Moyerman, D. Boettger, J. Edwards, G. Fuller, F. Matsuda, N. Miller, H. Paar, G. Rebeiz, I. Schanning, M. Shimon, N. Stebor, K. Arnold, D. Flanigan, W. Holzapfel, J. Howard, Z. Kermish, A. Lee, M. Lungu, M. Myers, H. Nishino, R. O'Brient, E. Quealy, C. Reichardt, P. Richards, C. Shimmin, B. Steinbach, A. Suzuki, O. Zahn, J. Borrill, C. Cantalupo, E. Kisner, E. Linder, M. Sholl, H. Spieler, A. Anthony, N. Halverson, J. Errard, G. Fabbian, M. Le Jeune, R. Stompor, A. Jaffe, D. O'Dea, Y. Chinone, M. Hasegawa, M. Hazumi, T. Matsumura, H. Morii, A. Shimizu, T. Tomaru, P. Hyland, M. Dobbs, P. Ade, W. Grainger, and C. Tucker. Ultra High Energy Cosmology with POLARBEAR. *ArXiv e-prints*, October 2011.

[71] L. Bleem, P. Ade, K. Aird, J. Austermann, J. Beall, D. Becker, B. Benson, J. Britton, J. Carlstrom, C. Chang, H. Cho, T. de Haan, T. Crawford, A. Crites, A. Datesman, M. Dobbs, W. Everett, A. Ewall-Wice, E. George, N. Halverson, N. Harrington, J. Henning, G. Hilton, W. Holzapfel, S. Hoover, J. Hubmayr, K. Irwin, R. Keisler, J. Kennedy, A. Lee, E. Leitch, D. Li, M. Lueker, D. Marrone, J. McMahon, J. Mehl, S. Meyer, J. Montgomery, T. Montroy, T. Natoli, J. Nibarger, M. Niemack, V. Novosad, S. Padin, C. Pryke, C. Reichardt, J. Ruhl, B. Saliwanchik, J. Sayre, K. Schafer, E. Shirokoff, K. Story, K. Vanderlinde, J. Vieira, G. Wang, R. Williamson, V. Yefremenko, K. Yoon, and E. Young. An overview of the sptpol experiment. *Journal of Low Temperature Physics*, 167:859–864, 2012. 10.1007/s10909-012-0505-y.

[72] K. D. Irwin, G. C. Hilton, D. A. Wollman, and J. M. Martinis. Thermal-response time of superconducting transition-edge microcalorimeters. *Journal of Applied Physics*, 83:3978–3985, April 1998.

[73] M. A. Dobbs, M. Lueker, K. A. Aird, A. N. Bender, B. A. Benson, L. E. Bleem, J. E. Carlstrom, C. L. Chang, H.-M. Cho, J. Clarke, T. M. Crawford, A. T. Crites, D. I. Flanigan, T. de Haan, E. M. George, N. W. Halverson, W. L. Holzapfel, J. D. Hrubes, B. R. Johnson, J. Joseph, R. Keisler, J. Kennedy, Z. Kermish, T. M. Lanting, A. T. Lee, E. M. Leitch, D. Luong-Van, J. J.

McMahon, J. Mehl, S. S. Meyer, T. E. Montroy, S. Padin, T. Plagge, C. Pryke, P. L. Richards, J. E. Ruhl, K. K. Schaffer, D. Schwan, E. Shirokoff, H. G. Spieler, Z. Staniszewski, A. A. Stark, K. Vanderlinde, J. D. Vieira, C. Vu, B. Westbrook, and R. Williamson. Frequency Multiplexed SQUID Readout of Large Bolometer Arrays for Cosmic Microwave Background Measurements. *ArXiv e-prints*, December 2011.

[74] T. M. Lanting. *Multiplexed readout of superconducting bolometers for cosmological observations*. PhD thesis, University of California, Berkeley, 2006.

[75] M. Dobbs, E. Bissonnette, and H. Spieler. Digital Frequency Domain Multiplexer for Millimeter-Wavelength Telescopes. *IEEE Transactions on Nuclear Science*, 55:21–26, 2008.

[76] K. MacDermid, P. Hyland, F. Aubin, E. Bissonnette, M. Dobbs, J. Hubmayr, G. Smecher, and S. Wairrach. Tuning of Kilopixel Transition Edge Sensor Bolometer Arrays with a Digital Frequency Multiplexed Readout System. In B. Young, B. Cabrera, and A. Miller, editors, *American Institute of Physics Conference Series*, volume 1185 of *American Institute of Physics Conference Series*, pages 253–256, December 2009.

[77] M. B. Milligan. *The E and B EXperiment: Implementation and Analysis of the 2009 Engineering Flight*. PhD thesis, University of Minnesota, 2011.

[78] F. Aubin, A. M. Aboobaker, P. Ade, C. Baccigalupi, C. Bao, J. Borrill, C. Cantalupo, D. Chapman, J. Didier, M. Dobbs, W. Grainger, S. Hanany, J. Hubmayr, P. Hyland, S. Hillbrand, A. Jaffe, B. Johnson, T. Jones, T. Kisner, J. Klein, A. Korotkov, S. Leach, A. Lee, M. Limon, K. MacDermid, T. Matsumura, X. Meng, A. Miller, M. Milligan, D. Polsgrove, N. Ponthieu, K. Raach, B. Reichborn-Kjennerud, I. Sagiv, G. Smecher, H. Tran, G. S. Tucker, Y. Vinokurov, A. Yadav, M. Zaldarriaga, and K. Zilic. First implementation of TES bolometer arrays with SQUID-based multiplexed readout on a balloon-borne platform. In *Society of Photo-Optical Instrumentation Engineers (SPIE) Conference Series*, volume 7741 of *Society of Photo-Optical Instrumentation Engineers (SPIE) Conference Series*, July 2010.

[79] J.R. Pardo, J. Cernicharo, and E. Serabyn. Atmospheric transmission at microwaves (atm): an improved model for millimeter/submillimeter applications. *Antennas and Propagation, IEEE Transactions on*, 49(12):1683 –1694, dec 2001.

[80] J. W. Lamb. Miscellaneous data on materials for millimetre and submillimeter optics. *International Journal of Infrared and Millimeter Waves*, 17(19):1997–2034, 1996.

[81] J. B. Peterson and P. L. Richards. A cryogenic blackbody for millimeter wavelengths. *International Journal of Infrared and Millimeter Wave*, 5(12):1507–1515, 1984.

[82] J. Clarke and A. I. Braginski. *The SQUID Handbook: Fundamentals and Technology of SQUIDs and SQUID Systems, Volume I*. J. Clarke and A. I. Braginski, Wiley-VCH Verlag GmbH & Co. KGaA, 2004.